

# POLITECNICO DI TORINO

Department of  
Control and Computer Engineering (DAUIN)

**Master of Science in Mechatronic Engineering**

Master Degree Thesis  
Performance Testing and Components  
Characterization for Martian Drone Prototype



**Supervisor:**  
Prof. Marcello Chiaberge

**Candidate:**  
Margherita Marchi

July 2019

# Contents

<b>Abstract</b>	<b>vii</b>
<b>1 Re-inventing Flying on Mars</b>	<b>1</b>
1.1 Next Stop: Mars . . . . .	1
1.2 Reinventing Flight in a New Atmosphere . . . . .	3
1.2.1 Mars/Earth atmosphere comparison . . . . .	6
1.2.2 Effect of Mach number . . . . .	8
1.2.3 Effect of low Reynolds number . . . . .	9
1.3 State of the art . . . . .	10
1.3.1 The American prototype . . . . .	10
1.3.2 The French experience . . . . .	16
1.3.3 University of Tokyo project . . . . .	17
1.3.4 Thales Alenia Mars Drone Project . . . . .	19
<b>2 Performance Accuracy Investigation</b>	<b>26</b>
2.1 Vacuum Testing . . . . .	26
2.2 Test Bench Components . . . . .	30
2.2.1 Load cell . . . . .	30
2.2.2 Motor . . . . .	32
2.2.3 ESC Driver . . . . .	36
2.2.4 Accelerometers . . . . .	37
2.2.5 Joint Coupling . . . . .	37
2.2.6 Torque Meter . . . . .	38
2.2.7 Propeller & Hub . . . . .	41
2.3 Preventive Vacuum Testing . . . . .	42
2.3.1 Vibration Analysis . . . . .	43
2.3.2 Fixed Setup Testing . . . . .	47
2.4 Motor Characterization . . . . .	49
2.4.1 Controller Software . . . . .	49
2.4.2 Motor tests . . . . .	51
2.5 Updating Mechanical Connections . . . . .	57
2.6 Air Tests . . . . .	60
2.6.1 Air Propeller Selection . . . . .	60
2.6.2 Acquisition & Supply System . . . . .	65
2.6.3 Firsts Results . . . . .	71
2.6.4 Vibration Tests . . . . .	75
2.6.5 Simulation of Vacuum Chamber Electrical Connections . . . . .	80
2.7 New Vacuum Chamber Torque Test Campaign . . . . .	84

---

2.7.1	Standard air test with 15"x5" L propeller . . . . .	85
2.7.2	Martian atmosphere test with 15"x5" L propeller . . . . .	88
2.7.3	Martian atmosphere test with Thales Alenia Space propeller . . . . .	93
2.8	Investigation on new Thrust Test-bench . . . . .	97
<b>Conclusion</b>		<b>103</b>
<b>Nomenclature</b>		<b>105</b>
<b>Acknowledgement</b>		<b>107</b>
<b>Bibliography</b>		<b>108</b>

# List of Figures

1.1	Distance walked by manned and unmanned rovers in space exploration history. ©NASA . . . . .	2
1.2	Mars Scout Helicopter in May 2019. ©NASA/JPL-Caltech . . . . .	4
1.3	Speed of sound comparison Earth/Mars. ©Aerospaceweb . . . . .	6
1.4	Density comparison Mars/Earth Atmosphere. ©NASA . . . . .	8
1.5	Laminar separation bubble at low Re. ©NASA . . . . .	10
1.6	MHS final design [1]. ©NASA . . . . .	15
1.7	Eiffel 428 blade with 26 cm chord. ©ONERA . . . . .	16
1.8	Perlan II model.©Airbus . . . . .	17
1.9	Carbon fiber replica of University of Maryland propeller used for Thales Alenia Space tests . . . . .	19
1.10	Swing test bench in TAS-I PHASE vacuum chamber . . . . .	20
1.11	Detailed view swing test bench . . . . .	21
1.12	Thrust results comparison with Maryland experimental data . . . . .	23
1.13	Torque results comparison with Maryland experimental data . . . . .	24
1.14	Acquired torque error distribution . . . . .	25
2.1	Internal PHASE structure scheme . . . . .	29
2.2	Working principle rotating vane pump. ©Pfeiffer . . . . .	29
2.3	S beam miniature load cell. ©FUTEK . . . . .	30
2.4	Wheatstone bridge of a load cell . . . . .	31
2.5	BLDC emf and current profile per phase . . . . .	32
2.6	Internal Structure of 2264W 4 poles BLDC. ©Faulhaber . . . . .	35
2.7	Ideal Torque/Speed relation of BLDC motor . . . . .	35
2.8	Faulhaber ESC SC5008 . . . . .	36
2.9	Jaw coupling elements . . . . .	38
2.10	T21WN torque meter. ©HBM . . . . .	39
2.11	Torque meter contactless transmission principle [2] . . . . .	40
2.12	Schematic of structural loads on torque meter. ©HBM . . . . .	41
2.13	Propeller pitch angle . . . . .	42
2.14	Axial Vibrations cascade plot at varying speed $\omega$ . . . . .	44
2.15	Flexural Vibrations cascade plot at varying speed $\omega$ . . . . .	45
2.16	Thrust cascade plot at varying speed $\omega$ . . . . .	46
2.17	Torque cascade plot at varying speed $\omega$ . . . . .	46
2.18	Comparison between torque data trends in old setup (swing) and the new setup (fixed) . . . . .	48
2.19	3D model of the fixed setup used for vacuum testing . . . . .	48
2.20	USB connector . . . . .	49

2.21	Block diagram of the controller . . . . .	50
2.22	Input voltage functions for the ESC . . . . .	51
2.23	Data acquired at $U_{nsoll}$ changing . . . . .	53
2.24	Data acquired when $U_{mot}$ changing and $U_{nsoll}$ is saturated . . . . .	54
2.25	Torque-current relationship in no load conditions for Faulhaber 2264W 024 motor . . . . .	55
2.26	Torque-current relationship for Faulhaber 2264W 024 motor coupled with HBM T21WN torque meter . . . . .	57
2.27	R+W MK1 miniature bellow coupling . . . . .	58
2.28	Aluminium cage on torque meter side . . . . .	59
2.29	Aluminium cage lid on motor side . . . . .	59
2.30	Torque-speed comparison for FAULHABER 2264W 024 motor and different propellers . . . . .	61
2.31	T-motor 15"x5" L propeller and fixing cover . . . . .	62
2.32	T-motor fixing cover scheme . . . . .	62
2.33	T-motor 15"x5" L connector for HBM T21WN torque meter . . . . .	63
2.34	Test bench used for torque testing in standard air . . . . .	64
2.36	Electronic Control Unit Schematic . . . . .	67
2.37	Ramp cycle for data acquisition . . . . .	68
2.38	Comparison between filtered and unfiltered torque signal acquired at 10 kHz . . . . .	69
2.39	Passive low pass filter with cutting frequency $f_c=15$ kHz . . . . .	69
2.40	Torque-speed characteristic of 15"x5" L acquired compared with state of the art . . . . .	71
2.41	Variation of motor torque with different control methods . . . . .	72
2.42	Errorbar plot comparing acquired filtered torque and unfiltered. . . . .	74
2.43	Torque polynomial regression . . . . .	74
2.44	Unfiltered Torque Vibration . . . . .	76
2.45	Filtered Torque Vibrations . . . . .	76
2.46	Colour map for unfiltered torque vibrations by harmonics . . . . .	77
2.47	Filtered torque waterfall plot . . . . .	78
2.48	Colour map for speed vibrations . . . . .	78
2.49	Accelerometers positioning for hammering test . . . . .	79
2.50	Hammering test results . . . . .	79
2.51	PCB inputs and outputs for propeller performance testing . . . . .	81
2.52	PCB electronic scheme for propeller performance testing . . . . .	82
2.53	Errorbar plot for acquired torque with long cables set . . . . .	83
2.54	Torque speed characteristic for long cable set . . . . .	83
2.55	Comparison for errorbar data within open air propeller test and vacuum chamber filled with standard air test. . . . .	86
2.56	Torque comparison between acquired data and computed data for 15"x5"L testing in vacuum chamber filled with standard air . . . . .	86
2.57	Comparison torque-speed data acquired in open air test and in vacuum chamber filled with standard air . . . . .	87
2.58	Unfiltered torque waterfall for propeller 15"x5" L in standard air in the chamber . . . . .	87
2.59	Filtered torque waterfall for propeller 15"x5" L in standard air in chamber . . . . .	88
2.60	Torque-speed data acquired with 15"x5" L propeller in Martian-like atmosphere. . . . .	89

2.61	Torque comparison between acquired data and computed for 15"x5" L in low density environment . . . . .	90
2.62	Comparison speed as read by the torque meter encoder and as computed from the motor characteristic for 15"x5" L propeller in low density atmosphere . . . . .	90
2.63	Errorbar torque distribution for 15"X5" L propeller in Martian-like atmosphere . . . . .	91
2.64	Filtered torque waterfall for propeller 15"X5" L in Martian like density . . . . .	91
2.65	Unfiltered torque waterfall for propeller 15"x5" L in Martian-like density . . . . .	92
2.66	Aliasing causes mirroring the frequency that happens to be higher than $f_{max}=f_s/2$ , where $f_s$ is the sampling frequency. ©SIEMENS . . . . .	92
2.67	Torque distribution for previous Martian propeller tests in TAS-I PHASE chamber and for data acquired with the new system . . . . .	94
2.68	New architecture torque result for Martian propeller compared to University of Maryland's one. . . . .	94
2.69	Comparison between torque data found for fixed setup in PHASE vacuum chamber before and after the architecture changes . . . . .	95
2.70	Filtered torque waterfall for Martian blade in vacuum . . . . .	96
2.71	Unfiltered torque waterfall for Martian blade in vacuum . . . . .	96
2.72	Computed and acquired torque comparison for Martian blade in Martian-like conditions . . . . .	97
2.73	New thrust setup design . . . . .	98
2.74	Moment arm for air test analysis . . . . .	99
2.75	Maximum thrust defined as a moment in function of the beam arm length . . . . .	100
2.76	Thrust moment as a function of the arm length with respect to the speed in vacuum condition . . . . .	101
2.77	Thrust test bench with propeller parallel to the vacuum chamber axis. . . . .	102

# List of Tables

1.1	Solar System celestial bodies suitable for flight . . . . .	3
1.2	U.S. Standard Atmosphere model for lower layers . . . . .	6
1.3	Blade evolution NASA . . . . .	12
1.4	MHS final characteristics . . . . .	15
1.5	Hypothetical 60 g drone mass budget. . . . .	18
1.6	Summary of data acquisition for previous tests . . . . .	22
2.1	Vacuum Quality Ranges . . . . .	27
2.2	TAS-I PHASE technical data . . . . .	28
2.3	Pinout for SC5008S driver . . . . .	37
2.4	Data acquired from varying tension tests . . . . .	52
2.5	Data acquired from $U_{nsoll}$ saturated test . . . . .	53
2.6	Data acquired from current tests . . . . .	55
2.7	Data acquired with $k_T$ testing . . . . .	56
2.8	Comparison between coupling used and advised . . . . .	58
2.9	USB 6211 pin out table . . . . .	70
2.10	$c_Q$ value distribution in different test runs . . . . .	73

# Abstract

The aim of this thesis is to provide a suitable test stand that could be used to evaluate performances of a Martian drone prototype. The main issues were sparked by the necessity for test bench components to work in low density atmosphere, near to the Martian one, and the scarce amount of previous research on extra-terrestrial atmosphere flight. The first part of the thesis will focus on a discussion of new research works and papers that were published in this field, while the second part will be entirely dedicated to the process that led to the final testing architecture. The final test bench was developed from components of a previously existing low density test bench, that provided inaccurate torque measurements. The thesis will discuss the characterization of single components used to measure drone performances and will investigate problems that could have contributed to erroneous previous measurements.

L'obiettivo di questa tesi è di progettare un banco di prova adatto a testare le performance di un prototipo per drone marziano. Le più grandi difficoltà sono scaturite dalla necessità che i componenti, facenti parte del banco, potessero lavorare in atmosfera a bassa densità, vicine alle condizioni marziane, e dalla scarsa presenza di ricerche precedenti sul volo in atmosfera extra-terrestre. La prima parte della tesi si concentrerà sulla discussione di articoli e ricerche pubblicate finora sulla progettazione di un drone marziano, mentre la seconda parte sarà interamente dedicata al processo che ha permesso di ottenere l'architettura di test finale. Il banco di prova è stato sviluppato partendo da componenti usati per un precedente sistema di test in atmosfera a bassa densità, il quale si è dimostrato dare misure di coppia inaccurate. In questa tesi si discuterà la caratterizzazione dei singoli componenti usati nella misura di coppia e verranno investigati i problemi che possono aver portato alle precedenti misure erranee.

# Chapter 1

## Re-inventing Flying on Mars

### 1.1 Next Stop: Mars

Planetary observation is one of the most used tools to get to know the universe that surrounds our planet Earth. The technology used nowadays can be divided in two main types: orbiters and surface rovers. Each type has its perks: the first one enables to analyse the atmosphere and the outside appearance of a celestial body, while the second type can scan the surface and examine physical and chemical properties of the soil. However, it can be spotted that the massive amount of data, that been have received from these robots over the years, does not take into account a large area of the planet explored. This due to their low speed compared to the one of normal terrestrial vehicles: for example, the highest speed NASA's Opportunity rover could reach was approximately 0.18 km/h (Fig.1.1). Speed constraints on rovers are due to two main factors: the fragility of rovers' onboard systems and their high dependency on proximity sensors and SLAM (Simultaneous Localization and Mapping) algorithm to explore the environment around them. Moreover, it has to be stated that rovers cannot be controlled in real-time, since it takes up to 21 minutes to communicate with Earth from Mars, meaning they have to be semi-completely auto-sufficient.

The continuous interest in finding new ways to perform a better exploration led, at the beginning of the 21<sup>st</sup> century, to the design of the first prototypes of extraterrestrial flying drones [3]. It was mostly the necessity of taking a closer look at our Solar System neighbours that led to a more in-depth research in extraterrestrial aircraft field. Up to now, this type of studies has been focusing on the following celestial bodies: Mars, Venus and Titan, Saturn's largest moon. Drone architecture could be best suited for exploration since it would allow to speed up operations and overcome the fragility of a rover. For example, NASA's Opportunity rover took 340 sols<sup>1</sup> to find a safe path and descend into Mars' Victoria crater [4]: this operation would have been extremely less time consuming with a drone able over to fly over the crater and directly land at its interior. Moreover, it has been thought that a rover and a drone could work in synergy to accelerate the path of the rover. As a consequence of rover limits, current planet exploration is mainly limited to plains because caves and mountains are not easily accessible by unmanned vehicles but these spots could represent the most interesting points for soil analysis and search for life.

As it can be seen from Table 1.1, the celestial bodies, taken into account for a drone

---

<sup>1</sup>1 sol=1 Martian day=24h 39min.

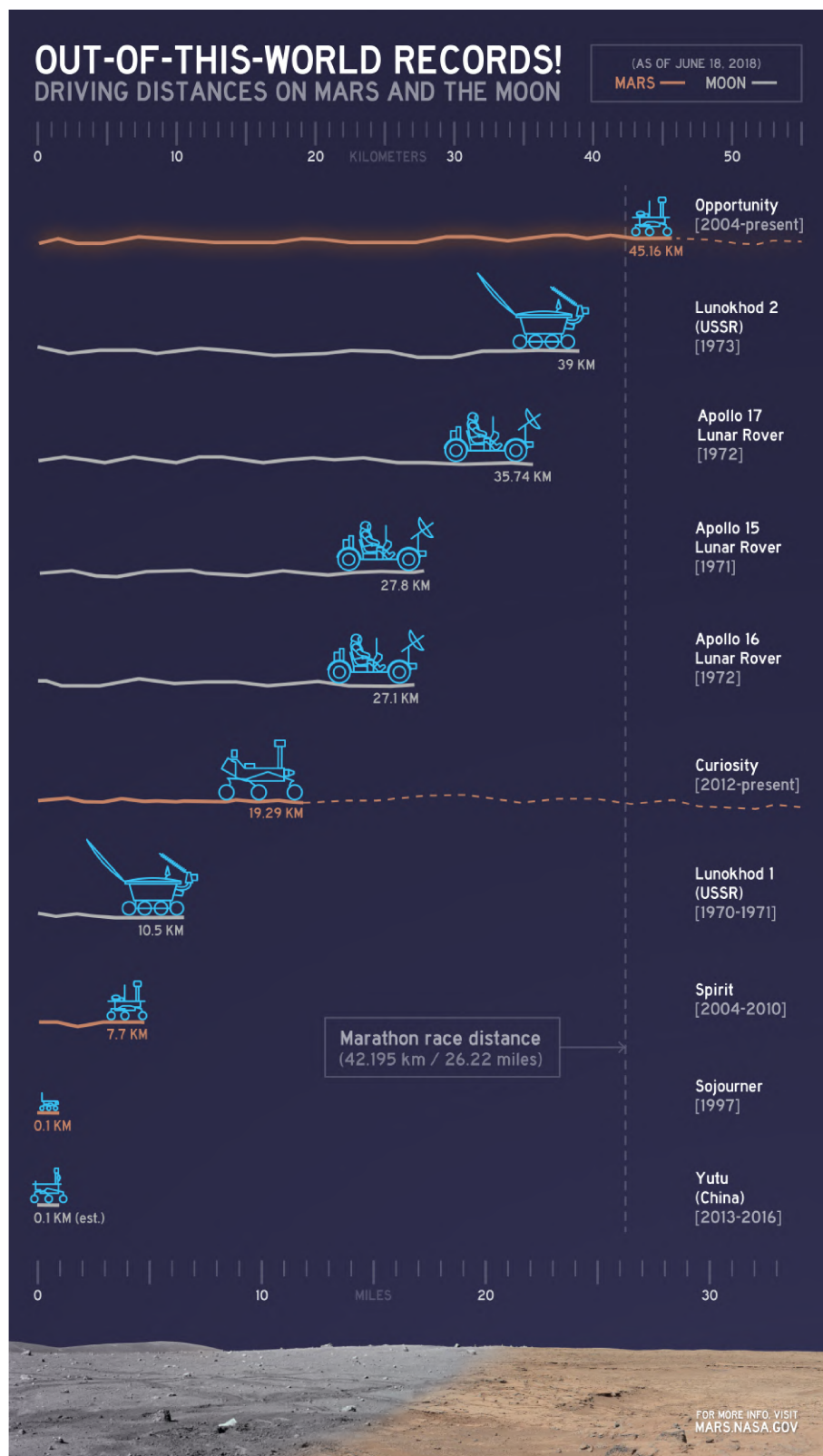


Figure 1.1: Distance walked by manned and unmanned rovers in space exploration history. ©NASA

	Earth	Mars	Venus	Titan
Mean Radius [km]	6371	3390	6052	2575
Gravity [ $\text{m/s}^2$ ]	9.82	3.71	8.87	1.354
Mean Surface Atm. Temperature [K]	288.2	214	735.3	94
Mean Surface Atm. Pressure [Pa]	101300	636	$9.21 \times 10^6$	149526
Mean Surface Atm. Density [ $\text{kg/m}^3$ ]	1.23	$1.55 \cdot 10^{-2}$	64.79	5.55
Atmospheric Composition	$N_2$ 78% $O_2$ 21%	$CO_2$ 95% $N_2$ 2.7%	$CO_2$ 96% $N_2$ 3.5%	$N_2$ 65-98% $Ar$ < 25%

Table 1.1: Solar System celestial bodies suitable for flight

exploration differ greatly one from the other, regarding dimensions and atmosphere characteristics. It has to be underlined that the comparison shown in Table 1.1 is only between the "sea level" atmospheres. Within the different planets, the one chosen to host the extra-terrestrial flight project is Mars. The main difference that stands out, between Mars and Earth, is the low density of Martian atmosphere with respect to the one of Earth: this will represent the main challenge in performing a flight on the Red Planet. The main reasons that led to pick this body, to investigate the possibility of flying, over the others, are the following:

1. from the beginning of the year 2000, space exploration has largely seen in the Red Planet a future for the mankind, finding water molecules under the planet surface and in its rocks, and a flying drone could help this research in hardly accessible environments;
2. most of current scheduled space missions are directed towards Mars, so there are multiple occasions to send a drone as a payload of a pre-existent mission;
3. the great number of previous missions that were conducted, more or less successfully, on this planet, has left an enormous scientific heritage that could support the development of a project for flying on Mars.

NASA, which was the first to start investigating the possibility of an extraterrestrial drone, has succeeded in designing a functional prototype: the Mars Helicopter Scout (MHS). This small helicopter, shown in Figure 1.2, will launch with the mission *Mars 2020*.

## 1.2 Reinventing Flight in a New Atmosphere

Flying has become a normal operation for the mankind: helicopter, airplanes and drones take off every minute and they do not inspire awe anymore. Flying in an extraterrestrial atmosphere represents, instead, a colossal deed for modern engineering.

It is important to acknowledge that the flying systems used today have been optimized for the terrestrial atmosphere, which is described in Table 1.1, but they would not work as successfully in other environmental conditions. One of the main parameters that has to be taken into account is the density of the atmosphere: for example, flying on Titan would not be that difficult as on Mars, since the atmosphere is so dense that even a man flapping his arms could take off.



Figure 1.2: Mars Scout Helicopter in May 2019. ©NASA/JPL-Caltech

As previously shown the atmosphere on Mars is very rarefied, attesting its density value around  $1/100^{\text{th}}$  of the terrestrial one: this would cause issues for the lift force of a general air vehicle trying to fly in a Martian environment. Describing how different atmospheres could affect a flying object is not trivial, therefore two main dimensionless coefficients were developed to describe the aerodynamic behaviour of a body in a general fluid: Reynolds number ( $Re$ ) and Mach number ( $Ma$ ). The two are defined as:

$$Ma = \frac{\text{speed of the object}}{\text{speed of sound in the medium}} \quad (1.1)$$

$$Re = \frac{\rho u L}{\mu} = \frac{u L}{\nu} \quad (1.2)$$

where:

- $\rho$  [kg/m<sup>3</sup>] is the the density of the fluid;
- $u$  [m/s] is the speed of the fluid with respect to the object;
- $\mu$  [Pa·s] is the dynamic viscosity;
- $\nu$  [m<sup>2</sup>/s] represents the kinematic viscosity of the fluid;
- $L$  [m] is the characteristic dimension.

Taking into account the densities in Earth and Mars atmospheres, it may be considered that the Reynolds number for the same object with the same velocity will drastically decrease in Martian conditions. On the other hand, to evaluate the Mach number, it has to be taken into account the speed of sound on Mars. The speed of sound formula is the following:

$$a = \sqrt{\gamma R T} \quad (1.3)$$

where:

- $a$  [m/s] represents the speed of sound in a known medium;
- $\gamma$  is the heat constant defined for the medium;

- $R$  [J/(kgK)] is the specific gas constant;
- $T$  [K] is the temperature of the medium.

Analysing this formula, it can be noted that the speed of sound depends directly on the temperature of the medium in which it is being calculated. Considering Earth atmosphere condition, it can be stated that the speed of sound changes also with respect to the altitude, because as seen from the U.S. Standard Model for the terrestrial atmosphere [5], built in 1976, the air temperature fluctuates greatly between the different atmosphere layers, as depicted in Figure 1.3). A similar standard model<sup>2</sup> (Mars Atmospheric Model) has been built in 1996 by NASA for planet Mars, thanks to the different data recovered from diverse missions, and most importantly thanks to the Mars Global Surveyor contribute. This model has not been optimized yet, but hopefully will be in the near future. Taking into consideration this model of Martian atmosphere at its presents state, the parameters that define the speed of sound in this medium can be defined as it follows:

$$\gamma_{Mars} = 1.29$$

$$R_{Mars} = 191.8 \text{ J/(kgK)}$$

$$T_{(\leq 7000m)} = -32.0 - 0.000998 \cdot h$$

$$T_{(> 7000m)} = -23.4 - 0.002220 \cdot h$$

Considering that any present hypothesis on flying on Mars is restricted to a maximum 10 m height, it can be declared that the speed of sound in the range from the surface to 10 m in altitude can be approximated to the one of 0 m altitude, sea level. Therefore, the speed of sound at sea level on Mars is:

$$a_{Mars} = 244 \text{ m/s}$$

This value is substantially smaller than the speed of sound at the same altitude on Earth (343,8 m/s), at mean temperature 20° C.

It can be seen from Fig.1.3, that the speed of sound on Mars is nearly perfectly inversely proportional to the altitude, while the same cannot be said for Earth.

It is important to underline a less prominent discrepancy between Mars' and Earth's atmosphere: the atmosphere of the Red Planet is thinner than the one found on Earth, speaking of how much it propagates from the surface of the planet. This characteristic makes the Martian "air" less stable and more sensitive to Solar and Universal radiations, leading to a seasonal reduction of the atmosphere in Martian winter, when 20% of the CO<sub>2</sub>, present in the atmosphere, sublimates into ice at the poles.

Taking into account the nature of Martian atmosphere, stressing the low density and smaller speed of sound, the problem of flying on Mars can be directly translated in having a rotor that could be able to work with low Reynolds number and high Mach. This kind of flight has already been studied while analysing the flying of insects and trying to recreate it in tiny drones, as it is discussed in [6]. It is important to underline how most of the previous works done on Low Reynolds focused on small air wings, so the changing quantity, in formula 1.2, was  $L$ , the length of the characteristic dimension, while in the case that will be discussed in this dissertation the most important varying factor is the air density.

<sup>2</sup>[www.grc.nasa.gov/www/k-12/airplane/atmosmrm.html](http://www.grc.nasa.gov/www/k-12/airplane/atmosmrm.html)

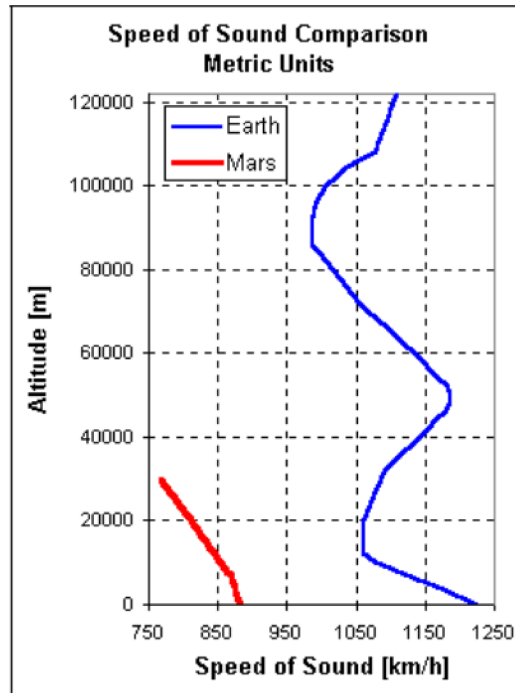


Figure 1.3: Speed of sound comparison Earth/Mars. ©Aerospaceweb

### 1.2.1 Mars/Earth atmosphere comparison

Mars atmosphere seems an exotic reality, although a similar condition could be found few km above our heads: in the Stratosphere. It is important to remember that the most critical parameter in this research it is the density of the Martian atmosphere itself, attested to be  $1.55 \cdot 10^{-2} \text{ kg/m}^3$  (Tab.1.1). The U.S. Standard Atmosphere divides the atmosphere into layers, where the lower three are modelled by the following equations<sup>3</sup>:

Earth Standard Atmosphere Model		
Upper Stratosphere	Altitude	$25 \cdot 10^3 \div 50 \cdot 10^3 \text{ m}$
	Temperature	$T = -131.21 + 0.00299 \cdot h$
	Pressure	$P = 2.488 \cdot \left[ \frac{T+273.1}{216.6} \right]^{-11.388}$
Lower Stratosphere	Altitude	$11 \cdot 10^3 \div 25 \cdot 10^3 \text{ m}$
	Temperature	$T = -56.46 \text{ }^\circ\text{C}$
	Pressure	$P = 22.65 \cdot e^{(1.73-0.000157 \cdot h)}$
Troposphere	Altitude	$< 11 \cdot 10^3 \text{ m}$
	Temperature	$T = 15.04 - 0.00649 \cdot h$
	Pressure	$P = 101.29 \cdot \left[ \frac{T+273.1}{288.08} \right]^{5.256}$

Table 1.2: U.S. Standard Atmosphere model for lower layers

Finding Mars conditions on Earth, although, is not as simple as finding a spot that has the same density, but it also has to be taken into account the difference between gravity

<sup>3</sup>[www.grc.nasa.gov/www/k-12/airplane/atmosmet.html](http://www.grc.nasa.gov/www/k-12/airplane/atmosmet.html)

forces: when speaking of a flying object, two main forces act onto it in opposite directions: the thrust and the weight; needless to say the first one has to be bigger than the second to lift the body and make it fly. To be able to find the perfect spot where a test flight could verify the possibility of performing a flight on Mars, it has to be defined the relationship between mean Martian density and its gravity:

$$\frac{\rho_{Mars}}{g_{Mars}} = \frac{1.55 \cdot 10^{-2}}{3.71} = 4.18 \cdot 10^{-3} \quad (1.4)$$

Supposing air as an ideal gas, to simplify the model in the first part of the analysis, and therefore applying the ideal gas law, the density  $\rho$  of Earth atmosphere can be defined as:

$$\rho = \frac{p}{1000 \cdot R_{spec} \cdot (T + 273.1)} \quad (1.5)$$

Where:

- $\rho$  [kg/m<sup>3</sup>] it is the air density;
- $p$  [kPa] is the air pressure;
- $R_{spec}$  [J/(kg K)] is the specific gas constant for dry air;
- $T$  [°C] is the air temperature.

For dry air  $R_{spec}=287.058$  J/(kgK). Gravity constant is defined by:

$$g = \frac{G \cdot M}{(R + h)^2} \quad (1.6)$$

where:

- $G=6.67 \cdot 10^{-11}$  [Nm<sup>2</sup>/kg<sup>2</sup>] is the universal gravity constant;
- $M$  [kg] is the mass of the planet;
- $R$  [m] is the radius of the planet;
- $h$  [m] is the height at which the object is positioned with respect to the planet surface.

Supposing that  $h \ll R$ , then it can be neglected and gravity can be considered constant as:

$$g_{Earth} = 9.81 \text{ m/s}$$

Matching  $\rho/g$  on Mars and on Earth and resolving the system for the previous pressure and temperature equations<sup>4</sup>, collected in Table 1.2, it can be identified that, at an altitude of 24.9 km from Earth surface, the ratios are equal for the two planets; that corresponds to a point, that will be call point **M** in the Lower Stratosphere with the following characteristics:

---

<sup>4</sup>Unit of measurements:  $h$ =[m],  $T$ =[°C],  $p$ =[kPa].

- $\rho_M = 4.10 \cdot 10^{-2} \text{ kg/m}^3$
- $T_M = -56.46 \text{ }^\circ\text{C}$
- $p_M = 2.55 \text{ kPa}$

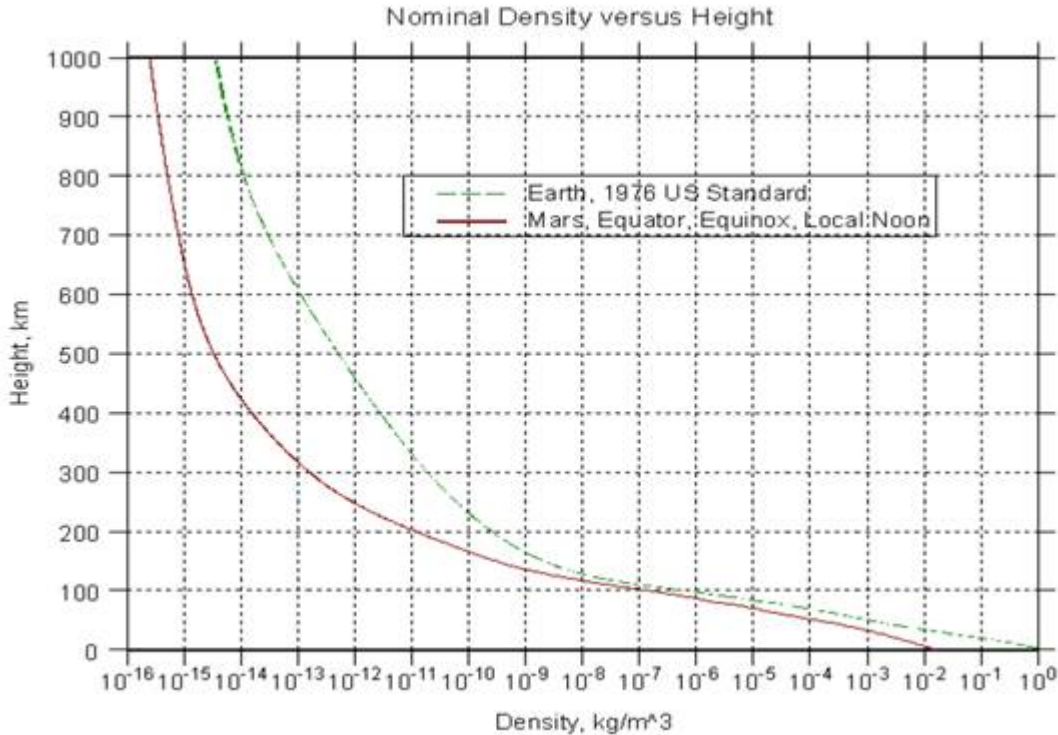


Figure 1.4: Density comparison Mars/Earth Atmosphere. ©NASA

Knowing this, it is possible to develop a set of experimental campaigns that aim to fly around point **M** on Earth before going directly on Mars. Some projects are aiming for this type of testing while developing Martian aircraft, as it will further be discussed in section 1.3.2. Albeit, this kind of tests could turn out extremely unruly for UAV in the first design phase, given that the great distance between the object and the control facility could prevent from intervening if anything goes wrong.

A remarkable difference between the point **M** and the Mars atmosphere is, not only the air composition, but also the speed of sound. Referring to Figure 1.3, it can be seen that the speed of sound of point **M** is higher than the one at 0 m level on Mars surface. This means that, to be able to fly smoothly on Mars, in subsonic speed range ( $Ma < 1$ ), the drone should fly at lower speeds than the ones that would be allowed on Earth to achieve the same fly regime.

### 1.2.2 Effect of Mach number

As previously said, Mach number, mathematically defined by Equation 1.1, is an important quantity that has to be taken into account when speaking about designing a flying system. The Mach number describes the regime of the flow of air around a flying body: as a body flies in the air, air particles tend to get compressed; this compression gets higher with respect to the body velocity and gets critical when the speed of the object is

equal to the speed of sound in that particular medium. When this condition is reached, there could be the formation of a shock wave that expands and affects the lift and the drag forces of the flying object. In late 19th century flight regimes, based on their Mach numbers, were subdivided as:

1. **Subsonic**( $Ma < 1$ ): air compressibility effects can be ignored. Example: commercial turbofan aircraft;
2. **Transonic**( $Ma = 1$ ): drag increases, Mach value easily fluctuates around 1 making this condition critical;
3. **Supersonic**( $1 < Ma < 5$ ): important compressibility effects, generation of shock waves on to the object surfaces. Example: Concorde aircraft, gun bullet;
4. **Hypersonic**( $Ma > 5$ ): some part of the flying object energy heats the surrounding air, modifying chemical bonds between nitrogen and oxygen, transforming air into an ionized plasma. The object has, therefore, to be insulated from the high temperatures. Example: spacecraft.

The project of a Martian drone will be designed to fly in a subsonic regime while on Mars. This will put a strong boundary to the speed of the rotor since the speed of sound on Mars is smaller than the one of Earth and it will have to be taken into account when effectuating performance tests on Earth.

### 1.2.3 Effect of low Reynolds number

As stated before not only Mach number has to be taken into account when flying but also Reynolds one. Reynolds number is a powerful tool to understand the nature of flow around a moving object, it is directly derived by the ratio of inertial forces and viscous forces, generated by the movement of air particles around a moving object. These forces depend highly on the characteristics of the medium; usually, viscous aerodynamic forces create a boundary layer of air that sticks to the object when this one is moving with respect to the medium.

Lower atmosphere density on Mars will cause the same airfoil to work at lower Reynolds than on Earth, this may cause some instability problems to the aircraft. Reynolds number are usually classified in low Reynolds number or high Reynolds number and tied with the concept of laminar and turbulent flow; anyway, no absolute transition value is given since Reynolds number highly depends on the type of medium took into account. Some studies were conducted to analyse how low Reynolds number affects the flow of the air around a wing and the boundary layer, changing the actual shape of the flying object as shown in Figure 1.5. This figure refers to a research conducted to study low Reynolds flight in high subsonic state [7]. It can be seen that what happens when a wing flies in a low Reynolds condition is that air forms a laminar bubble of separation that arises when it encounters an adverse region of pressure. The flow that separates from the bubble is really unstable and it transitions rapidly from a laminar flow to a turbulent flow that will later reconnect with the surface of the foil.

It has been seen that at constant subsonic Mach number, lowering the Reynolds number consequently leads to a decrease in the maximum lift coefficient, causing a downfall in the efficiency of the airfoil. Furthermore, the separation bubble increases while lowering

Reynolds number, causing a decrease in the overall performances of the aircraft.

To overcome these problems, the more immediate solution is to keep Reynolds number as high as possible, modifying the only adjustable parameter  $L$ , that practically means building a larger rotor.

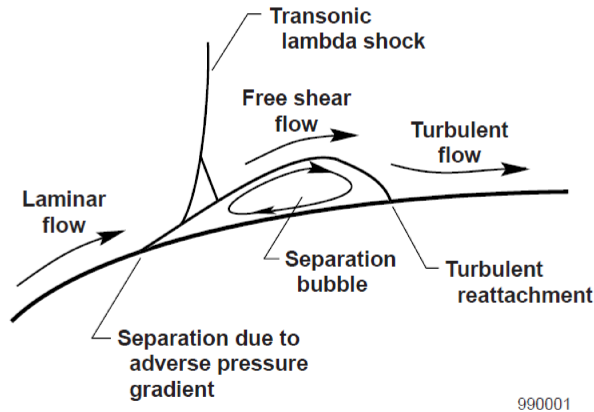


Figure 1.5: Laminar separation bubble at low Re. ©NASA

## 1.3 State of the art

Flying has always fascinated the mankind, but in more recent years a new challenge was set: flying in a different atmosphere than ours. Quickly the focus of this experiment was set on Mars, the Red Planet. The research in this direction was firstly conducted by NASA, but during the years parallel investigations were performed by other companies all around the globe.

### 1.3.1 The American prototype

NASA was the first company to launch the idea of a Mars flight. This idea has finally seen the light in 2018 when the Mars Scout Helicopter was revealed to take part in the *Mars 2020* mission launch. At the beginning, it was Ames Research Center, one of the ten active NASA centres in the United States, that started looking for possible solutions for developing an aircraft prototype able to perform a flight on Mars. The first steps were lead through university grants and resulted in some scientific papers that today set a solid base for this kind of projects. The most relevant ones were produced by the University of Maryland: "Hover Performance of a Small-Scale Helicopter Rotor for Flying on Mars" [8] and "Design of a Martian Autonomous Rotary-Wing Vehicle" [3]. The first one focuses on the most suitable blade profile for a Low Reynolds Martian flight and its performances, while the second one gets into the details of a complete design of an extra-terrestrial helicopter. In particular, in this second paper it could be found the primitive design of what will become the centre mechanism of the MHS: the control yaw swash-plate. Before these articles were published, NASA was, in parallel, exploring the feasibility of sending other types of aircraft on Mars such as: multi-rotors drones, fixed-wing planes or a hybrid between the two (tilt-copter). These other types of aircraft were discarded for different reasons: in particular drone technology was still being developed

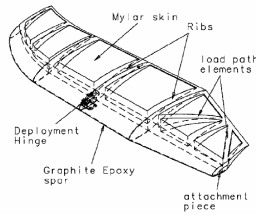
and was not fully stable with respect to the helicopter one, at the beginning of the 21<sup>st</sup> century; moreover, the multi-rotor drones are wider than a coaxial helicopter, therefore more difficult to transport as a mission payload. Early experiments were conducted on a not optimized blades, as described by Table 1.3, in a vacuum environment to test and acquire performance data. The first test-bench approach tested thrust force, the force causing the mass to be lifted, while propeller torque was being calculated indirectly from motor characteristic, as it will be further explained in section 2.2.2. As studies advanced, space rated precision instruments were used to check previously collected torque data and acquire simultaneously thrust and torque.

	Isolated Rotor Test[9]	Maryland University Mylar Prototype [3]	Air Recirculation Test ([10],[11])	Maryland Carbon Fiber Propeller [8]
Number of blades	4	2+2 coaxial	2+2 coaxial	2
Rotor Diameter [m]	2.438	4.266	1.016	0.4572
Disk Loading [N/m <sup>2</sup> ]	4	6.49	-	-
Tip Mach number	0.65	0.625	-	0.42
Tip Reynolds number	$5.49 \times 10^4$	$6.48 \times 10^4$	-	$5 \times 10^4$
Blade Chord[m]	0.3048 from 40% radial station outwards	0.670	-	0.0508
Rotor solidity	0.191	0.1585(each rotor)	-	-
Blade linear twist[°]	0 up to 40% span out $\pm$ from 40 % to 100 %	0	-	0°
Blade weight [kg/blade]	0.355	-	-	-
Outer Blade Span Airfoil Section	Eppler 387	-	-	-
Blade construction	Milled foam fairing with internal cavities; circular graphite tube spar across the span of the blade	Single box beam spar in graphite epoxy with transverse rib structure, wrapped with Mylar skin and Nomex honeycomb core	Off-the-shelf RC 40x22 super-class propeller manufactured by Biela Propeller Company, built in epoxy resin.	Carbon fiber blades and epoxy resin.
First Fund. Flap Mode	1.264 per rev	1.15 per rev	-	-
First Fund. Lag Mode	1.118 per rev	3.6 per rev	-	-
First Fund. Torsion Mode	2.310 per rev	-	-	-
Rotor Hub configuration	Rigid cantilever hub, with tension/torsion straps,dry contact pitch bearings and pitch arms at % 5 station.	Cantilever suspension connect to a collective-yaw shawsplate, control to move tip and fold the blade.	Rotor Hub built in the blade itself in wood. Coaxially coupled with another propeller of the same type, spinning in the same direction or in the opposite direction.	Polymeric hub, with possibility to change pitch; blades are fastened with screws to the hub.

Table 1.3: Blade evolution NASA



(a) Isolated rotor testing blade. [9]



(b) Prototype of composite blade [3]



(c) Off-the-shelf rotor used for recirculation test. ©Smigła Biela

Test campaigns for this particular project suffered a shutdown in 2007 and were started again only in 2014 with a brand new project sponsored and co-developed by the company AeroVironment. New experimentations got a full spectrum of the performances of the future helicopter. In order to reproduce Martian atmosphere as best as possible, setups were tested in JPL's environmental chamber. JPL's environmental chamber is a stainless steel cylindrical facility with an internal diameter of 7.62 m and a height of 26 m, where air composition, temperature and density could be controlled. It is important to recall that NASA focused large part of the research on air recirculation problems, due to a rotor spinning inside a closed vacuum chamber[11]. This kind of experience highlighted a strong recirculation in the chamber that influenced the thrust measurements, and it underlined the importance of a study of the effect that the propeller has on the inside flow of the air in any chamber used for this kind of tests in order to be sure of the results got. During the recirculation experience, the vacuum pump was not used, since JPL's and NASA's team believed that the density of the air would not influence the recirculation effect. Afterwards, this theory was proved, by doing the same experience in a Mars-like atmosphere. This set of tests showed that an inverted propeller position in testing (thrust down, wake up), with respect to an upright position, had a strong impact on reducing the so-called ground effect. Ground effect is defined, by the Cambridge Aerospace Dictionary [12], as:

*"Increased wing lift when flying in close proximity to the ground, especially with low-wing aircraft."*

In particular, in order to avoid any ground effect, the propeller was positioned with 2 m offset with respect to the axis of the chamber and at 3 m height from the floor. During the different test runs two main setups were used: a column one, called Mars Rotor Test Stand (MRTS) and a cantilever stand. The first one was used for the first tests (2002-2007) consisted of a cylindrical column ( $\text{Ø}32.4$  cm) bolted to a base plate ( $1.22 \times 1.22$  m<sup>2</sup>). It was equipped with a potentiometer to control the rotor RPM, three load cells and 2 accelerometers mounted 90 degrees apart.

The second test stand was particularly designed to fit the JPL's environmental chamber, it was made of a cantilever arm that could be used in three different configurations: locked-down, swinging and as a gimbal. The swinging configuration, the arm was able to swing in a horizontal plane to simulate forward flight and to test aero-dynamical effects such as edgewise flow. The third and last configuration was mainly used to test control inputs to regulate the pitch and the roll angle acquired from tests with the previous configurations.

NASA released their success in achieving a first controlled flight in JPL test chamber in 2016 [13]. The flight was possible by connecting all the electronics components needed for the controller to the ground, in doing so the enlightened weight of the drone was

comparable to the final weight it will have when subjected to the Martian gravity field. For this particular experience, the vacuum chamber was evacuated from the air and filled with CO<sub>2</sub>; until this moment, all tests hypothesized that composition of the air would not affect the aerodynamic performances of the drone as it was correctly found out.

The final product of this experimental campaign was revealed in 2018: the Mars Helicopter Scout [1]. It was defined as a technology demonstrator, made with the goal to demonstrate the possibility of a take-off and flight of an UAV in the Mars Atmosphere, but without any other scientific purpose. Each flight is supposed to last 90 seconds, and it is designed to perform 5 flights over a range of 30 sols. Flights will only happen during early mornings, when Martian atmosphere density is supposed to be between 0.016 kg/m<sup>3</sup> and 0.0175 kg/m<sup>3</sup>, the wind up to 5 m/s and the temperature around -50 °C. Although time constraints given to the experimentation on Mars seem really strict, they are imposed by technical difficulties. The 90 s limit is dictated by the overheating of the motor, it is possible to imagine that the insulation required to shield electrical components from dust and rigid temperature is not well suited for the aeration of the motor, and so it forbids the natural cooling of the working motor, that is already reduced by the low heat conduction of the Mars atmosphere. The other important boundary set is the total amounts of flights that the MHS will be able to do on the Mars surface, this limit was set by NASA itself: the MHS was not intended to take part in *Mars 2020* mission until late 2018, so some modifications had to be done to the rover in order to make it a reliable base station for the MHS. When the helicopter will be flying, the rover will not be able to perform other tasks but focusing on the communication with the small aircraft, so in order not to undermine the work of *Mars 2020* rover, the total number of flight had to be limited.

An autonomous flying object represents a great hazard towards the robotics mounted on the *Mars 2020* rover: to prevent any damage, the MHS will be deployed by the rover in a plane and then the rover will retire 1000 m from the MHS position. The flights are already programmed on the onboard electronic presents on the MHS, but some key parameters will be directly sent from Earth. These real-time parameters would not include any information on the Martian weather, because even if a weather station is present on the rover, the time needed to receive and send data from Mars it is way to long<sup>5</sup> to be real-time effective on the control of the helicopter.

JPL is confident in saying that the MHS should be able to survive and complete its 5 flights, and it is hoping that it may survive even after in order to re-negotiate its use for future experiments.

---

<sup>5</sup>"The data rate direct-to-Earth varies from about 500 bits per second to 32,000 bits per second, roughly half as fast as a standard home modem.", states NASA [[www.marsmobile.jpl.nasa.gov/msl/mission/communicationwithearth/data/](http://www.marsmobile.jpl.nasa.gov/msl/mission/communicationwithearth/data/)]

<b>MHS</b>	
Weight	1.8 kg
Number of blades	2+2 coaxial
Relative rotation	counter-rotating
Rotor diameter	1.21 m
Flap frequency	1.9 per rev.
Collective angle	from $-4.5^\circ$ to $17.5^\circ$
Cyclic angle	$\pm 10^\circ$
Maximum rotation speed	2800 rpm
Blade construction	Carbon fiber composite
Motor	46 poles brushless custom made
Sensors	2 IMU Inclinometer Altimeter Navigation Camera Return-to-Earth Camera

Table 1.4: MHS final characteristics

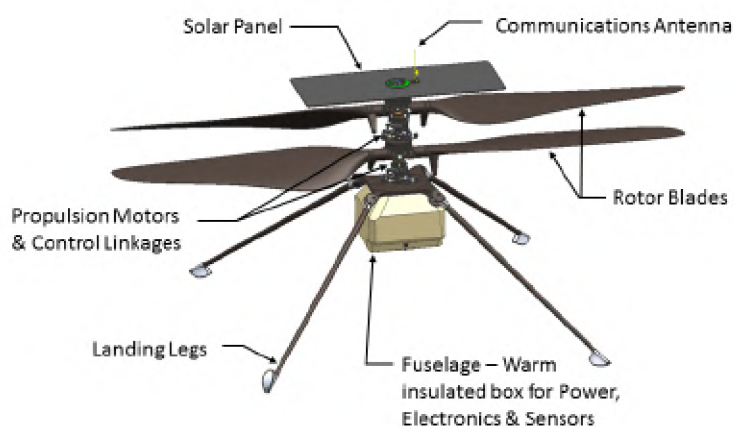


Figure 1.6: MHS final design [1]. ©NASA

### 1.3.2 The French experience

In a European perspective, there has been some attempts to fly a drone in a Martian atmosphere: the two most known are the co-axial drone conceived by ONERA and the fixed flying drone designed by Airbus . The first type is surely more similar to the one designed by NASA and it has the same pros and cons. ONERA in partnership with CNES developed an airfoil capable of flying on Mars maximizing the performances of the propeller and at the same time focused on developing a software for optimizing the structure of a multicopter drone and on analysing and testing the drone itself. CNES study was divided in two sections, developed by university students in 2015: the first consisted of generating a Visual Basic application capable of sizing the drone with respect to its hypothetical performances and the second part focusing on the design and testing of the drone itself. The first design parameters were the ones of a compact drone able to fly, carrying a 4kg payload, for at least 20 minutes a day [14]. All ONERA studies were done supposing a Reynold number of 3000. The configuration, that virtually made these requirements possible, is the following:

- AXI2826/10 motor;
- Beez2B 4S 10Ah battery;
- 2 Eiffel428 airfoils with a chord of 26 cm in a ducted fan.

The propeller was optimized to rotate at 8100 rpm in Martian atmosphere. Later an update of the same drone was proposed with a 4 blade Eiffel428 propellers of 30 cm diameter and a 200g total mass [15]. Following studies were orientated to find a new airfoil, smaller



Figure 1.7: Eiffel 428 blade with 26 cm chord. ©ONERA

and able to work properly in Martian atmosphere even without ducting. Before testing, the French company proceeded in building a first mock-up called MOSQUITO <sup>6</sup>, which highlighted some major instability problems in terrestrial air. The propeller testing was foreseen for December 2015: it should have been taken place in an environmental chamber, able to regulated pressure and the composition of its internal gas. The test bench was developed in partnership with a micro-mechanics industry, and it consisted of a horizontal ducted propeller, able to slide forward on a guide as the thrust increases. Attached to the sliding guide there is a dynamometer that provides thrust data. Other sensors that were

<sup>6</sup>Mars Original System for Qualitative Imaging and Tactical Operations

part of the testing bench are an encoder, a wattmeter and an anemometer. Despite all information published, the testing had some issue and it seems to have never taken place. The study seems to have continued focusing more on the 3D and 2D simulation for new blade profiles as it could be read in the more recent published article, in partnership with China Academy of Aerospace. [16].

French company Airbus, on the other hand, has developed a working aircraft called Perlan II: it is an ultralight fixed-wing aircraft able to soar in the stratosphere. Even if Martian exploration is not the first aim of this aircraft, the company has more than once strongly underlined the similarities between stratosphere environment and Martian atmosphere and they do leave an open window for using a slightly modified model for future missions on Mars.<sup>7</sup> The aircraft is engineless and its soaring capabilities rely completely on air currents, deriving from the combination of the Polar vortex with mountains winds. It weighs around 680 kg and it is 25 m large at its wing point. In September 2018, this aircraft broke the record for the highest human flight on Earth, reaching the altitude of 23.2 km, showing that its capabilities of flying on Mars are highly convincing. The main drawback of this project it is the size of the aircraft that would make it difficult to send it to Mars.

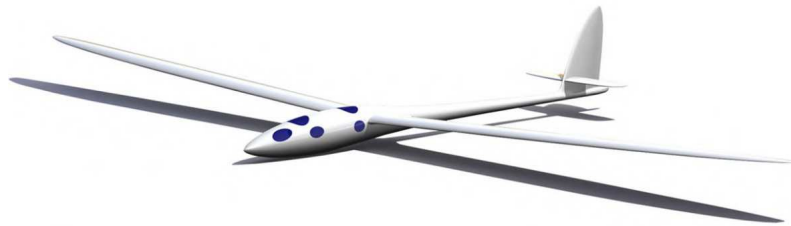


Figure 1.8: Perlan II model.©Airbus

### 1.3.3 University of Tokyo project

Some independent projects were developed in these last year for finding a best practice to define a suitable design and testing for a drone and in particular, a drone able to fly on Mars. One of the studies that is worth mentioning is the one conducted by a collaboration of Tokyo University and the Japanese ISAS [17]. This research puts the focus on the design and the study of a validation method for the performances of a Martian propeller. The final product is a test bench made with a pendulum-like architecture. The main sensor used is an inclinometer, an instrument able to measure angles with respect to gravity force direction. A previously found relationship between the inclination of the pendulum and the thrust of the propeller helped to compute the precise lift force generated by the blades in each moment. Since it is challenging to combine both thrust and torque measures in a single set up, the torque was not directly measured, but it was, instead, calculated through the current absorbed by the motor, as it was done in the first NASA tests. In fact, it is possible to say under certain hypothesis, further defined in section 2.2.2, that

---

<sup>7</sup>[www.airbus.com/newsroom/press-releases/en/2018/09/airbus-perlan-mission-ii-glider-soars-to-76-000-feet-to-break-ow.html](http://www.airbus.com/newsroom/press-releases/en/2018/09/airbus-perlan-mission-ii-glider-soars-to-76-000-feet-to-break-ow.html)

in an electric motor, torque and current are linked by the following equation:

$$Q = k_T(I - I_0) \quad (1.7)$$

where:

- $Q$  [Nm] is the motor generated torque;
- $k_T$  [Nm/A] is called torque constant and it is defined for each motor in its datasheet, based on its characteristics;
- $I$  [A] is the current absorbed by the motor;
- $I_0$  [A] is the no-load current defined in the specifications of the motor.

Some tests were conducted to define the feasibility of Martian co-axial helicopter. In recreated Martian atmosphere different propellers were tested using the pendulum test bench in these conditions:

- Mach number at tip  $\simeq 0.13$ ;
- Low Reynolds number ( $10^3 - 10^4$ ).

These experiences focused on finding how different blade profiles influenced aerodynamic forces, drag and lift coefficients in Martian atmosphere. It was hypothesized that, since at low Reynold numbers the drag on the surface of the blade it is significant, leaving a grooved surface would reduce torque forces. This assumption was found to be false and that grooves had small or no impact on the forces developed by the rotor. The author of the paper then proceeded to contemplate a first mass budget for a possible 60 g co-axial helicopter, divided as:

Mass Budget	
Control unit	11 g
Telemeter	8 g
Imaging Camera	15 g
Rotor	12 g
Fuselage	10 g

Table 1.5: Hypothetical 60 g drone mass budget.

This study sets some clear guidelines for all the attempts of building a Martian drone, that could be resumed in:

- Reynold number for blades should be as high as possible;
- Mach at tip should be in subsonic regime;
- Indirect measurements for torque are enough precise for first test campaigns.

### 1.3.4 Thales Alenia Mars Drone Project

The project for the development of Martian drone was proposed and started by Thales Alenia space, in collaboration with both the Mechatronic and the Aerospace engineering department of Politecnico di Torino. Thales Alenia Space project final aim is to develop a multicopter drone fully able to perform a flight on Mars. The choice to detach this research from the most common coaxial helicopter architecture, as used by NASA and ONERA, was fed by the great knowledge in drones mechanics and control, gained by this university over the years.

Two experimental campaigns were conducted: one in open air, conducted in the Politecnico headquarter of Verres and the second campaign of experiments was led by Thales-Alenia Space Italia (TAS-I), in Torino site. There, a vacuum chamber, able to reproduce Martian atmosphere conditions, was available to test the blade profile and the motor chosen. The blade selected for vacuum testing was a reproduction of the one built by University of Maryland and shown in their published article [8].

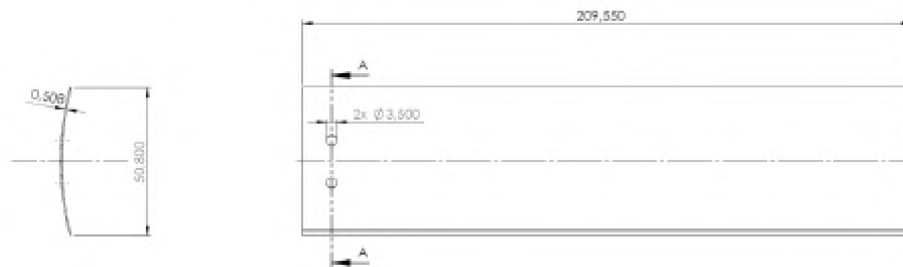


Figure 1.9: Carbon fiber replica of University of Maryland propeller used for Thales Alenia Space tests

During year 2018, several tests have been made to prove the capability to recreate and evaluate performances of the rotor described and used in the study of the University of Maryland [8]. The article, published by the University of Maryland, reports clear experimental data so it would be easy to understand if the propeller and the testing in TAS-I would be successful by comparing propeller performance with the already public results. This specific article was chosen not only because it had published clear performance results, but also because it is the one study that started the development of NASA's MHS project. The vacuum chamber that has been used for tests is TAS-I PHASE. This particular vacuum chamber has no thermal control, but it was found to be suitable for first tests whose main objective was to evaluate only the basic performances of the drone propeller. Ideally, to test the propeller, it would have been best to recreate a testing setup as close as possible to the one described in the above referred article. It was, although, not possible since the vacuum chamber used by the University of Maryland was vertically positioned, unlike TAS-I PHASE chamber. This led to a discussion of which setup could better measure the propeller performance, combining thrust and torque evaluation without losing precision. The found solution had to deal with mechanical constraints given by the limited dimensions of the vacuum chamber chosen and with the inevitable difficulty of working in a vacuum environment. The setup had to minimize friction and the presence of revolute joints, which suffer low pressure environments. Moreover, it was known, from the American research, that the thrust generated by this type of propeller would be really



Figure 1.10: Swing test bench in TAS-I PHASE vacuum chamber

small, if compared to the weight of the whole setup, hence it was chosen to set the whole test bench horizontally: in this way, gravity would not disturb the thrust force.

The most favourable solution, that was able to satisfy all the above demands, was a quadrilateral swing, supported by two lateral columns, holding up the measurement chain. This set up, photographed in Figure 1.10, was built to be able to test simultaneously thrust and torque generated by the propeller. The main problems that this kind of setup had to face were the aleatory vibrations applied to the structure and the impossibility to make the swing oscillate in a specific plane. To help increase structural and dynamic robustness, two guides were installed in the interior part of the swing to reduce oscillations. Vibrations were also due to the structure itself, it has to be said that the four cables suspending the setup were not easily tunable to achieve the same tension in all of them, causing issues when the propeller was spinning.

The setup previously described acquired both thrust and torque at the same time, as well as propeller speed and axial accelerations. Data were then compared to thrust and torque models generated starting from the University of Maryland study. Physical quantities were acquired with the most appropriate sensor, as shown in Table 1.6. Torque was measured by a torque meter, positioned between the motor and the propeller, while thrust was evaluated by a load cell, attached to the setup by a nylon wire and set in the rear part of the chamber, as it can be seen in Fig.1.11. Speed was acquired neither with the motor encoder nor with torque meter one. This choice was due to the digital acquisition system that would give a timeout error when the motor was spinning not fast enough with comparison to the acquisition rate of the encoder. It was then chosen to acquire feedback signals from motor Hall sensors. Moreover, temperature was checked with thermocouples in critical points of the set up: the chamber, the motor cover and the load cell. Chamber temperature was acquired to evaluate the density of air inside, while the sensors on motor and load cell were positioned to investigate thermal errors. Data were acquired through a NI DAQ board and stored by a Labview implemented code.



Data Acquired	Sensors
Thrust	Load cell
Torque	Torque meter
Longitudinal acceleration	Accelerometer
Perpendicular acceleration	Accelerometer
Motor speed	Hall sensor
Chamber temperature	
Load cell temperature	Thermocouples
Motor temperature	

Table 1.6: Summary of data acquisition for previous tests

The motor, for all previous tests, was driven by an ESC driver, through a voltage signal and with speed control loop enabled. In this configuration, a fixed voltage was forwarded to the motor supply, while a control voltage signal was forward in order to vary motor speed. It has been underlined that in these tests the voltage control signal never reached its maximum limit, meaning that the maximum speed possible  $\bar{\omega}$ , for the given motor voltage supply, was never reached, as it will be later discussed in section 2.2.2. The voltage control signal was generated as an analog output by the DAQ system and modified through PC interface in real-time with Labview.

Tests gave mixed results, because while the test bench was able to fully reproduce thrust forces in trend with the one of the American study, the same cannot be said for torque measurements. Tests could not be performed at the same speed used for Maryland's study for safety reasons, so to compare the data acquired by TAS-I with the American study, two trends were identified thank to the thrust and torque coefficients  $c_T$  and  $c_Q$  and the akin power parameter  $c_P$ . These coefficients are dimensionless numbers that are specific of a propeller profile in a given air density. There are different definitions of these coefficients, but the one used by Thales Alenia Space is the same used by Maryland University, defined as:

$$c_T = \frac{T}{\rho A \omega^2 R^2} \quad (1.8)$$

$$c_Q = \frac{Q}{\rho A \omega^2 R^3} \quad (1.9)$$

$$c_P = \frac{P}{\rho A \omega^3 R^3} \quad (1.10)$$

Where:

- $T$  [N] is the thrust force;
- $Q$  [Nm] is the propeller torque;
- $P$  [W] is the mechanical power of the rotor, as in  $P = Q\omega$ , making  $|c_Q|=|c_P|$ ;
- $\rho$  [kg/m<sup>3</sup>] is the air density;
- $A$  [m<sup>2</sup>] is the rotor disk area, as in  $A = \pi R^2$ ;

- $R$  [m] is the rotor radius;
- $\omega$  [rad/s] is the rotor speed.

For Maryland propeller the coefficient values were experimentally found to be:

$$c_T = 0.018$$

$$c_P = c_Q = 0.009$$

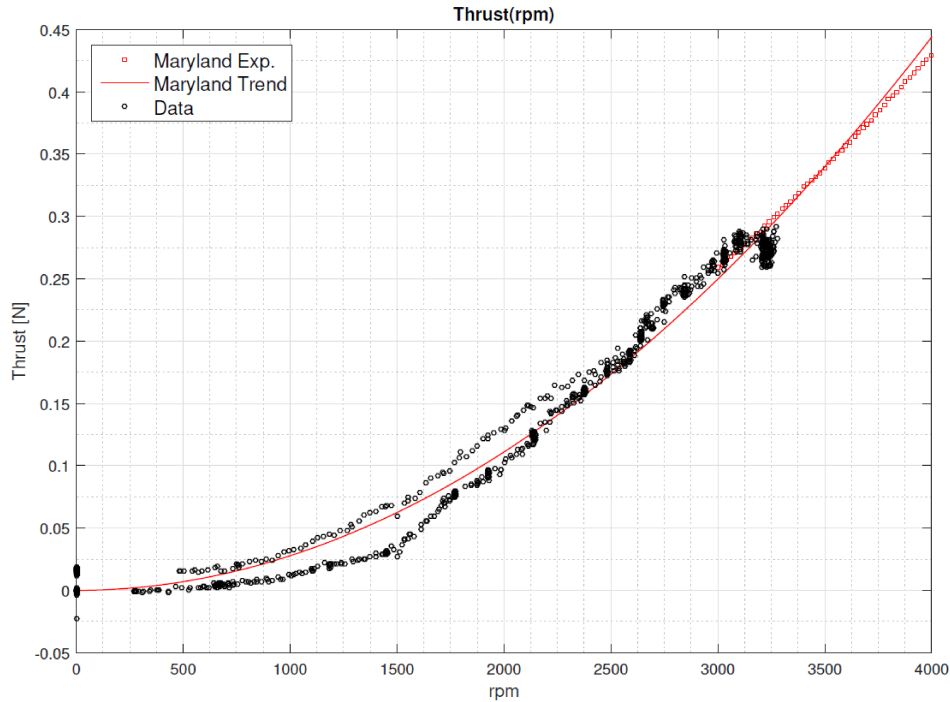


Figure 1.12: Thrust results comparison with Maryland experimental data

As it can be seen from Figure 1.13, the torque found in the Italian study is higher than the one expected. Furthermore, the standard distribution of torque data is extremely large with respect to the single point data acquired.

These results led to the conclusion that something was not working properly inside the vacuum chamber. Unluckily in a so enclosed and alien environment like the one inside the vacuum chamber, the troubleshooting process could be very hard to perform. Therefore some hypotheses were made on what could be the cause for which torque measurement was inaccurate:

- The torque meter could not be suited for vacuum testing, since it could contain some oils that with low pressure increase viscosity and increase the system friction;
- The motor could be responsible to increase the torque, either because cables from its ESC driver carrying voltage supply are too long (ESC was located outside the chamber for safety reasons) or due to an erroneous functioning of the motor itself;
- The setup could be affected by high mechanical noise due to its swinging motion;

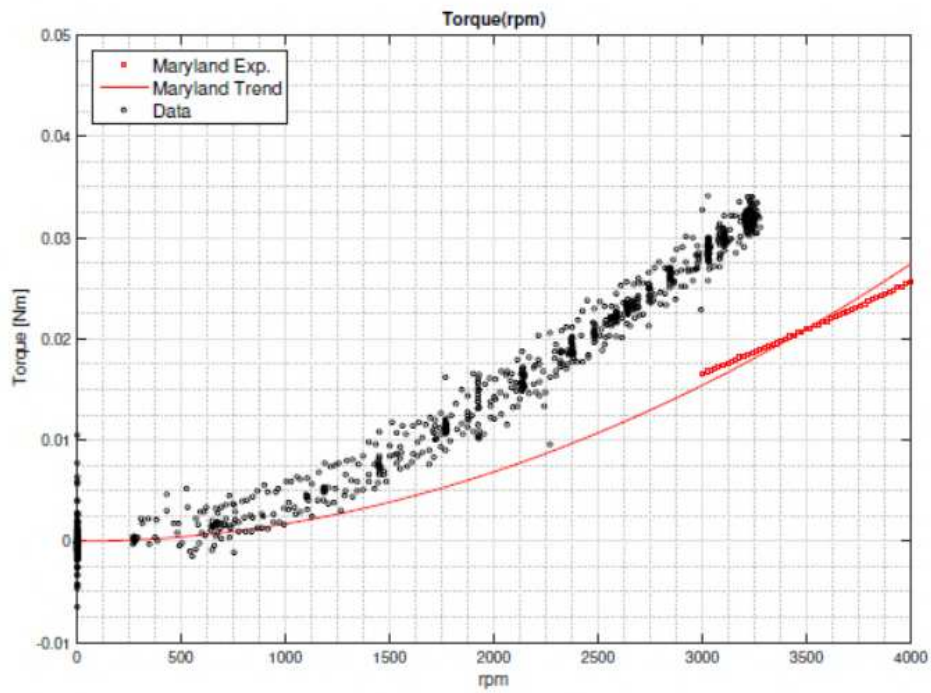


Figure 1.13: Torque results comparison with Maryland experimental data

- There could be a resonance problem on the setup, since no deep investigation on vibrations was done previous to tests;
- Coupling and mechanical connections could work against the propeller and therefore contaminate the results.

These hypotheses will setup the ground for the experimental investigation that will be conducted in the next chapter.

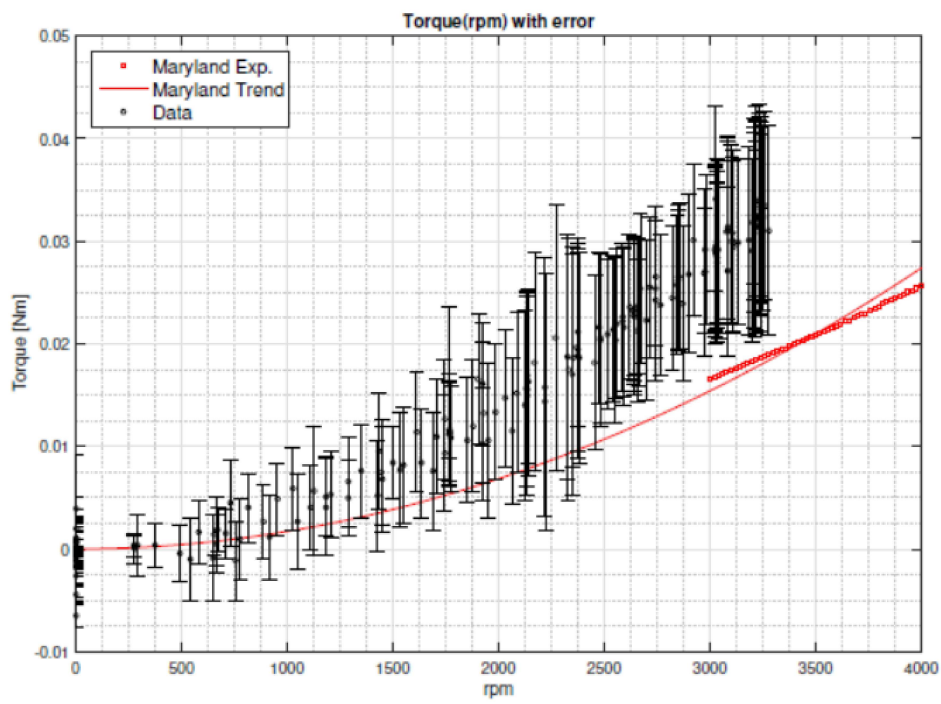


Figure 1.14: Acquired torque error distribution

## Chapter 2

# Performance Accuracy Investigation

In the following chapter, it will be laid out the path that was followed to understand which was the main cause of the wrong measurements found by previous TAS-I's studies.

The first part of the chapter will focus on the definition and mathematical characterization of the single components used in the setup, as well as a deeper insight in reproducing Martian condition in a vacuum chamber. Afterwards, it will be discussed a possible new torque setup that could increase data accuracy and eventually results from a new experimental campaign, led with a different test setup will be examined. Eventually a hint for a new thrust setup will be discussed.

### 2.1 Vacuum Testing

The critical parameter for testing a Martian drone is the air density in which its performances are evaluated. One of the most common ways to achieve a lower air density on Earth is by using a vacuum chamber or an environmental chamber. Vacuum chambers are structures provided with pressure control, while environmental chambers are also equipped with thermal control of the inside air.

A vacuum chamber is a system, most commonly, composed of a main rigid enclosure, a pumping system, and a pressure sensor. When the chamber undergoes air evacuation, the gradient of pressure between the inside and outside environment increases, the structure incurs in high mechanical stresses and therefore the chamber has to be designed to be sturdy enough to not be damaged by the repetition of air evacuations cycles. The most common materials used for building vacuum chambers are: stainless steel, aluminium, brass, high-density ceramic and glass.

The main body of the chamber is connected to a pump that represents the actual system that makes vacuum possible in this the main body. Vacuum pumps generate vacuum from moving the existing air outside the container and decreasing the overall pressure inside of it. They are categorized by their working principle. The first division is between gas transfer and gas binding pumps. The first ones are a non-limited in time type of pump, while the other type needs to be regenerated after a specific time period. Gas transfer pumps are furthermore classified in: positive displacement pumps and kinetic pumps. The difference between these two categories is that the displacement type transfers gas from a sealed environment to the atmosphere, while the kinetic type moves the gas by accelerating it in a precise direction, mechanically or through water steam. The sort of pump needed depends on the quality of the vacuum requested for the operations

With today technology actual vacuum is still impossible to reach but a suitable artificial approximation can be achieved. The quality of the air evacuation depends primarily on the sealing of the vacuum chamber itself and on the performances of the vacuum pump attached. It has to be said that the word *vacuum* do not describe a unique atmospheric condition: vacuum environment has been subdivided into different quality categories, defined by their pressure range as shown in Table 2.1.

Quality	mbar	Pa
Outer Space	$1 \times 10^{-17}$ to $1 \times 10^{-6}$	$1 \times 10^{-15}$ to $1 \times 10^{-4}$
Extreme Ultra-high Vacuum (EHV)	$> 1 \times 10^{-12}$	$> 1 \times 10^{-10}$
Ultrahigh Vacuum (UHV)	$1 \times 10^{-12}$ to $1 \times 10^{-9}$	$1 \times 10^{-10}$ to $1 \times 10^{-7}$
Very High Vacuum	$1 \times 10^{-9}$ to $1 \times 10^{-6}$	$1 \times 10^{-7}$ to $1 \times 10^{-4}$
High Vacuum	$1 \times 10^{-6}$ to $1 \times 10^{-3}$	$1 \times 10^{-4}$ to $1 \times 10^{-1}$
Medium Vacuum	$1 \times 10^{-3}$ to 10	$1 \times 10^{-1}$ to $1 \times 10^3$
Low Vacuum	10 to $1 \times 10^3$	$1 \times 10^3$ to $1 \times 10^5$
Std. Atmospheric Pressure	$1.013 \times 10^3$	$1.013 \times 10^5$

Table 2.1: Vacuum Quality Ranges

Vacuum chambers are often used in the spatial industry to recreate extra-terrestrial environments thanks to their simple and straightforward working principle. Vacuum environment sparks although some issue that have to be taken into account before placing any kind of device inside the chamber. Heat exchange is not the same as the one on Earth: in absence of atmosphere, the heat is only exchanged by irradiation or conduction, reducing cooling effects derived by the motion of air. Moreover, vacuum has a not negligible effect on materials such as: metals, alloys, polymers and lubricant. These materials can undergo a process of *outgassing*, meaning that gases, trapped inside material in standard atmosphere conditions, could escape the surface when subjected to low pressure, changing physical and chemical conditions of the vacuum achieved. In order to prevent any problem that may be linked to this process, all components and materials have to be *vacuum rated*, before being subjected to vacuum environments.

In order to reach the Martian atmosphere density, a vacuum chamber has to be depressurised to a pressure value corresponding to mean Martian air density. Supposing the air inside the chamber can be approximated by ideal dry air model, then the density of the air and the pressure are tied by the formula of perfect gas, expressed as:

$$p = R\rho T \quad (2.1)$$

where:

- $p$  [kPa] is the pressure required to achieve Martian density;
- $R$  [kJ/(kg K)] is the gas constant specific for dry air  $R=0.286$ ;
- $\rho$  [kg/m<sup>3</sup>] is the air density demanded;
- $T$  [K] is the air temperature measured.

<b>Dimensions</b>	
Internal Diameter	800 mm
Available Space	600x1200x570 mm
<b>Vacuum Pump</b>	
Model	Pfeiffer Duo 20
Min. Pressure	$1 \times 10^{-1}$
Flow Rate	20 m <sup>3</sup> /h
<b>Pressure Sensor</b>	
Model	Granville Philips 375 Convectron
Type	Gauge (Relative)
Min. Measurable Pressure	$1 \times 10^{-3}$
<b>Electronic Connectors</b>	
<ul style="list-style-type: none"> <li>- 8 RS232 connectors with 9 pin</li> <li>- 9 RS232 connectors with 15 pin</li> <li>- 1 RS232 connector with 25 pin</li> <li>- 4 BNC connectors</li> </ul>	

Table 2.2: TAS-I PHASE technical data

For Martian air purpose, the density required is  $1,55 \cdot 10^{-2}$  kg/m<sup>3</sup> (Tab.1.1), so the pressure needed on Earth to reproduce these conditions, at mean 20°C, is  $p \simeq 1,3$  kPa=13 mbar. It is important to underline that pressure  $p$ , used for tests, is not the actual one that is found on Mars at "sea level". This is caused by the different composition of air on Earth and on Mars, in fact Martian air is mainly composed by CO<sub>2</sub>, and therefore has a different  $R$  coefficient than the one of dry air.

TAS-I PHASE vacuum chamber, represented in Figure 2.1, is the stainless steel vacuum chamber chosen to perform the propeller testing in Thales Alenia Space facilities. The chamber is equipped with two doors, one of which has a porthole that enables to check the status of the interior even when the doors are sealed. Since most experiments need a stable plane to set them up, the inside of TAS-I PHASE chamber is not purely cylindrical but it has two sliding rails in the lower half of the chamber. The sliding rails give the opportunity to insert two removable steel perforated plates to set up and screw in place different devices. On the side of this vacuum chamber there are three vacuum flanges that made available electrical serial connections which provide the only possible link between the inside electronics and the outside environment.

The vacuum pump connected to TAS-I PHASE chamber is a Pfeiffer duo 20 rotatory vane pump. This kind of pump goes under the categories of gas transfer pumps and positive displacement pumps. The pump is connected through a ball valve and a filter to the chamber itself. This system works best in the low and medium vacuum range. The working principle on which is based this pumping technology is an eccentric rotor with vanes, rotating in a fixed housing. Gases are divided in two different parts of the chamber by the vane that moves due to centrifugal force. The gas that comes through the inlet valve (Fig.2.2, right valve) enters the pump chamber and when it is reached by the second vane, it is compressed until the pressure built is able to open the outlet valve

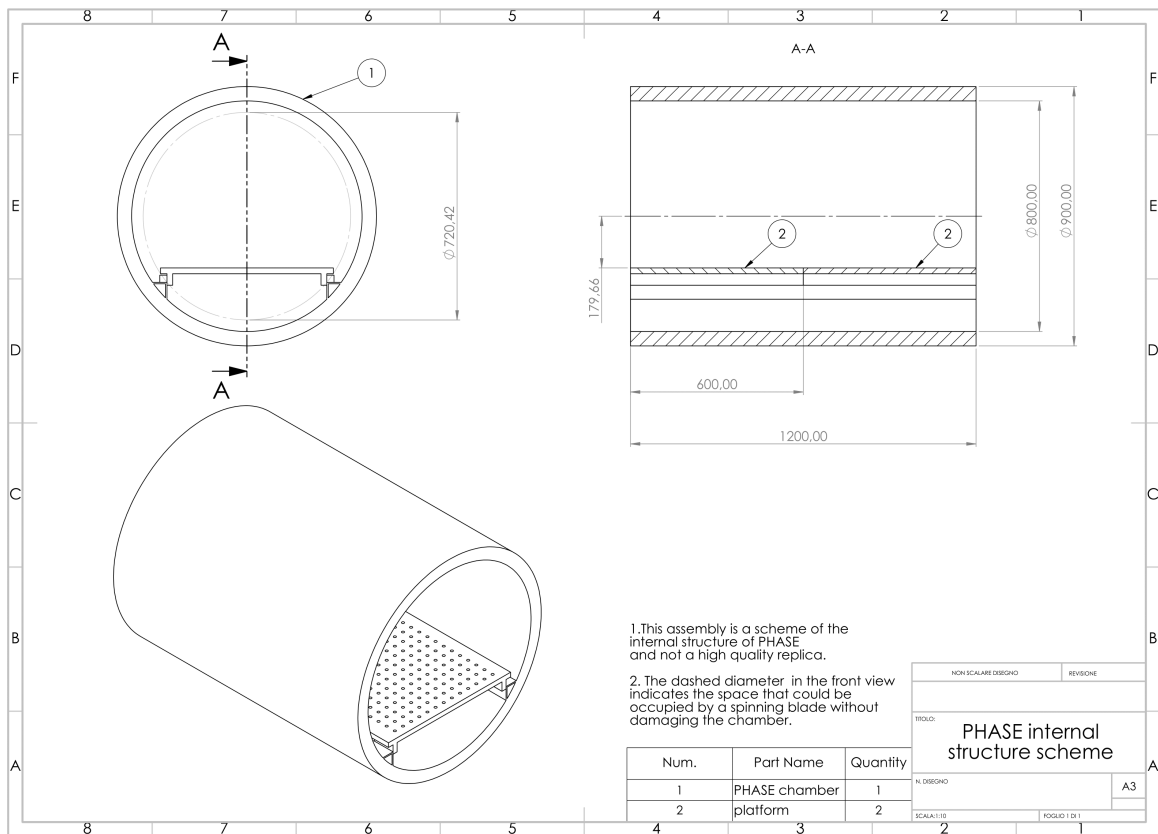


Figure 2.1: Internal PHASE structure scheme

against atmospheric pressure. The outlet valve is oil-sealed so that when it is opened a small amount of oil can cover the vane, lubricate it and protect it from the housing. This type of oils are also known as operating fluids and they prevent the mechanism from failing due to high mechanical pressures or continuous operations.

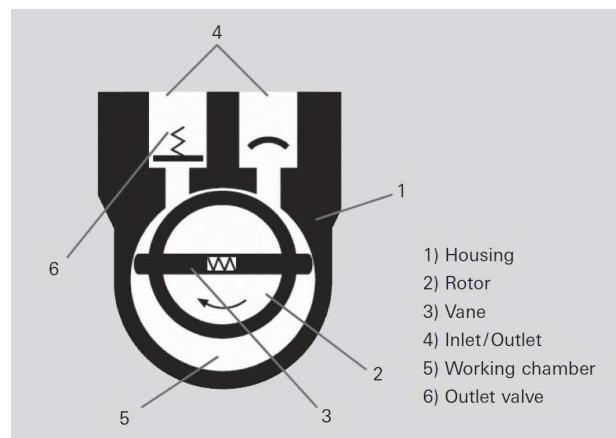


Figure 2.2: Working principle rotating vane pump. ©Pfeiffer

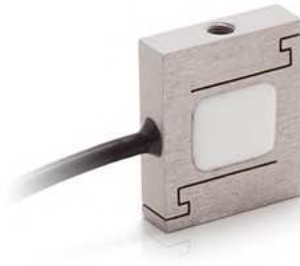


Figure 2.3: S beam miniature load cell. ©FUTEK

## 2.2 Test Bench Components

In the following section, all components used for the previous test, as described in Figure 1.11, will be listed in order to gain a deeper knowledge of their characteristics and working principle.

### 2.2.1 Load cell

A propeller generates two main physical quantities: a thrust force and a torque. To measure thrust, a load cell was used. Load cells are force sensors and are divided in different categories based on the type of application they are used for. The one that was used for testing the Martian propeller is a miniature S beam load cell with maximum rated load 50g manufactured by FUTEK Inc. S beam-type cells work on deformation principle, their name is due to their specific shape that recalls the letter S. In the middle segment of the beam cell there is the so-called *spring body* of the sensor: it is a metal piece that gets deformed when it is subjected to a load and comes back to its original shape whenever the load is released. This deformation process is precisely measured by strain gauges glued to the metal. Strain gauges define most commonly devices that when subjected to small deformations vary their resistance giving an electric output signal proportional to the deformation. The elastic rigidity of the strain gauges defines the nominal load of the load cell. Frequently, on the spring body, there are four strain gauges positioned in order to have two of them working in compression and two in extension; the four of them are connected electrically in a Wheatstone bridge and powered by a supplied voltage signal.

Wheatstone bridge circuits are well known for supplying accurate measurements, being able to compensate temperature variation, and keeping costs relatively low.

S-beam load cells are used both in tension and compression operations; in particular, they are well known for being able to reject side loads with high precision. This last characteristic makes this type of cells very well suited for the analysis of a propeller thrust since, even if theoretically the thrust should be always perpendicular to the propeller, other environmental factors can deviate it or introduce side errors.

Load cell datasheets usually provide three main error parameters:

- $\epsilon_L$ : non-linearity error;
- $\epsilon_H$ : hysteresis error;

- $\epsilon_R$ : repeatability error.

All of them are defined as a percentage of the rated output (RO), expressed in mV/V, that defines the ratio between the load cell output to the supplied voltage.

Some measuring errors could be also due to temperature change that induces a variation in the Young modulus ( $E$ ) of the material of spring body, modifying the deformation  $\epsilon$  given with same applied stress  $\sigma$ .

$$\sigma = E \cdot \epsilon \quad (2.2)$$

Linearity errors are also common and most often due to the geometry modifications induced by uneven loads applied. These errors could be compensated by adding specific resistances outside the Wheatstone bridge, as shown in Figure 2.4.

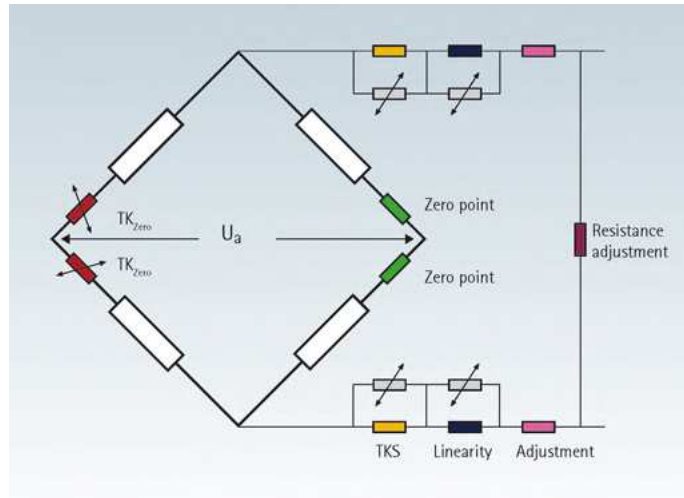


Figure 2.4: Wheatstone bridge of a load cell

The total accuracy of this load cell can be found, using the accuracy equation that ties the error parameters with the force measured:

$$\epsilon > \sqrt{\epsilon_L^2 + \epsilon_H^2 + \epsilon_R^2 + \left(\frac{\epsilon_Z \cdot L \cdot N}{W} \cdot T\right)^2 + (\epsilon_S \cdot T)^2} = 0.25\% \quad (2.3)$$

where:

- $\epsilon_Z$  [%/°] is the temperature effect on the balance of the zero point,
- $\epsilon_S$  [%/°] is the effect of temperature on span;
- $T$  [°] is the range variation of temperature of the load cell;
- $W$  [g] is the maximum weight measured;
- $N$  is the number of load cells used;
- $L$  [g] is the rated capacity of the load cell.

In this particular setup, the cell is connected to the propeller thanks to a nylon thread, attached with a ring screw to the torque meter base, as it can be seen in the CAD reproduction in Figure 1.11. This thread was previously tuned to give an offset load to the cell, making sure that the working point of the load cell is far away from the zero point. This precaution has to be taken because measuring errors for load cells tend to be higher when evaluating forces close to zero.

## 2.2.2 Motor

The motor chosen to power the Martian propeller was a Faulhaber 2264W 024 BP4, which is a brushless DC servomotor with 4 poles.

A brushless DC motor (BLDC) is an electric motor that derives from DC motors: in DC motors the windings, housed in the rotor, are externally powered by electric brushes and commutator rings. In the case of a brushless motor, instead, the rotor is made by permanent magnets while the stator accommodates electric coils. The commutation, that is mechanical in DC motors, becomes electrical in a brushless motor. Stator coils are energized by an external voltage source and by becoming electromagnets are capable of interacting with the rotor permanent magnets. The rotor of this motor present 4 poles, alternated N-S-N-S, that will interact with the inverse poles energized in the stator. The electrical commutator enables to energize different coils at different times, making the rotation continuous. The coils in the stator are usually disposed in order to be three at  $120^\circ$  and correspond to the phases of the motor: motor with this configuration are called triphase. DC brushless can be divided between sinusoidal BLDC or trapezoidal BLDC, depending on the shape of the induced emf (electromagnetic force) generated when the coils are energized. The motor used for Martian testing is a trapezoidal BLDC. Emf in different phases are separated by a time delay, since the coils are not energized all at once. Following the voltage profile, a distinctive current profile for each phase can be distinguished as described in Figure 2.5. The trapezoidal profile corresponds to the ideal condition where all the power supplied to the motor is transmitted to the 3 phases; this condition will correspond to a distinctive speed  $\bar{\omega}$ . Anyway, it is possible to modulate the speed to reach a value  $\omega < \bar{\omega}$  by chopping the voltage directed to motor phase at a certain frequency.

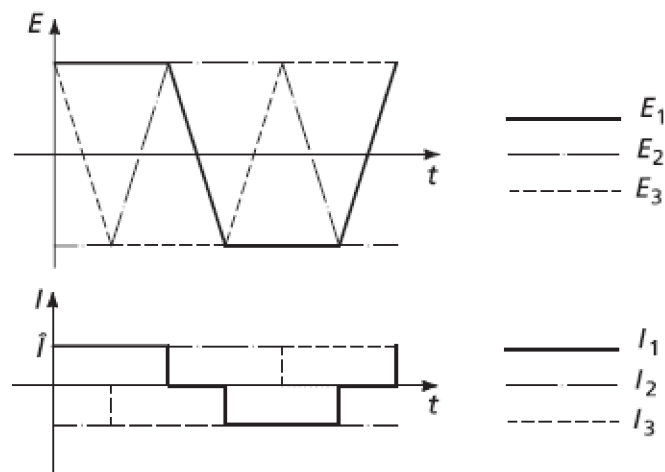


Figure 2.5: BLDC emf and current profile per phase

Voltage supply and voltage control signals are sent to the motor through an electric speed controller (ESC), a driver that should be positioned as closed as possible to the motor. The ESC functionalities will be later discussed in section 2.4.1.

BLDC motors characteristics are defined by its own datasheet, provided by the manufacturer. The main characteristics listed, between others, are:

- **Nominal Voltage [V]:** the maximum voltage that could be applied between two

phases connected to the electrical commutator. All the other parameters in the specifications are calculated at this voltage point.

- **Maximum Efficiency [%]:** it describes the maximum ratio between absorbed electrical power and the generated mechanical one;
- **No-load speed [RPM]:** it is the velocity of the motor in the case of no-load conditions, it is measured at steady-state and ambient temperature ( $\simeq 22^\circ$ );
- **No-load current [A]:** it is defined by the current consumption of the motor in no-load conditions at steady-state and ambient temperature, its value depends on speed and temperature;
- **Stall torque [Nm]:** it is the torque generated by the motor when the rotor is locked, zero speed, and the voltage supplied is the nominal one, this value is temperature dependent.

The other main parameters that define the working point of a motor are: speed, torque, voltage applied and current absorbed. These parameters are linked to each other by torque constant  $k_T$ , current constant  $k_I$  and speed constant  $k_V$ . These constants are defined by the manufacturer in the motor datasheet and are specific of each motor. They refer to what is called the mono-phase equivalent model that could be applied to study a three-phase motor [18]. This mathematical description can be used for three phase BLDC motors under the hypotheses that:

1. the commutation of phases is perfect;
2. the current waveforms are exactly the ones shown in Figure 2.5;
3. the motor is supplied from an ideal direct voltage source.

Monophase mathematical model defines the motor torque as:

$$Q = k_T(I - I_0) \quad (2.4)$$

Where:

- $I_0$  [A] is the no-load current defined by the motor datasheet;
- $I$  [A] is the current absorbed by the motor armature;
- $Q$  [Nm] is the mechanical torque generated;
- $k_T$  [Nm/A] is called the motor torque constant.

No-load current is taken into account if the  $Q_m$  is considered to be the torque inside the motor, not considering the losses due to friction; that said, often  $k_T$  is calculated using the motor torque with friction moments subtracted and in doing so the value already takes into account mechanical losses, so the formula is reduced by neglecting  $I_0$ . Similarly, the output speed of the motor shaft can be defined as:

$$\omega = k_V(U - RI) \quad (2.5)$$

Where:

- $\omega$  [rpm] is the rotational speed of the motor shaft;
- $I$  [A] is the current absorbed by the motor armature;
- $U$  [V] is voltage applied to the motor equivalent phase;
- $k_V$  [rpm/V] is the motor speed constant.

It is important to underline that commonly, on the datasheet, it could be found other two constants that are the reciprocal of the ones here described.

$$k_I = 1/k_T \quad (2.6)$$

$$k_E = 1/k_v \quad (2.7)$$

where  $k_I$  is called current constant and  $k_E$  is known as the back-EMF constant of the motor. From these equations it can be defined that motor torque  $Q$  and speed  $\omega$  are related in an ideal BLDC motor as shown in Figure 2.7. The larger line defines the ideal characteristic when the voltage of the supply is equal to the nominal voltage, while dashed lines represent a supply voltage lower than the nominal value.

The motor chosen for testing the Martian propeller is classified as a *servomotor* and therefore differs slightly from a normal brushless motor. A servomotor differentiates itself from a conventional engine by its high adaptive capability; as a matter of fact servomotors are better suited for applications that require a steep variations of speed and torque. Usually, servomotors have low inertia and high linearity current/torque ratio. This type of motors is largely used in numeric control or robotics. Servomotor's rotors usually are made by permanent neodymium (NdFeB) magnets.

The manufacturer of this motor has perfected a type of winding stator coils, patented as FAULHABER system, that can compromise the downsizing of the motors and high performances: in this system the motor becomes coreless, meaning that the coils are not anymore wound around an iron stator, but instead wound up as a thin cylindrical layer around the rotor. This configuration has several perks such as: low torque ripple, no cogging torque and a complex higher efficiency and smoother speed control than other BLDC motors.

Brushless motors also have position sensors, called Hall sensors, that enable to know the rotor position and to evaluate the output speed of the motor. Hall sensors are transducers that react to the motor magnetic field by sending a voltage signal output that will be processed by the ESC. In this particular motor there are 3 Hall sensors.

Attached to the motor rear end, it can be found an encoder produced by the same manufacturer as the motor. The encoder is a 3 channel incremental encoder, where 2 channel outputs are shifted by 90 degree, in order to determine the direction of the spinning motion, and the last is an absolute position channel. This encoder has a resolution of 1024 lines per revolution. A brushless motor was not only chosen for its reduced size, but also because it is preferable in aerospace applications: avoiding brushes prevents any sparking that could lead to fire or electrical problems, moreover this kind of devices are more time enduring.

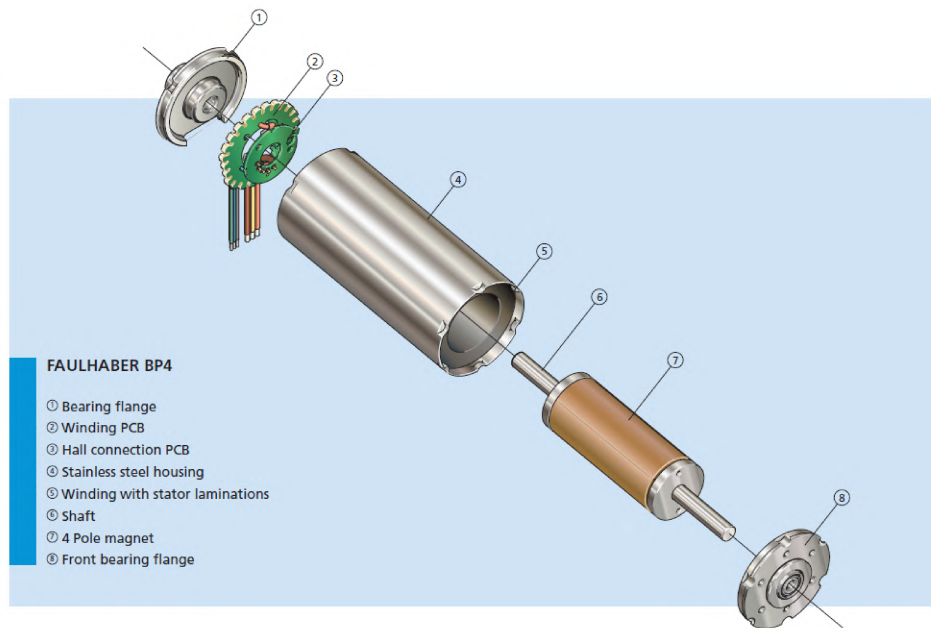


Figure 2.6: Internal Structure of 2264W 4 poles BLDC. ©Faulhaber

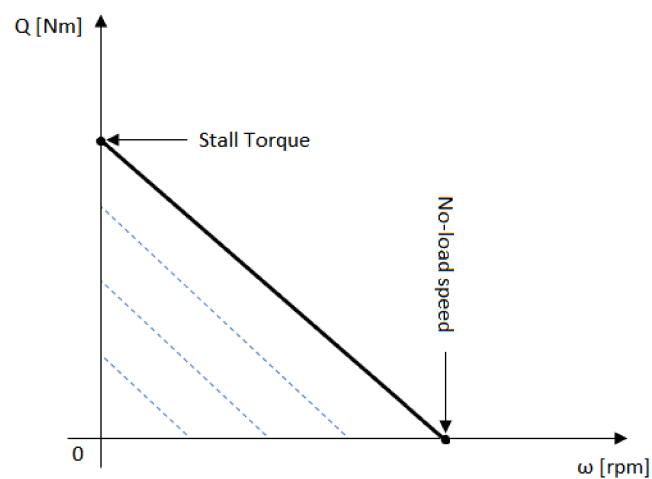


Figure 2.7: Ideal Torque/Speed relation of BLDC motor

### 2.2.3 ESC Driver

Brushless motors are electrically driven by an external ESC driver. ESC controllers house the control electronics of the motor and of its sensors. The ESC, that the manufacturer advises using with the chosen motor, is the SC5008S, depicted in Figure 2.8. Its main duty is controlling the output speed of the motor, by chopping and modulating phase voltages. This can be done through different methods. The type of control signals that could be forward to this ESC are the following:

- an **analog voltage signal** between 0 and 10 V, where 10 V corresponds to the maximum speed reachable with a determined motor supply and if the signal is greater than 10 V the control is saturated;
- **PWM signal** in TTL logic<sup>1</sup>, where the duty-cycle can range from 0 to 100%, meaning maximum speed for the specified supply;
- **No function**, meaning that the velocity of the motor will be fixed to the maximum value for the supplied voltage;

All these methods could be applied by using a control loop on the speed, that uses Hall sensors feedback, or they could be just directly forwarded by the ESC, skipping the speed control regulation.



Figure 2.8: Faulhaber ESC SC5008

<sup>1</sup>TTL logic is cor a technology used for Integrated circuits where the logic 1 corresponds to a 5V signal.

The ESC driver used in this application has 16 ports on both sides, defined as:

Position	Name	Function
Left side	<i>IO1</i>	Encoder or brake
	<i>IO2</i>	Encoder or enable
	<i>FG</i>	Digital output
	<i>DIR</i>	Direction of rotation of the motor
	<i>U<sub>nsoll</sub></i>	Control voltage for speed
	<i>GND</i>	Motor reference signal
	<i>U<sub>mot</sub></i>	Motor power supply
	<i>U<sub>p</sub></i>	ESC electronics power supply
Right side	<i>MotC</i>	Phase C voltage
	<i>MotB</i>	Phase B voltage
	<i>MotA</i>	Phase A voltage
	<i>SGND</i>	Motor reference signal
	<i>V<sub>cc</sub></i>	+5V motor power
	<i>SensC</i>	Hall sensor C output
	<i>SensB</i>	Hall sensor B output
	<i>SensA</i>	Hall sensor A output

Table 2.3: Pinout for SC5008S driver

Faulhaber ESC is configurable through a software interface that will be further discussed and analysed in section 2.4.1

## 2.2.4 Accelerometers

Vibration analysis is one of the preliminary tests that has to be done in order to define if the built setup is sturdy enough to proceed in doing performance evaluation. To verify the robustness of the structure, vibrations should be acquired during tests and in standstill conditions, therefore two accelerometers were installed on the base plane of the swing. Each accelerometer was used to collect data in one direction: one is the direction perpendicular to the motion axis of the swing and the second one is on the motion axis itself. Ideally, for having reliable and precise vibration measurements the two axes of the accelerometers have to be completely decoupled and the sensors should be placed as close as possible to the centre of mass of the object in case.

Accelerometers here used are provided by NXP, have only one measuring axis that can analyse accelerations between -10g and +10g, with a nominal sensitivity rated at 200mV/g.

## 2.2.5 Joint Coupling

All the setup, shown in Figure 1.11, is kept together by a small coupling placed in a strategic position. Even if the coupling's work is purely mechanical, it performs a central duty: it connects the motor shaft with the torque meter shaft, making it possible for the propeller to turn at the same speed the motor is rotating. The main problem that could affect the coupling is misalignment, both axial and angular of the two shafts. Couplings should, therefore, be chosen with precision, knowing the misalignments that are allowed by

the specific mechanical assembly used. If alignment constraints are not respected, it can cause severe vibrations and erroneous torque transmission.

The one that was used in previous setups is a jaw coupling made of three separate pieces: two made of aluminium for the housing of shafts and a polyurethane insert, so called *spider*, that connects the two. This particular one presented two different diameters in order to couple itself specifically with the motor and the torque meter used. It has to be said that jaw couplings are able to accommodate large misalignments and high torques, on the contrary they are not best suited for high accuracy measurements. The coupling chosen for this setup is produced by Ruland Manufacturing. It had two screws on the side of the aluminium part to grasp the shaft, both M3 dimensioned, while the connection with the spider was done only by friction between the components.



Figure 2.9: Jaw coupling elements

The coupling was, in this setup, paired with a 3D printed cage. This ABS piece helped reduce the weight of the suspended motor on the torque meter shaft, by fastening it on the torque meter side panel. Moreover, the cage was supposed to be parallel to the coupling in order to stiffen the connection between motor and torque meter. It has to be said the ABS polymer, while it is easy to use in rapid prototyping and reduces production costs, has a low elastic coefficient, and therefore its stiffness could be not high enough to be suitable in high accuracy measurements.

### 2.2.6 Torque Meter

The torque meter chosen, to acquire torque data for this project, is HBM T21WN with nominal rated torque of 0.1 Nm. The limit of the measuring capability was chosen to be that low, because the tests of Maryland University, selected as a comparison, stated that the torque value for this specific propeller did not exceed 0.1 Nm, when kept under 5000 rpm. The torque meter was mounted between the motor and the propeller hub with suited joints to couple the rotational axis of motor, torsionmeter and propeller. This torque meter has additional functionalities such as an incremental encoder, the possibility to check the calibration of the instrument and multiple channels for reading the torque, either as voltage or frequency signal. In this campaign the torque was analysed through the voltage output, stating that:

$$Q = kV \quad (2.8)$$

where:

- $Q$  [Nm] is the torque read by the torque meter, applied to the shaft;



Figure 2.10: T21WN torque meter. ©HBM

- $k=0.01$  Nm/V is a constant;
- $V$  [V] is the voltage output of the sensor.

Constant  $k$  is not given by torque meter datasheet, but it was obtained knowing that at the maximum rated torque  $|Q_{max}| = 0.1$  Nm corresponds an output voltage of the sensor of  $V = \pm 10V$ . The accuracy of the torque measurement is defined by ANSI standard. The torque meter is certified to have an accuracy class 0.2, meaning that the absolute error on the measurement is  $\pm 0.2\%$ .

The torque meter is built with two different shafts: one, whose diameter is larger than the other, driven by the motor and a smaller one used to measure the torque generated by the object attached to it.

Torque meter can be defined on the basis of which type of torque they can measure: static or dynamic. Dynamic torques represent a complex measurement and therefore torque meter built for this purpose have to rely on complex sensor structures including electronics and pneumatic circuits. On the contrary, when torque is static or the dynamic is slow enough to be considered so, torque meters have to deal with simpler architectures. static sensors depends on the same principle that makes it possible to measure forces through load cells: deformation. The torque meter chosen for this study is of the second type.

On the measuring shaft of the torque meter, strain gauges are attached in a way that the torsion of the shaft will deform them, and the shear deformation will be transmitted as a voltage signal. The most common strain gauges configuration is a Wheatstone bridge, as described in section 2.2.1. This particular HBM sensors is equipped with a contactless measuring system, meaning that the output of the strain gauges circuit is not collected mechanically through slip-rings, but with an inductance system. This system enables to get rid of bearing and contact point with the rotating shaft that may cause mechanical damage over time. The manufacturer assure that this sensor needs semi zero maintenance, and the only parts that require it are the optical sensor, such as the encoder.

As described in the book "Measuring Torque Correctly" [2], edited by HBM itself, the Wheatstone bridge is powered by the voltage signal coming from a rotor winding on the shaft. This winding is powered by induction thanks to a antenna on the stator side that is excited with an AC voltage supply. Since the voltage given to the torque meter is DC, the stator electronics include a transformer to allow to power the inductance circuit.

The output of the strain gauges circuit is passed through a Voltage-Frequency Converter (VFC), which helps the deformation signal to be transmitted via an induction circuit similar to the one supplying voltage to the Wheatstone bridge. The output frequency signal is then amplified and filtered on the stator side. The scheme represented in Figure 2.11 depicts the output only as frequency, but it can be supposed that in order to read a voltage output as in the T21WN, the frequency is passed in a Frequency to Voltage Converter (FVC).

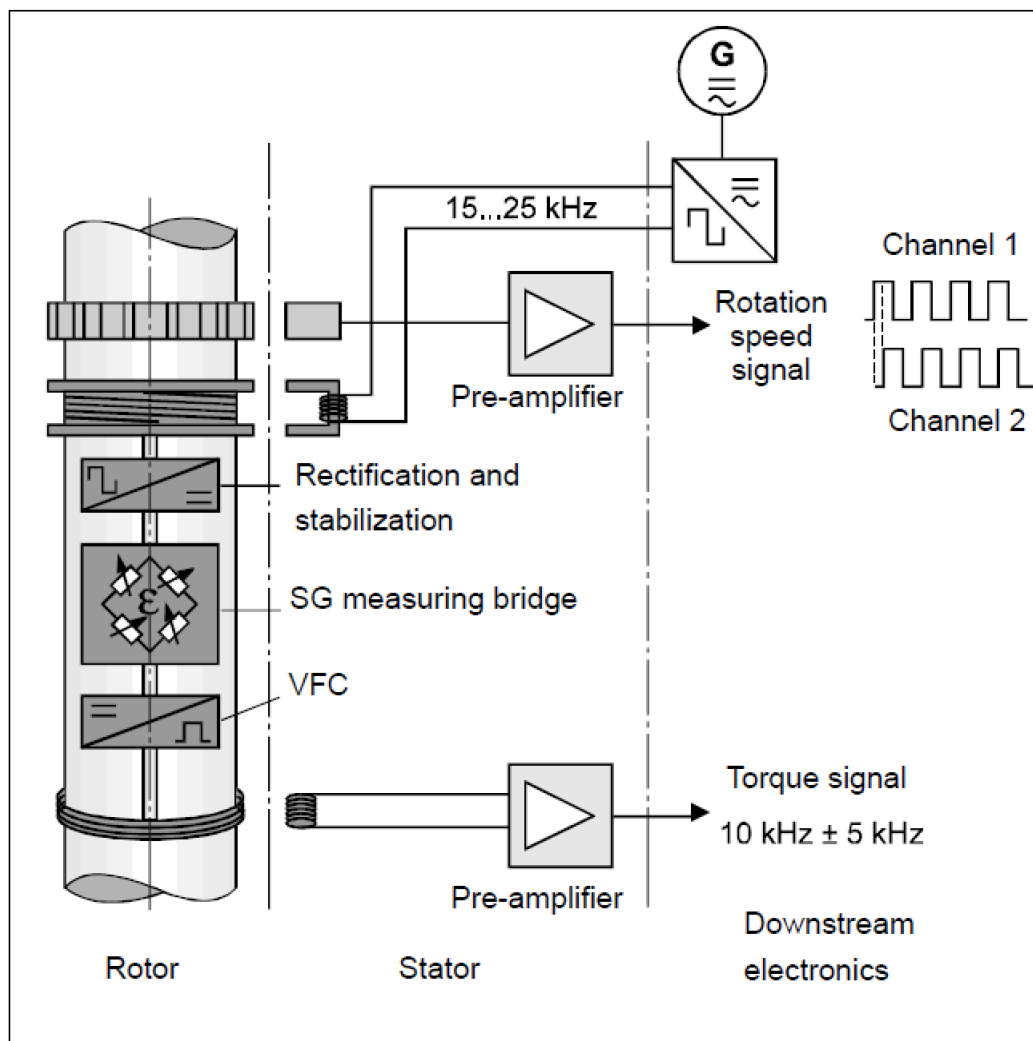


Figure 2.11: Torque meter contactless transmission principle [2]

Since torque meters are highly sensitive and fragile instruments, some precautions have to be taken into account when working with them. Structural limits are advised both for mounting it and for operating in safe conditions. Limits are imposed on the axial and radial forces, as well as on the flexural moment applied to the shafts.

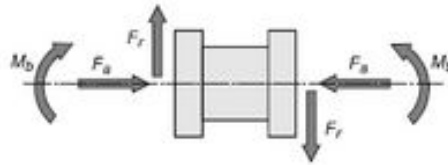


Figure 2.12: Schematic of structural loads on torque meter. ©HBM

For the torque meter used in this application the limit values that need to be respected are:

- Axial Force:  $F_a \leq 2$  kN;
- Radial Force:  $F_r \leq 3.6$  N;
- Bending Moment:  $M_f \leq 0.12$  Nm.

These limits do not have to be evaluated as absolute criteria, but as suggested boundaries for safety and damage prevention by the manufacturer. It is said that the limit values could be lower than the ones previously stated, if in presence of vibrations due to multiple axes solicitation. The rule of thumbs affirms that if the load is built up from 30% of the axial force and 30% of the radial force, then the maximum limit for the bending moment is only 40% of the value  $M_f$ . The same goes for the other combinations of loads<sup>2</sup>. As previously said, this torque meter has as an additional functionality an incremental encoder. The encoder has two channels and a resolution of 360 lines per revolution. Its output signals are squared waves, whose phase is shifted by 90°. These signals are TTL logic signals. The speed is read by an optical encoder that reads the rotation rate of the shaft with respect to an optical disk positioned on the shaft.

The torque meter is equipped, on its top part, with a permanent connector, whose different pins help collecting data outputs (torque, speed) as well as providing voltage references and supply.

### 2.2.7 Propeller & Hub

As already said, first performance tests aimed to reproduce the test developed by the University of Maryland, which gave the input for developing JPL's Mars Helicopter Scout. It was decided to try and recreate a propeller equal to the one used in the previously mentioned study [8] and test it in a similar environment to prove the capability of testing in Martian atmosphere.

The propeller was accurately made following the dimension given in the above mentioned paper and custom made in carbon fiber. Two identical blades were manufactured and a custom hub was 3D printed in ABS to house the blades. Blades are kept at a 32° pitch angle by the hub structure. This particular angle was chosen because, in the University of Maryland research, it was the one maximizing propeller performances. Blades are fastened to the hub with precision in order that, when spinning, centrifugal force does not damage the carbon fiber structure.

<sup>2</sup>[www.hbm.com/en/0779/tips-and-tricks-terms-and-expressions-for-specifying-torque-transducers/](http://www.hbm.com/en/0779/tips-and-tricks-terms-and-expressions-for-specifying-torque-transducers/)

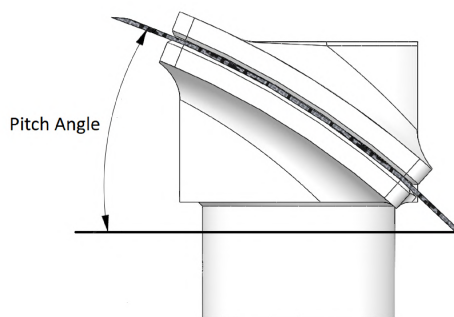


Figure 2.13: Propeller pitch angle

The connection between the torque meter and the propeller hub was made by several separate pieces:

1. a keyless bush, screwed to the torque meter measuring arm;
2. a funnel-shaped shaft;
3. a nut and a lock-nut, keeping the hub in place.

It can be seen from Figure 1.11, that the hub on the propeller side is fastened by a hexagonal nut and its lock-nut, while on the other side the hub is supported itself on top of the funnel shaft. The larger diameter of the funnel shaft it is emptied to fit over the external part of the bush. This design was apparently chosen because the shaft of the torque meter was not long enough to fit the hub designed. Furthermore, it is of leading importance the functioning principle of the keyless bush for securing the blade. A keyless bush is a specific type of bearing composed by a part that can be locked by screwing it on itself and a mobile part working as a reverse clamp. This second part opens up when the rear of the bearing is fully screwed, this principle enables to lock objects around the clamp by reducing the mechanical backlash between the two surfaces. These type of bearings are best suited for hydraulic and pneumatic works. Chances are that this connection could lead to problems in the torque analysis since the bush is not fully appropriate for this type of accurate measurement, as it could get easily unscrewed by random vibrations. It has to be mentioned that the hub was designed to have two perpendicular grub screws, that could help lock the hub in place on the shaft. This type of locking was never used in the previous setup since it was feared that the pressure of the grub screws could lead to propeller unbalance.

## 2.3 Preventive Vacuum Testing

In order to define which was the faulty component in the vacuum setup, it was at first thought to lead a new testing campaign that would focus on aspects of the system that were not considered sooner. The two main tests done were a vibration test and a fixed setup test. Both of them were conducted in vacuum Mars-like conditions to reproduce the exact same situation in which the erroneous torque data were acquired.

### 2.3.1 Vibration Analysis

As previously stated, when approaching data acquisition with a new test bench, it is necessary to perform vibration tests. Unfortunately, this type of tests were never performed with the swing setup represented in Figure 1.10, even if some accelerometers were included in the acquisition system. Accelerometers output signals were in fact actively acquired by the Labview code, but, since the acquisition rate was uniquely defined for both for the acquisition of torque, thrust and vibrations, the rate chosen was not enough to sample vibrations in the right way. The acquisition rate used in these older test was 200 Hz, implying an under sampling of the acceleration outputs and therefore an aliasing of the read signal. It is, in fact, important to remember the Nyquist-Shannon sampling theorem that states:

$$f_s > 2f_{max}$$

meaning that the sampling frequency,  $f_s$ , used to acquire a signal, has to be at least two times larger than the maximum frequency contained in that signal. The usual rule of thumbs tells that a good accuracy on measurements is given by a sampling frequency ten times higher than  $f_{max}$ . This explains why 200 Hz was a good sampling rate for torque and thrust measurements, that have a real slow dynamic, while it was not enough for vibrations.

For a more accurate and honest analysis of the setup vibrations, it was chosen to use the same acquisition system developed in Labview with increased sampling rate to 1000Hz. In order to give a graphical representation of vibrations, data were collected and elaborated with a fft (Fast Fourier Transform) algorithm in MATLAB. Fast Fourier Transforms algorithms allow to convert time domain signal, as the the one acquired in test runs, into frequency domain. Ffts are computed for signal acquired with quasi-fixed speed; they are then collected in a waterfall plot where the  $x$  axis represents the frequency domain, while the  $y$  axis is the rotating machine speed. By using this procedure, it is trivial to detect the frequencies at which vibrations occur. Such relationship between the rotating shaft speed and the excitation frequencies becomes evident only if the speed is defined in Hz, knowing that 1 Hz is equal to 60 rpm. On waterfall plots two types of lines can show up: diagonal lines and straight lines parallel to speed axis  $y$ . The first ones are defined by the ratio between vibration frequency and the speed a which the peak occurs and the number associated with them are called orders, instead the second ones define critical speeds of the system or outside acquired noise. Orders  $n$  can be mathematically defined by:

$$\omega = n \cdot \lambda \tag{2.9}$$

Where:

- $\omega$  [Hz] is the rotational speed of the machine;
- $\lambda$  [Hz] is the vibrational frequency.

Vibrations are defined as more or less important by their amplitude displayed on the waterfall  $z$  axis. Separate waterfall plots were done for flexural vibrations and axial vibrations: the first ones are vibrations occurring in the plane perpendicular the propeller thrust while the second ones are parallel to the motion of the swinging setup. In this particular case, the two plots show some similar peaks, which means that the positioning

of accelerometers was poor and the two vibration axis were not completely uncoupled.

In the axial plot, represented in Figure 2.14, it can be seen that the two main orders present are the 3<sup>rd</sup> one and the 1<sup>st</sup> one. The type of harmonics, indicated by the cascade plot, can define which problem affects the rotating machine analysed. This method, called *Failure mode analysis*, does not to give a definitive response for the failure, but its an approach that fused with general knowledge of the working principle of the system could get started and send hints on which the problem can be [19]. In the case of axial vibrations, harmonics from 1<sup>st</sup> to 4<sup>th</sup> could be due to shaft bending or misalignment. Instead in the radial direction, the dominant harmonic is the 1st one, that most certainly means that there is a dynamic unbalance in the rotating structure. It has to be said that, in the first phase of the manufacturing of propeller, balance tests were performed on the blades. These tests were made only in static condition, since the propeller could be damaged if working in standard air and in vacuum it is difficult to perform dynamic balancing.

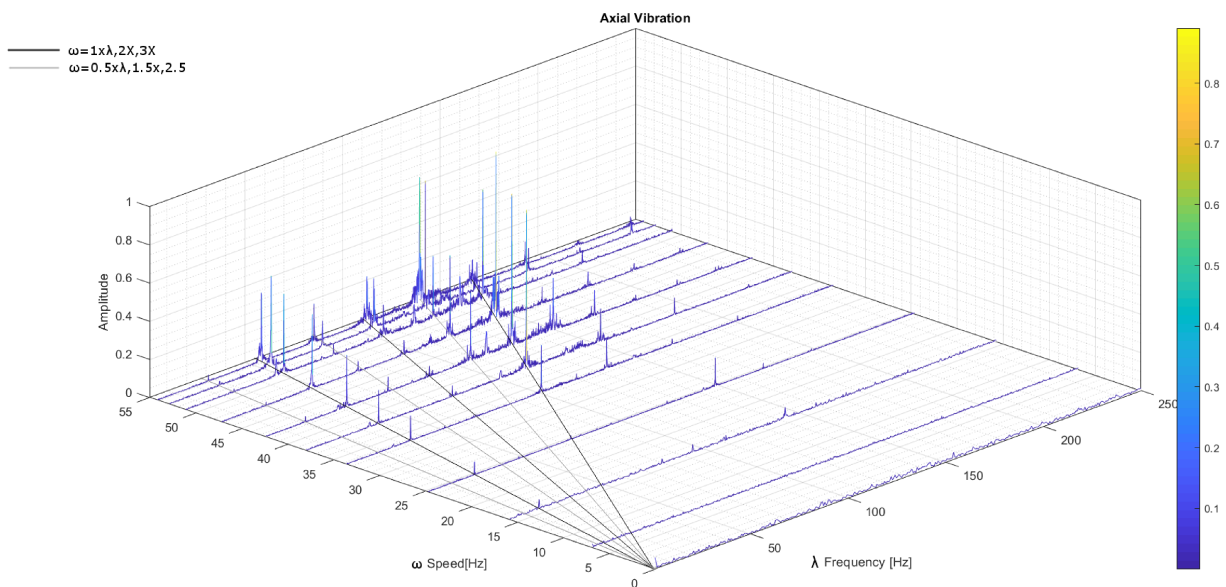


Figure 2.14: Axial Vibrations cascade plot at varying speed  $\omega$

Most of the largest axial and flexural vibrations are thought to be due to the swinging motion of the setup. The setup is not swinging in a precise direction and it is subject to external stresses when the speed of the propeller is instantaneously changed. Moreover, the cables supporting the suspended design from the top plate of the columns were visibly vibrating during tests, transmitting excitation to the whole setup.

The same fft analysis was done also on torque and thrust data collected from tests. In this case, the amplitude of the harmonics was significantly less important with respect to the motion vibrations. In contrast with what was hypothesised, most vibrations happened in the thrust measurement, where there is a considerable 1<sup>st</sup> harmonic and a critical speed at 150 Hz. Torque vibrations were smaller than the ones associated with thrust, but they showed a considerably high amplitude for high orders such as x8 and x12 as well as a critical speed at 450 Hz. Unluckily, these tests did not give an absolute result on which

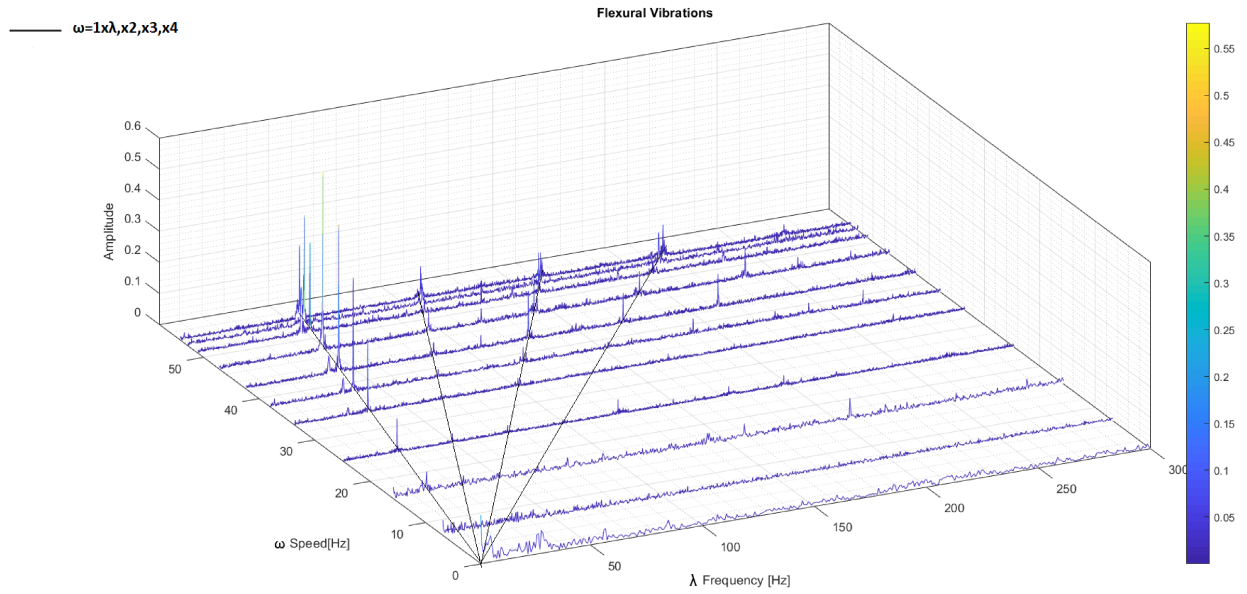


Figure 2.15: Flexural Vibrations cascade plot at varying speed  $\omega$

was the cause of the faulty torque measurements, but brought forward the suspect that the error was due to a misalignment in the measurement chain.

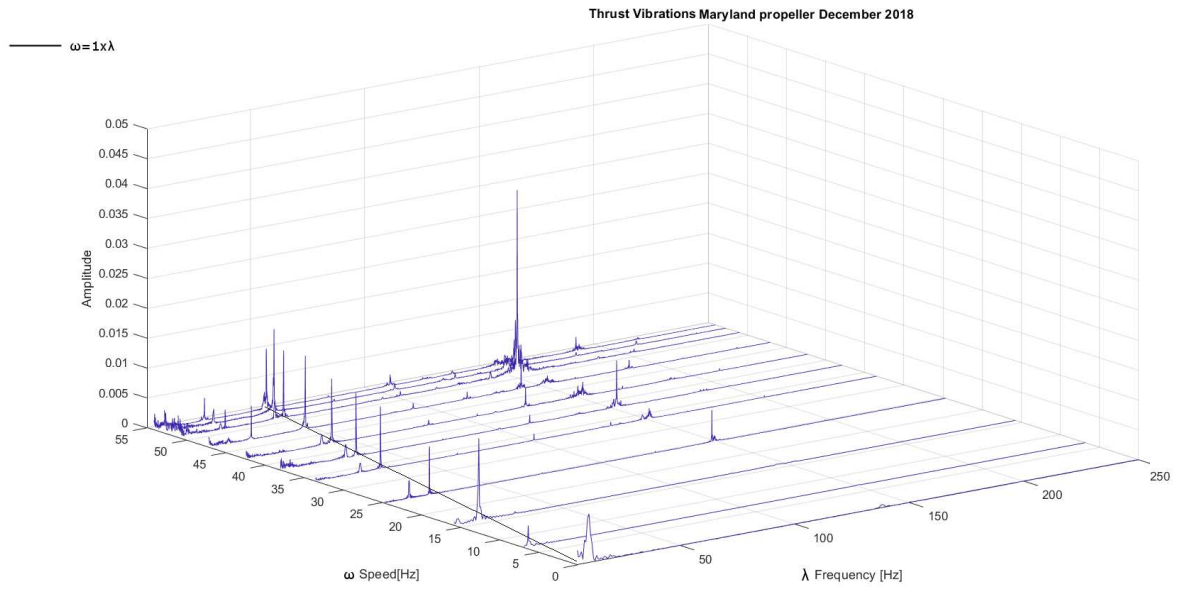


Figure 2.16: Thrust cascade plot at varying speed  $\omega$

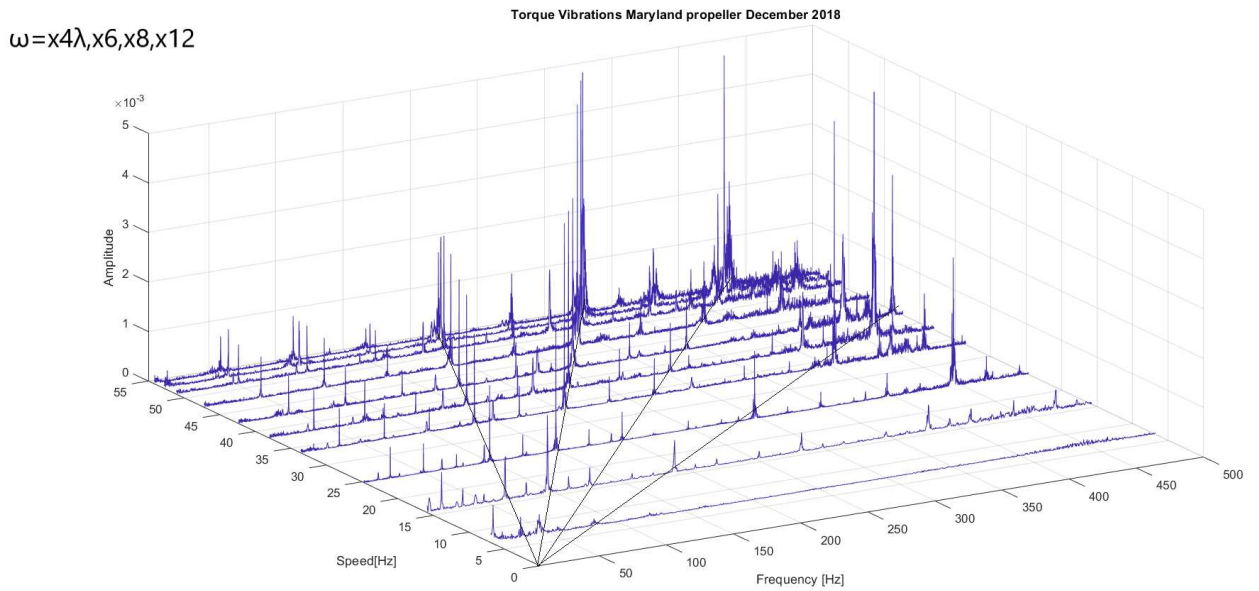


Figure 2.17: Torque cascade plot at varying speed  $\omega$

### 2.3.2 Fixed Setup Testing

One of suspects of the incorrect torque acquired was the setup architecture itself. The swing setup was a comprise between Maryland's University architecture and what was possible to insert in TAS-I PHASE chamber. The setup had to have at least one degree of freedom in order for the thrust to be acquired by an S-beam load cell. In the beginning, it was thought to build a fixed setup, but it was advised not to, because, lacking a vibrational study of the setup, it was thought to be unsafe. In fact, the energy generated by the propeller could be stored in the chamber body, leading to structural damages if it should be excessive. In any case, when confronted with the possibility that the swing setup could not be appropriate for acquiring the torque, the only choice left was a fixed architecture.

One test was performed in vacuum conditions and only torque and speed were acquired. The fixed setup had to be high enough to allow the blade to rotate freely inside the chamber and to do not interfere with the plate and the supporting rails. The configuration was achieved by using modular supports, fastened with the 3D printed torque meter base, as seen in Figure 2.19. On the setup the custom made blade was mounted as described in section 2.2.7.

This test resulted in the torque trend getting furtherer from the one found by Maryland's University, meaning that the swinging motion of the setup actually interfered with the torque measurement. This trend could be observed in Figure 2.18. The torque increased by 6% with the new test setup with respect to the one found with the swing test bench. Unfortunately, the distribution of the standard deviation error of the torque was not reduced. In particular, the torque produced by a propeller should be proportional to the square of the speed. This was proven to be wrong when analysing both previous tests' torques and the one acquired with a fixed setup.

This setup, which was though to radically change the torque measurements and previous errors, turned out to do not work as well as expected. In particular, none of these vacuum tests gave a clear indication if the cause of the wrong torque was due to the motor or the torque meter. In order to proceed in the analysis, vacuum tests were stopped and a characterization of the components was started.

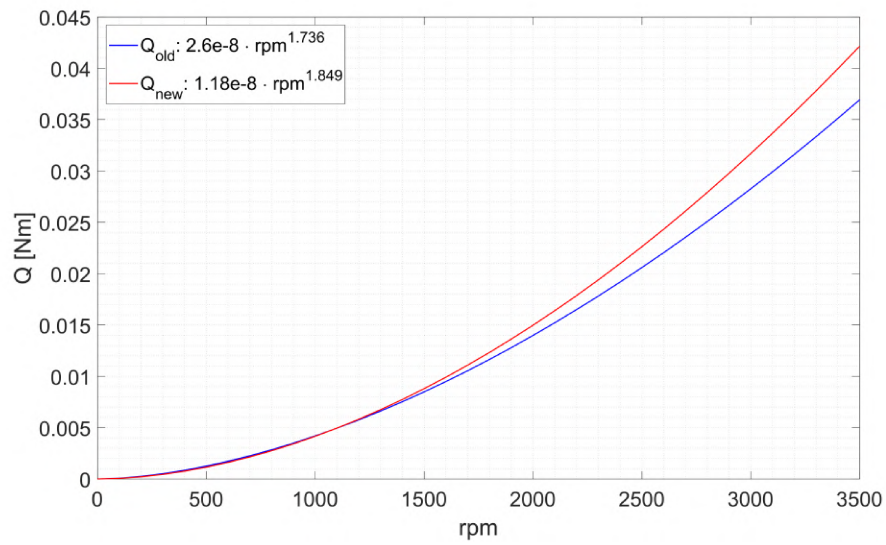


Figure 2.18: Comparison between torque data trends in old setup (swing) and the new setup (fixed)

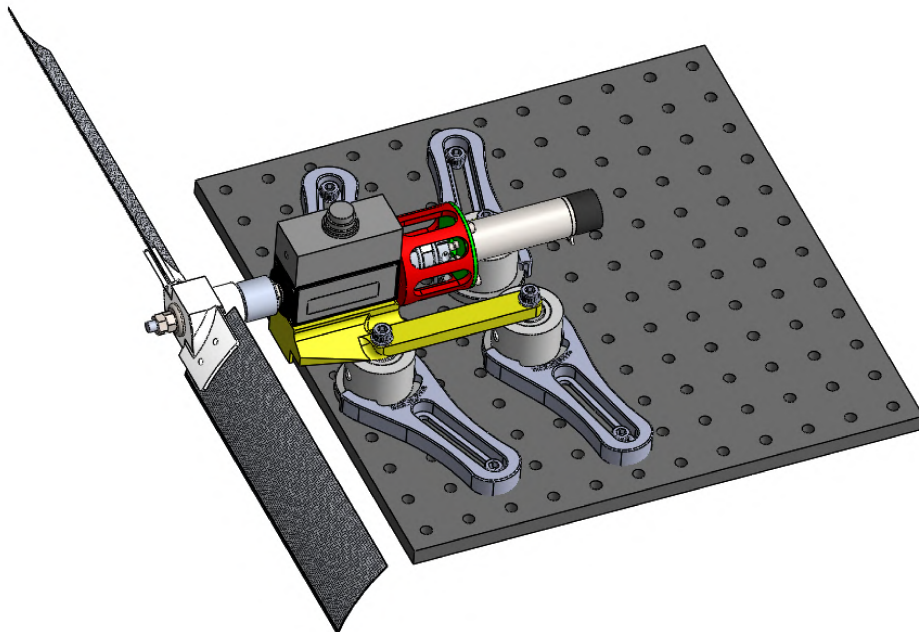


Figure 2.19: 3D model of the fixed setup used for vacuum testing

## 2.4 Motor Characterization

After trying unsuccessfully to individuate the cause that led the torque to be higher than the one measured by the study of the University of Maryland in the vacuum environment, it was thought best to test individually the components in air to understand whether they had suffered any damage during their stay in low pressure.

The first components to be tested were the motor and its ESC, following by a detailed analysis of the torque meter performances. To characterize the motor and attest that it was working properly an experimental characterization had to be done. The constants  $k_V, k_I$  and  $k_T$ , given in the motor datasheet, were checked through physical tests. This was done both to ensure the motor datasheet was correct and to be able to define the torque in future tests in a mathematical way, using the monophasic equivalent model.

### 2.4.1 Controller Software

To control the motor in this first phase of the testing it was useful to try and understand the software *Motion Manager*, developed by the manufacturer of the motor. The software is able to connect to the physical ESC and send commands to control it. The interface that makes this connection possible is a USB B port available on the adapter for USB interface, shown in Figure 2.20, that is connected to the left part of the ESC. In order to successfully connect the ESC to the PC software, the electronic voltage  $U_p$  has to be supplied to the ESC, since the USB does not feed enough power to turn on the ESC circuits.

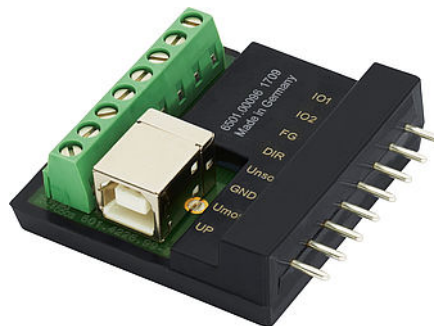


Figure 2.20: USB connector

When first connected to the software the user has to define the type of motor in use, the moment of inertia applied to the shaft and the minimum and maximum speed possible; all the other parameters are already defined on the base of what is written in the datasheet.

When it comes to the choice of the type of control to apply, there is a first decision that has to be taken: it is possible to do either a speed control or voltage control. The speed control, described in red square Figure 2.21, is implemented as a PI control that elaborated the difference between the speed value  $n_{soll}$  given by the software and the value read from Hall sensors, in order to reach the given input value.

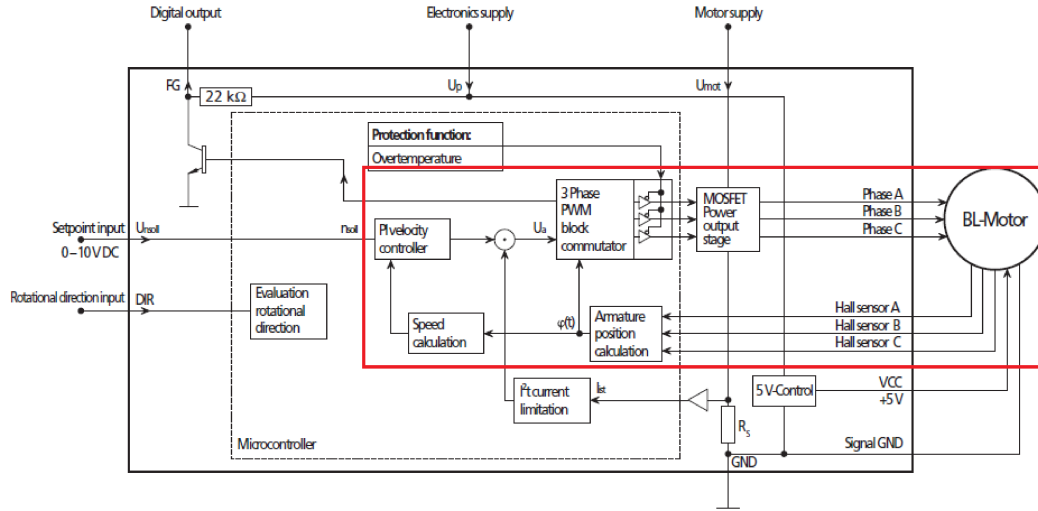


Figure 2.21: Block diagram of the controller

While working in speed control mode the manufacturer defines that the shaft speed as:

$$n_{soll} = n_{max} \left( \frac{U_{nsoll}}{10V} \right) \quad (2.10)$$

Where:

- $n_{soll}$  [rpm] is the rotational speed of the motor shaft;
- $n_{max}$  [rpm] is the maximum speed defined through the PC interface, for the datasheet is can be 21100 rpm to its maximum;
- $U_{nsoll}$  [V] is the voltage applied to the homonym input, it can range from 0 to 10 V maximum.

It is easily remarkable that the main function of  $U_{nsoll}$  is to reduce the output speed, multiplying the maximum defined value by a fraction of the 10V input. This control method is useful when it is requested a sweep of the speed, like a ramp, but for understanding the correctness of the motor parameters it can be misleading.

The other control method possible is the voltage control. It was verified that in this case the speed control loop was bypassed and the behaviour of the motor was defined by the following equation:

$$U = U_{mot} \left( \frac{U_{nsoll}}{10V} \right) \quad (2.11)$$

Where:

- $U$  [V] is the voltage applied to the equivalent monophase model of the motor;
- $U_{mot}$  [V] is the voltage applied for supplying of the motor.

Moreover, it was proven that when  $U_{nsoll} \geq 10$  V, the voltage  $U$  was saturated to its maximum value possible with  $U_{mot}$ . This particular characteristic was really important for the tests ahead, since it gives the power to say that if  $U_{nsoll}$  is saturated, then  $U = U_{mot}$ . Combining the result from equation 2.11 and the equation 2.5, the speed of the shaft can be defined knowing the voltage  $U$ .

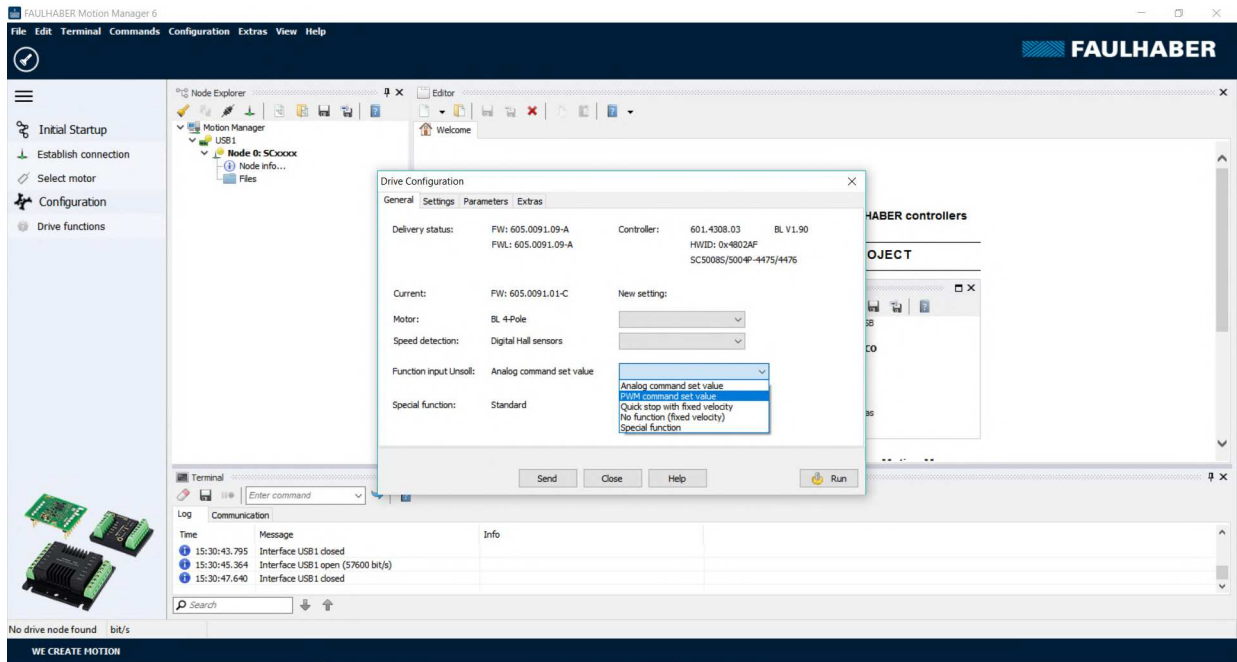


Figure 2.22: Input voltage functions for the ESC

After choosing one of the previously described control methods, the software gives a series of functions through which the input can be given to the controller. Once the user has defined the control type and its parameter, they are sent to the motor when the button Send is pressed, but the motor will run only after the Run button is pushed. When the USB is disconnected, the controller recalls the last control input used and will run with those parameters, until a new software connection happens and a new run is done.

## 2.4.2 Motor tests

Some tests were performed to evaluate experimentally the constants  $k_V$ ,  $k_T$  and  $k_I$  of the motor and compare them to the ones given by the datasheet. Unluckily for testing these parameters there is no standard given, hence the values handed by the manufacturer can suffer not only from normal statistic errors, but also from subtle differences in testing methods.

Tests were initially made on the motor with no load applied and later connecting the torque meter, following the former testing architecture. Voltage signals were delivered by two DC voltage supplies: a GwInstek GPS2303 for the  $U_{nsoll}$  and  $U_{mot}$  and an Eutron BVD450 for the ESC electronics  $U_p$  and the torque meter supply. Voltage and current data were collected with a Fluke 45 multimeter, either put in parallel, for voltage reads, or in series with the supply for the currents reads. The rotational speed of the motor was read through the Hall sensors of the motor, by plotting the output on a Tektronic TDS3012 oscilloscope, reading the frequency of the square wave, knowing that the relationship between the frequency  $f$ , expressed in Hz, and the speed  $\omega$ , in rpm, is the following:

$$\omega = f \cdot 30 \quad (2.12)$$

To achieve higher accuracy on speed values, for each test point three speed values were collected and later averaged. The control applied to  $U_{nsoll}$  used for all the following test is a voltage control, lead by an analog input.

### Kv testing

In order to find the speed constant  $k_V$ , by simplifying the Equation 2.5, the following formula was used:

$$k_V = \frac{\omega}{V} \quad (2.13)$$

supposing that the current losses are sufficiently small to be neglected. In this case,  $U_{mot}$  was chosen equal to 5V and  $U_{nsoll}$  was varied to vary the speed output.

Data collected are shown in the Table 2.4.

$U_{nsoll}$ [V]	$U_{mot}$ [V]	$U$ [V]	$\omega$ estimated [rpm]	$\omega$ [rpm]	$k_V$ [rpm/V]
0	0	0	0	0	0
0,9774	5,015	0,490166	396,5	418	852,77215
2,0586	5,015	1,032388	835,2	873,9	846,48416
3,0173	5,007	1,510762	1222,2	1285,7	851,02743
3,991	5,005	1,997496	1616,0	1693,5	847,81167
4,984	5,005	2,494492	2018,0	2130	853,88127
6,08	5,016	3,049728	2467,2	2597,7	851,78088
7,046	5,022	3,538501	2862,6	2991,3	845,35792
8,01	5,037	4,034637	3264,0	3477	861,78757
9,079	5,049	4,583987	3708,4	3918	854,71445
10,012	5,001	5,007001	4050,7	4039	806,67047

Table 2.4: Data acquired from varying tension tests

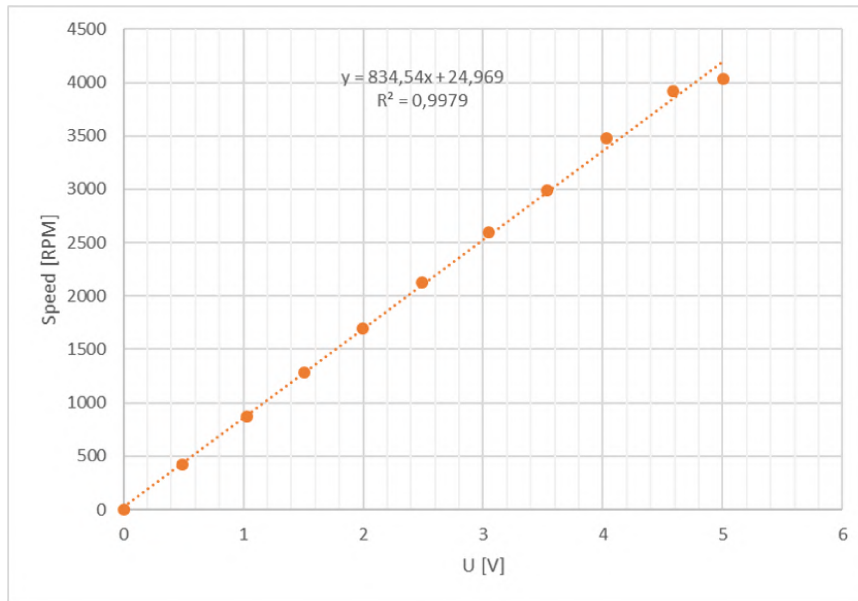
The  $\omega$  estimated column represents the speed expected if  $k_V$  was exactly equal to the datasheet value of 809 rpm/V with the found  $U$  value. From this test was found  $k_V=847.2\pm 15$  rpm/V, while the constant given by the datasheet is  $k_V=809$  rpm/V.

The same test was done a second time, by keeping  $U_{nsoll}$  constant saturated over 10 V, and varying  $U_{mot}$ . It is important to remember that in this case, from Equation 2.11,  $U = U_{mot}$ .

In order to evaluate the correctness of the data acquired, both tests results have been plotted in a speed-voltage plot (Fig. 2.23, Fig. 2.24). A linear regression has been added as defined between the  $U_{mot}$  and the speed  $\omega$  found by the control saturated testing. The value of  $R^2$ , called coefficient of determination, is defined mathematically by the ratio of the explained variance<sup>3</sup> to the total variance<sup>4</sup> of the model. This value identifies the quality of the regression superimposed to the data: the more  $R^2$  is close to 1, the better the approximation.

<sup>3</sup>Variance of the model's prediction.

<sup>4</sup>Sample variance on the dependent variable.

Figure 2.23: Data acquired at  $U_{nsoll}$  changing

$U_{mot}=U$ [V]	$\omega$ estimated [rpm]	$\omega$ [rpm]	$k_V$ [rpm/V]
1,0653	861,8	853,6	801,2766
1,9868	1607,3	1613,8	812,2609
3,085	2495,8	2491,8	807,7147
4,024	3255,4	3251	807,9026
5,018	4059,6	4098	816,66
6,015	4866,1	4855	807,1488
7,017	5676,7	5664	807,1826
7,982	6457,4	6466	810,0727
8,89	7192,0	7202	810,1237
10,019	8105,4	8056	804,0723

Table 2.5: Data acquired from  $U_{nsoll}$  saturated test

From this last test, performed changing  $U_{mot}$ , it was found an average value of  $k_V=808.4\pm 4$  rpm/V. It can be then underlined that when  $U_{nsoll}$  is saturated, the experimental  $k_V$  value is more similar to the one found in the datasheet than the first experiment's one. It was thought that there could be an underlying relationship between the percentage of command input given to the motor and the  $k_V$  value obtained. It was done a state of the art research about this topic but it was not found any important study about this issue. For further tests, it was thought better to continue controlling the motor with  $U_{mot}$  as the changing variable and  $U_{nsoll}$  saturated slightly over 10 V.

A last test was made measuring the current absorbed by the motor. The test was done repeating the last test voltage variable, with  $U_{nsoll}$  saturated and  $U = U_{mot}$ . In this case two different  $k_V$  values were calculated, one using the full formula described by Equation 2.5 and  $k_V$  simplified using the of the Equation 2.13.

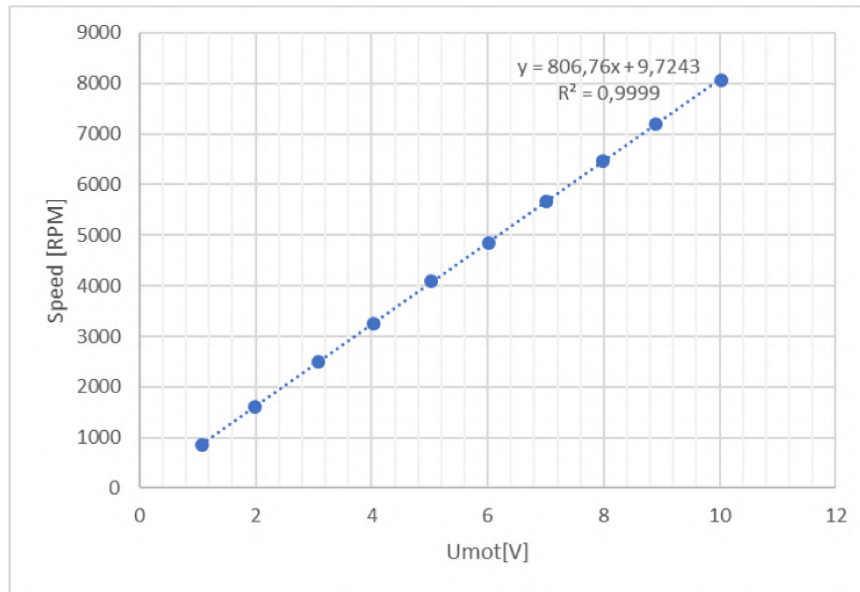


Figure 2.24: Data acquired when  $U_{mot}$  changing and  $U_{nsoll}$  is saturated

The mean value found are the following:

$$k_{V\text{simpl}} = 809.21 \pm 5.22 \text{ rpm/V}$$

$$k_V = 813.15 \pm 3.63 \text{ rpm/V}$$

It can be seen that the simplified version carries out a more accurate value with respect to the datasheet one, but also the value found through the complete version of the equation is close enough to the one given by the manufacturer. These tests lead to think that the value described in the motor datasheet was found with the control saturated, bypassing the speed control and neglecting the absorbed current component. After analysing the overall results it was thought that if future tests had to be done, the parameter  $k_V$  of the datasheet could be used to calculate the output torque with enough accuracy.

$U_{mot}$ [V]	$U_{nsolt}$ [V]	$\omega$ [rpm]	I[A]	$k_V$ simplified [rpm/V]	$k_v$ [rpm/V]
1,05	10,14	840,7	0,067	800,67	812,07
2,02	10,14	1616,5	0,079	800,25	807,19
3,02	10,14	2442,7	0,08	808,84	813,58
4,03	10,14	3246	0,085	805,46	809,21
5,04	10,14	4095	0,088	812,50	815,63
5,98	10,14	4870	0,092	814,38	817,15
6,99	10,14	5679	0,107	812,45	815,19
7,96	10,14	6484	0,113	814,57	817,12
9,02	10,14	7320	0,121	811,53	813,93
10	10,14	8043	0,131	804,30	806,62
12,01	10,14	9760,5	0,153	812,70	814,98
13,98	10,14	11364	0,175	812,88	815,12

Table 2.6: Data acquired from current tests

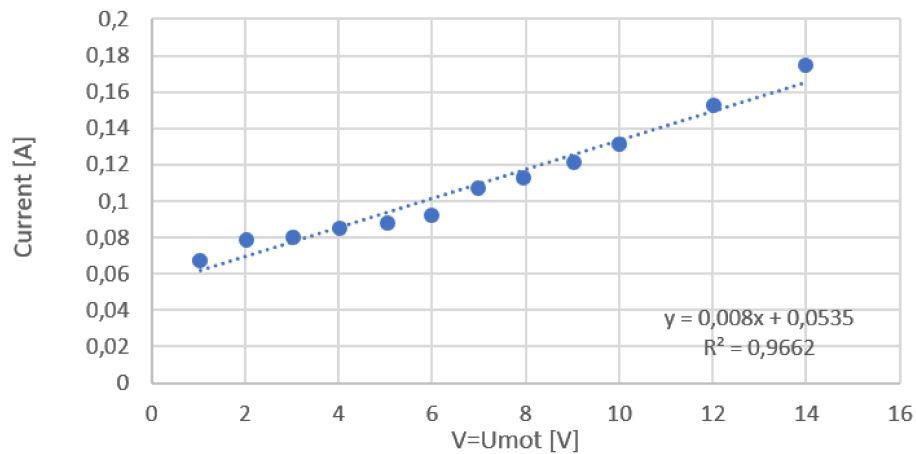


Figure 2.25: Torque-current relationship in no load conditions for Faulhaber 2264W 024 motor

### Kt testing

Finding and testing the torque constant  $k_T$  for the motor is not as easy as evaluating its speed constant. In this case, the motor had to be connected to the torque meter in its former position, with the jaw coupling. This was done to read the torque value from the torque meter output. In no-load conditions the torque meter output is close to 0, so, to identify a torque momentum, a mass was mounted on the torque meter measuring arm. This mass helped as well to keep the torque meter shaft blocked during the measurements.

The test was done by increasing the current given by the supply to the motor, with  $U_{nsoll}$  kept constant over 10 V, and reading the  $U_{mot}$  value as well as the speed. It is important to underline that previously to this test some precautions were taken: the torque sent to the torque meter never exceeded the nominal limit of the sensor, moreover reaction forces at the base of the torque meter shaft were calculated to be lower than the limits express in HBM's datasheet, and additionally the currents fed to the motor were kept under the 6 A limit prescribed by the manufacturer. The test was repeated three separates times.

I [A]	Q[V]	Q[mNm]	$k_T$ [mNm/A]	$k_I$ [A/mNm]
0	-0,035	-0,3501	-	-
0,502	0,555	5,55	11,06	0,0905
1	1,11	11,1	11,10	0,0901
1,533	1,76	17,6	11,48	0,0871
2,009	2,3	23,0	11,45	0,0873
2,05	2,24	22,4	10,93	0,0915
0	-0,055	-0,550	-	-
0,496	0,6	6,00	12,10	0,0827
0,998	1,16	11,6	11,62	0,0860
2	2,33	23,3	11,65	0,0858
2,995	3,52	35,2	11,75	0,0851
3,994	4,89	48,9	12,24	0,0817
0	0,068	0,680	-	-
0,498	0,627	6,27	12,59	0,0794
0,997	1,26	12,6	12,64	0,0791
2,034	2,295	23,0	11,28	0,0886
3,019	3,455	34,6	11,44	0,0874
4,015	4,45	44,5	11,08	0,0902
4,998	5,52	55,2	11,04	0,0905

Table 2.7: Data acquired with  $k_T$  testing

Here the torque constant has been determined as a simplified version of Equation 2.4

:

$$k_T = \frac{Q}{I} \quad (2.14)$$

- $Q$  [Nm] is the torque read through the torque meter;
- $I$  [A] is the current supplied to the motor.

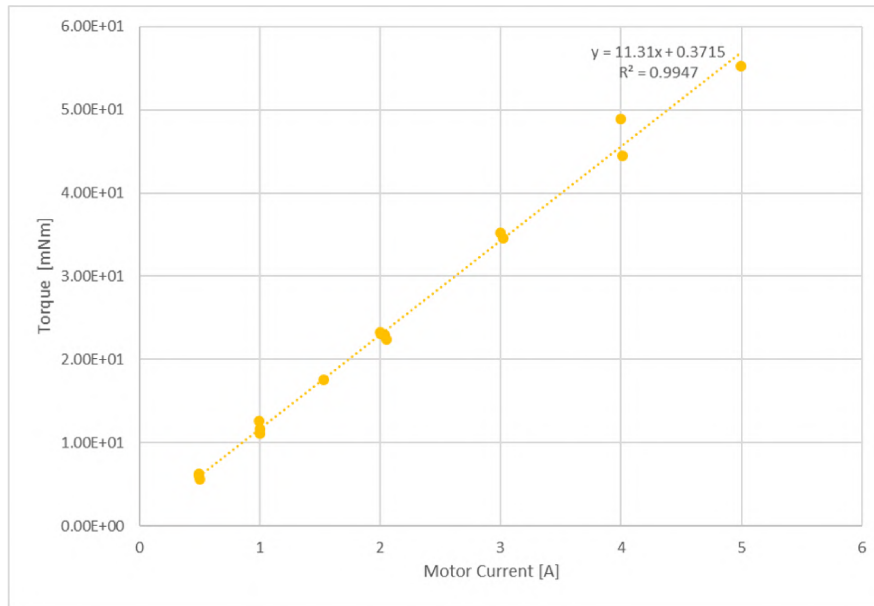


Figure 2.26: Torque-current relationship for Faulhaber 2264W 024 motor coupled with HBM T21WN torque meter

From this analysis resulted that  $k_T=11.59\pm0.56$  mNm/A and its reciprocal  $k_I=0.0864\pm0.0040$  A/Nm. The values presented for these two constants in the motor datasheet are respectively 11.8 mNm/A and 0.085 A/mNm. The provided datasheet data for these two parameters are extremely near to the one experimentally found, meaning that the datasheet constant could give a good approximation when used in mathematical calculations.

This  $k_T$  test had a double aim: first to check that the real constant value of the motor is similar to the one handed out by the manufacturer and second to check that the data read through the torque meter was reliable in open air. Both of these points were found to be true, meaning that the torque meter did not suffer damages when it was working in low pressure environment.

## 2.5 Updating Mechanical Connections

Dealing with wrong acquired torque data, the fault could either be electrical, as in the motor or in the data acquiring system of the torque meter, or it could be mechanical. In particular, during the tests campaign it was found out that the torque meter was not vacuum rated and therefore it became the major suspect. Before putting to the test the torque meter in open air, it was thought best to check the mechanical connections of the previous setup.

The main focus was set on the 3D printed supporting cage and on the coupling inside of it. The coupling, that has been discussed in section 2.2.5, is usually thought to have little importance in the setup. On the contrary, if the coupling is not able to accommodate the misalignment between the motor and the torque meter shaft, this can lead to serious mechanical problems.

When analysing the components used in the testing architecture, it was discovered that, with the torque meter datasheet, came also a suggestion on the best coupling to use when attaching other instruments to the torque sensor. The coupling recommended by HBM is

a miniature bellow coupling called MK1 5 23, produced by R+W Company. This coupling has different characteristics with respect to the Ruland one, as seen in Table 2.8.

	Ruland jaw coupling	R+W bellow coupling
Lenght	21.8 mm	23.0 mm
Outer diameter	15.0 mm	15.0 mm
Forged Clamping	M2	M3
Weight	9 g	6 g
Angular Misalignment	1.0°	1.5°
Rated Torque	0.27 Nm	0.1 Nm
Parallel Misalignment	0.13 mm	0.2 mm
Torsional Stiffness	14 Nm/rad	0.21 kNm/rad
Material	Aluminium/Polyurethane	Aluminium

Table 2.8: Comparison between coupling used and advised

As it can be seen, the joint advised by HBM is longer than the one that was previously used, but its lighter. In particular, it can be noticed that the misalignments that can be accommodated by the R+W coupling are slightly higher than the ones of Ruland's one. The MK1 joint has one grub screw per side, acting directly on the shaft inserted, to prevent it from moving, as it can be seen in Figure 2.27. In order to give the whole setup the best possibility to work at its best, the old coupling was replaced with the new advised one.



Figure 2.27: R+W MK1 miniature bellow coupling

The 3D printed cage suspending the motor was also suspected to decrease the accuracy of the measurements. Therefore, a new cage was built in aluminium with a similar design. The slots on the cylindrical surface were left to reduce the mass of the cage and because they make easier to fasten the coupling when both shafts are in place. The length of the cage was thought to be excessive, thus it was reduced. The outside diameter was increased to leave more space to the fastening screws on the torque meter side. The cage is made by two parts, a cylindrical part connecting to the torque meter (Fig. 2.28), and a lid that connects to the motor (Fig. 2.29). All the designed modifications had the aim to increase the stiffness of the cage structure, reducing deformations due to reactions forces applied to it.



## 2.6 Air Tests

To verify that the instrumentation did not suffer any damage from previous tests in vacuum conditions, it was thought optimal to reproduce torque tests at ambient density. These tests could not be performed with the same blade used in vacuum, since it was designed for low density atmospheres. Seen that the difference in Reynolds number between the two Martian and Terrestrial atmosphere is excessive, a new blade had to be chosen. The selection was quite challenging due to the low torque meter nominal limit. Thrust measurements were not acquired during this new testing campaign, considering that the swing architecture had given satisfactory results.

### 2.6.1 Air Propeller Selection

The aim of air tests is to check the truthfulness of the torque meter output and to do it, it has to be connected to a propeller whose torque characteristics are well known. The propellers, that were taken into considerations for the project, were the ones used in the study "UAV Powertrain Efficient Design Through a Model-based Approach" [18]. This study was selected because it performed tests on commercial drone propellers to analyse experimentally their coefficients  $c_Q$  and  $c_T$ . The  $c_Q$  values indicated in this study, as well as the ones of the University of Maryland's Martian blade, experimentally found by TAS-I in both air and Martian conditions, were used to define torque-speed trends for each propeller. The torque curves in function of the spinning speed were mathematically derived, knowing that torque coefficient  $c_Q$  can be expressed as:

$$c_Q = \frac{Q}{\rho \omega^2 D^5} \quad (2.15)$$

where:

- $Q$  [Nm] is the torque generated by the propeller;
- $\rho$  [kg/m<sup>3</sup>] is the atmosphere density;
- $\omega$  [rev/s] is the speed at which the propeller is turning;
- $D$  [m] is the diameter of the propeller.

Since the known  $c_Q$  for the University of Maryland's blade were expressed by the Equation 1.9, it had to be transformed to the new  $c_Q$  formulation as:

$$c_Q = \frac{\pi^3}{8} \cdot \bar{c}_Q \quad (2.16)$$

where the  $\bar{c}_Q$  indicates the  $c_Q$  value expressed by the previous formulation (Eq.1.9). Torque trends for the propellers were then plotted as in Figure 2.30.

The torque-speed characteristic of the Faulhaber motor, at different values of  $U_{mot}$  supply, was plotted against the propellers torque trends. The equation used to express the torque as a function of the speed is :

$$Q = \frac{k_T}{R} \left( U - R \cdot \frac{\omega}{k_V} \right) \quad (2.17)$$

that is derived by combining Equation 2.14 and Equation 2.5.

The air propeller that approximates best the torque trend of the Martian blade, when used in low density, is the 15"x5" L model (Fig.2.31). This propeller is manufactured by T-motor for commercial drone use. Its name represents the *propeller diameter in inches* $\times$ *pitch angle*. By referencing Figure 2.30, it can be highlighted that when the motor characteristic crosses a propeller trend, the point defined by that specific torque and speed can be a possible working point for that propeller driven by the motor at that specific voltage supply. In the case of the 15"x5" L blade, its torque trend encounters the motor torque twice around the 0.1 Nm limit: once under the limit and once slightly over. Even if the torque meter nominal torque is 0.1 Nm, the actual measuring limit for the instrument is set at 0.2 Nm by the producer. The manufacturer advises not to cross the nominal torque limit, but guarantees as well that, if the torque is less than twice the nominal limit, the instrument will not suffer any permanent damage when the limit is surpassed. It is, although, important to know that, if it is wanted to measure torques above the nominal limit, the accuracy of the measurement is not guaranteed and, in order to prevent accidents, the stay of the torque above its limit should be short. The voltage supply found suitable for testing the torque meter with the 15"x5" L propeller is  $U_{mot}=6$  V.

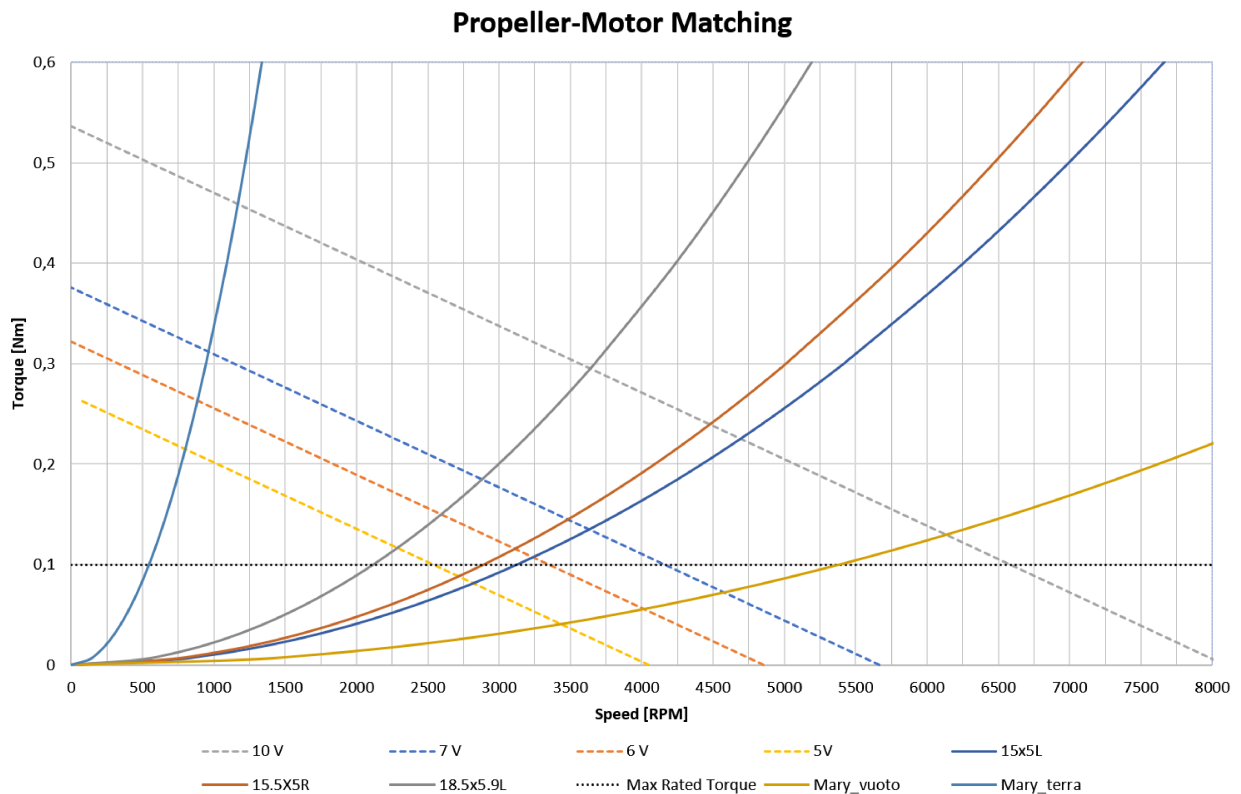


Figure 2.30: Torque-speed comparison for FAULHABER 2264W 024 motor and different propellers



Figure 2.31: T-motor 15"x5" L propeller and fixing cover

The 15"x5" L T-motor propeller does not have an external hub, since it is designed to be accommodated directly over a motor shaft when used for drones. The middle section of the propeller is untwisted and has three bores that are used to fix it on the motor shaft, whose schematic is represented in Figure 2.32. Luckily, the shaft bore for this blade has exactly the same diameter of the torque meter measuring shaft, allowing to place the propeller directly on the torque sensor. In order to fasten the propeller in place, the T-motor company includes a cover that is connected with two M3 screws to the motor shaft.

Considering that the propeller, in this case, has to be positioned on the torque meter shaft and that the shaft is not specifically created to be attached to a propeller, a suitable connector was designed and built, as it can be seen in Figure 2.33. The hub for T-motor propeller has been designed in aluminium to keep it light in weight. It is furnished of a pass-through-hole that houses two M3 grub screws for fixing it on the torque meter shaft. The hub was positioned close to the torque meter main body surface in order to reduce the flexural moment on the shaft and it was controlled that its weight would not overcome the radial force limit of the torque meter. All air tests have been performed by fixing the structure shown in Figure 2.34 to a wooden plate that was positioned as a cantilever from a table surface.

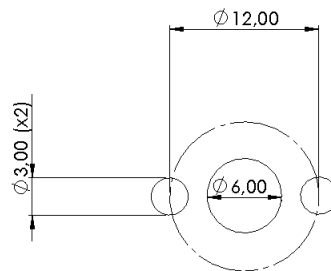


Figure 2.32: T-motor fixing cover scheme

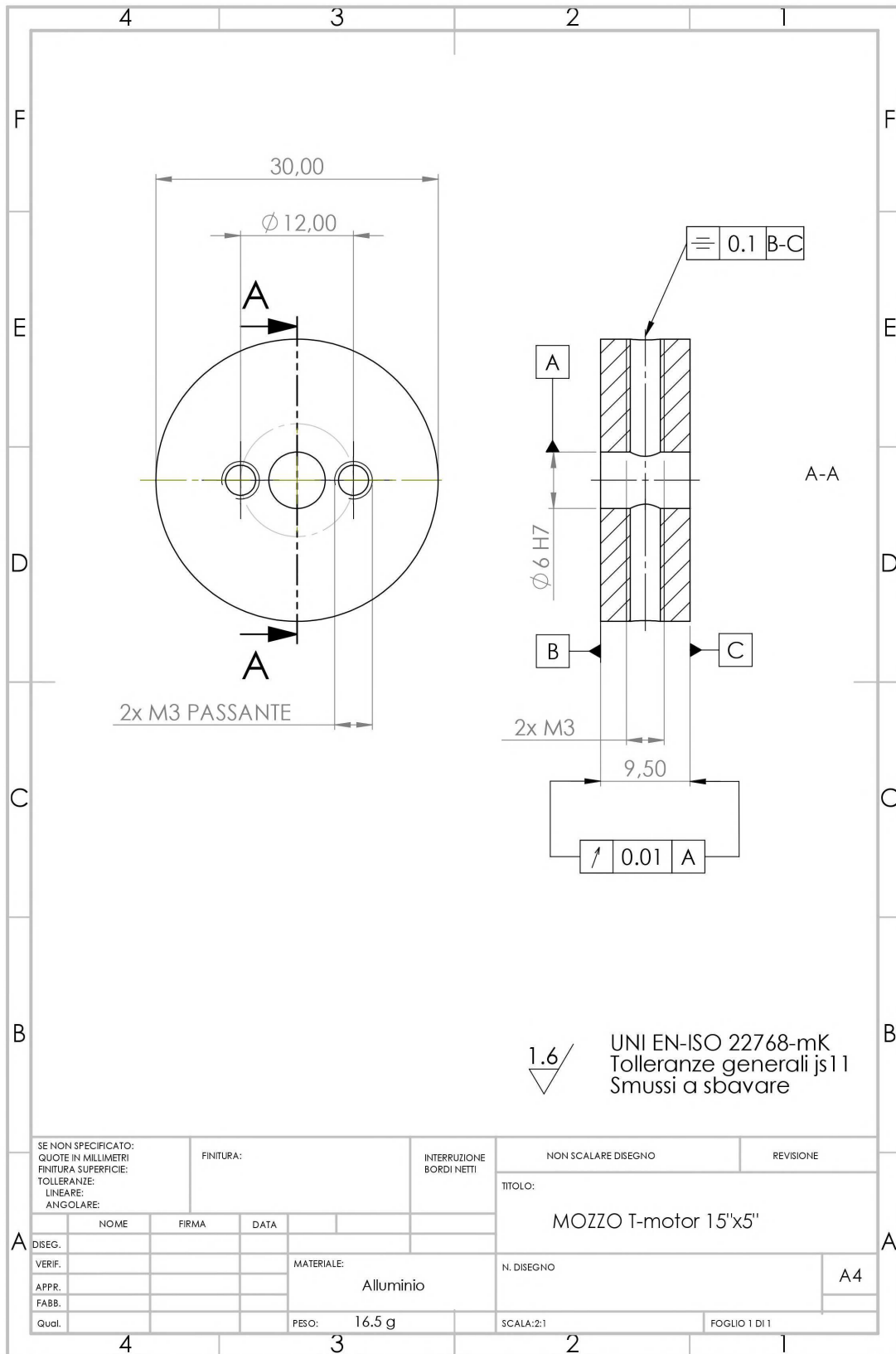


Figure 2.33: T-motor 15"x5" L connector for HBM T21WN torque meter

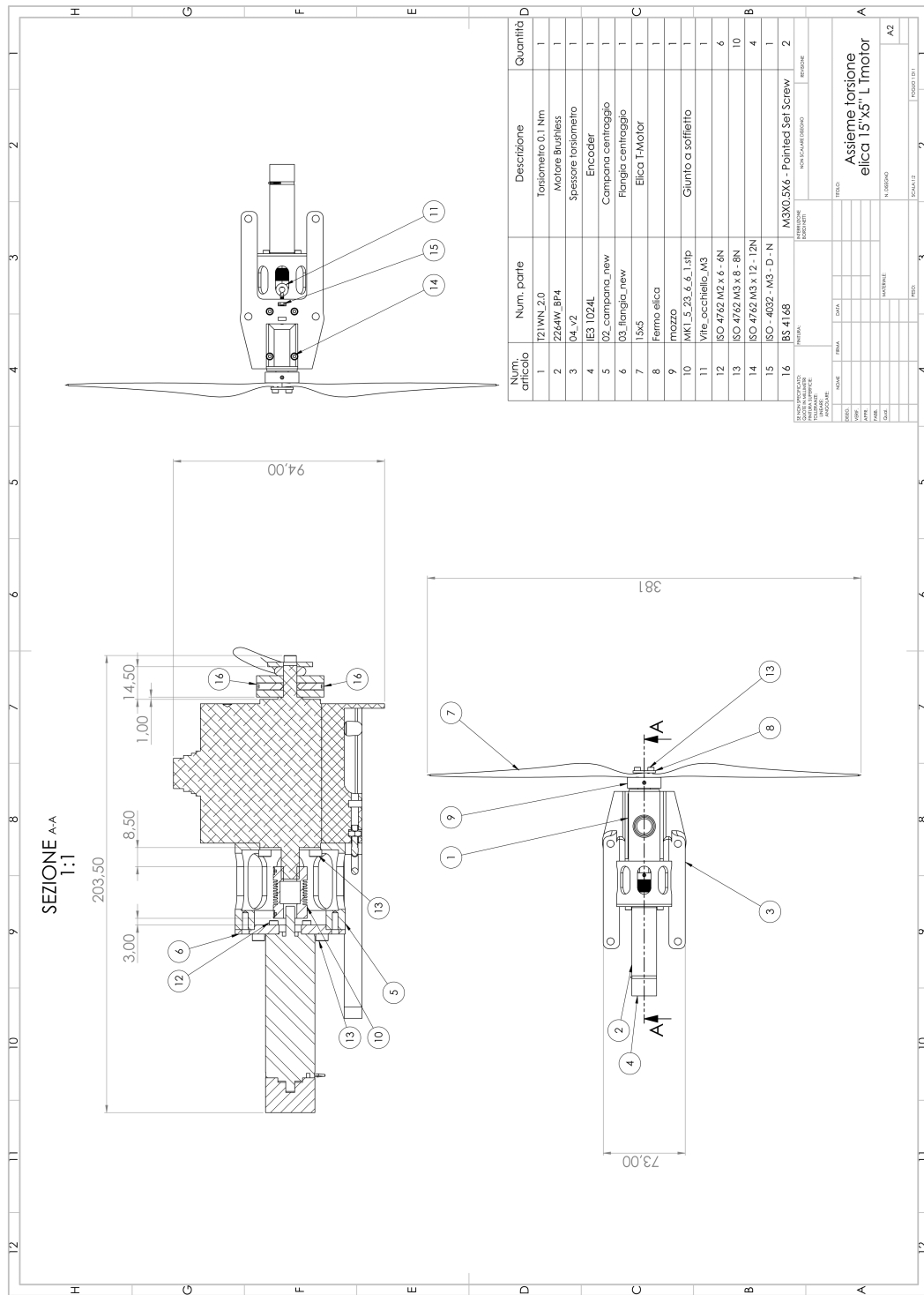


Figure 2.34: Test bench used for torque testing in standard air

## 2.6.2 Acquisition & Supply System

While the mechanics of the torque test bench was kept similar to the one used in vacuum test, with the exception of the modifications discussed above, the electronics was completely revised. The electronic system of this project has two main duties:

- Supply power to the ESC and to the torque meter;
- Acquire data from the test bench.

In order to determine whether the system would function in air, some physical parameters of the test bench were acquired during testing. Signals collected are the following ones:

- Current absorbed by the motor;
- Propeller speed;
- Generated torque;
- Motor voltage supply;
- Motor control voltage.

In order to acquire the above listed physical quantities, the system was composed by several instruments. The motor supply,  $U_{mot}$ , was fed by a TTI-CPX400DP, a 2 channels DC power supply. A 1 m $\Omega$  shunt, as it can be seen from Figure 2.35, it was positioned in series with the positive  $U_{mot}$  supply.

The low value of this resistor mimics well the internal resistance of the motor supply cable. The voltage was read at the resistance's terminals by an HP 3547A digital multimeter with 6<sup>1/2</sup> digits precision. The voltage measurements were performed by the multimeter only when it was reached by an external trigger signal. The external trigger signal sent to the multimeter has to be a TTL square wave, and the measurement happens when on the downside of the wave.

Knowing the voltage at the terminals of the resistor and the resistance value, the current absorbed by the motor can be calculated as:

$$I_{mot} = \frac{V}{R} \quad (2.18)$$

where:

- $I_{mot}$  [A] is the current absorbed by the motor;
- $V$  [V] is the voltage measured at the resistor ends;
- $R$  [ $\Omega$ ] is the resistance chosen value.

The torque meter was supplied by a constant voltage, given by a Eutron BVD450 power supply. The torque was acquired as a voltage signal, similarly to what was done in vacuum tests. In this phase of the testing, the speed was read through one of the torque meter encoder channels that was preventively checked to work correctly. This choice helped in reducing the number of electrical connections needed, since the torque meter top connector enables to read the preferred outputs with only one cable. During

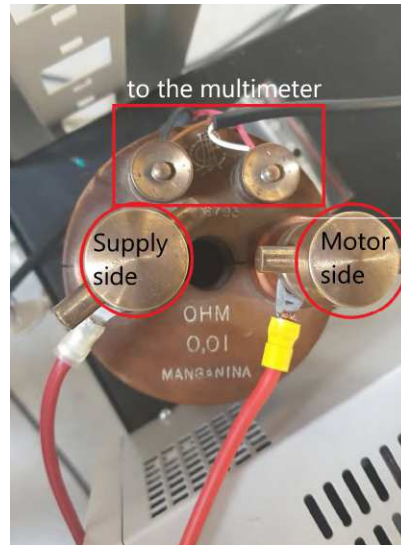


Figure 2.35:  $1\text{m}\Omega$  shunt used to acquire the current absorbed by the motor

the air testing, it was available for use the junction box specific for this torque meter. This device helps to filter input supply voltage for the sensor and outputs produced, as well as to provide easy connections with different instrumentation.

All systems outputs were regulated by an Electronic Control Unit, whose schematic is represented in Figure 2.36. It can be seen that all signals inputs, on the right of the scheme, are handled by the electronics in PCB, for example the speed signal is passed through a divider that acts as a filter, while the torque measurement is not modified since the noise rejection process is already done by the junction box.

By analysing the result given by the motor and ESC characterization, it was thought best to control the motor by a PWM voltage signal, bypassing the speed control loop. The PWM signal, sent to  $U_{nsoll}$ , was generated by a multifunction I/O DAQ. This data acquisition system, used also to acquire all analog data, is the NI USB6211 model. This board has 16 analog input channels, 2 analog output channels, 4 digital inputs and 4 digital outputs. The 8 digital channels can be also used as 2 digital counters. Digital counters are device able to analyse and store how many times a certain event occurs over a span of time; this analysis is base on the internal clock of the board and allows to output a PWM voltage as well as reading directly the frequency output of a speed encoder.

A digital channel was chosen to output the external trigger signal to the multimeter. Torque, speed and motor voltage were acquired, through the USB6211 board, as analog inputs. Analog inputs were connected in a differential configuration, as it can be seen in Table 2.9, meaning that the voltage reference signal is delivered by the pin following the one acquiring the specific quantity. Both the counters were used: the input of the first one was used to read the speed signal coming from the encoder, while the output of the second one was employed to produce the PWM signal. In order to be recognized by the ESC, the PWM signal has to be a square wave between 0 and 5 V. The USB6211 has a maximum output limit equal to 5 V, but it was found to be inadequate for the ESC, due to the losses in the connections between the two. To bypass this problem, the PWM signal generated by the DAQ was set as input to two 10 V powered N-channel MOSFETs connected in series; in this way, a new square wave with amplitude 10 V, and the same

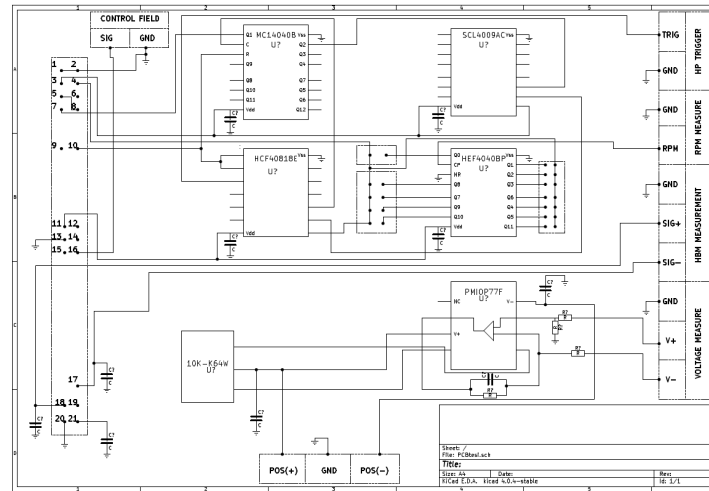


Figure 2.36: Electronic Control Unit Schematic

duty-cycle as the one produced the DAQ, was forwarded to the ESC driver. The MOSFETs circuit was implemented on an external breadboard.

The USB6211 board, as well as the motor supply and the multimeter, were controlled by a MATLAB code, designed for these tests. The voltage supply and the torque meter were connected to the computer through GPIB interface, while the DAQ system communicated via USB. MATLAB code was designed with the *Session-based Data Acquisition Toolbox* that helped to interact with the board; instead the command to the other instruments were given in SCPI language.

The code was structured in four parts:

1. Preliminary configuration and output setting for GPIB instruments;
2. Configuration of DAQ active channels and control signal;
3. Data acquisition;
4. Stopping instruments outputs and DAQ channels.

Data acquisition process was done either by setting the PWM to 100% duty cycle, in order to saturate the control of the motor, and increasing the  $U_{mot}$  voltage supply, or by setting  $U_{mot}$  to a specific voltage value and increasing the PWM duty-cycle.

In both cases, data acquisition was done in stable working conditions, meaning that after the voltage variable had been increased as a ramp, the system would start acquiring signals after a time pause of selected length. This time pause helped to acquire data without including overshoot or settling that may be due to the external control given. The control and acquisition process is sketched in Figure 2.37. The control ramp height, called  $h$  was performed by the control signal in  $n$  small steps, in order do not give an excessive voltage change to the motor, that may lead to damages. Once data acquisition is finished, another ramp will follow until the maximum control voltage equals the limit set in MATLAB code.

MATLAB code also enable to store directly from GPIB connection the voltage read by the multimeter. The data acquisition for USB 6211 channels was done either a 1000 Hz for a couple of seconds after each ramp, or at 10000 Hz, disabling the speed counter. Data were then averaged and their mean value as well as their standard deviation error was collected in a matrix, referencing the rotational speed, the current absorbed and the control parameters for that particular acquisition point.

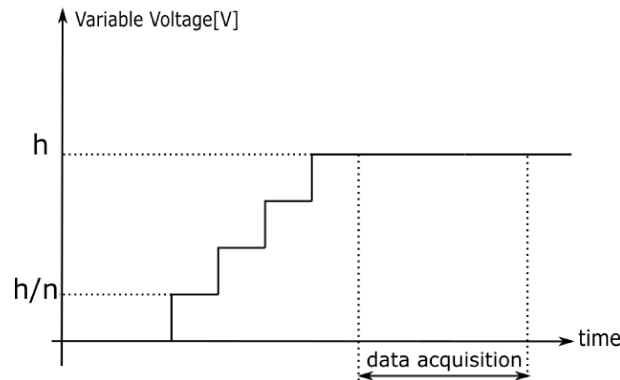


Figure 2.37: Ramp cycle for data acquisition

### Filtering Torque

Some preventive tests were done in order to better understand the working principle of the torque meter. These tests were performed at fixed speed and only the torque was acquired at 10 kHz. It was noticed that the torque measurement was altered by some electric noise. It was then chosen to proceed and filter the torque signal with a low pass RC circuit with cutting frequency  $f_C=150\text{Hz}$ . The passive filter was implemented on the breadboard where the circuit for amplifying PWM signal was also positioned. The filtered result, plotted in Figure 2.38, is visibly less dispersed and assures a higher accuracy in the measurement. For all the following tests the torque was read both filtered and unfiltered with two different analog input channels dedicated on the USB6211 board.

The possibility to implement a digital filter on MATLAB, to filter the acquired torque data in post process, was investigated. The digital RC filter, equivalent to the physical one connected to the DAQ, gave satisfactory results, but it was though that in this first phase of testing it would be more convenient to use the analog one.

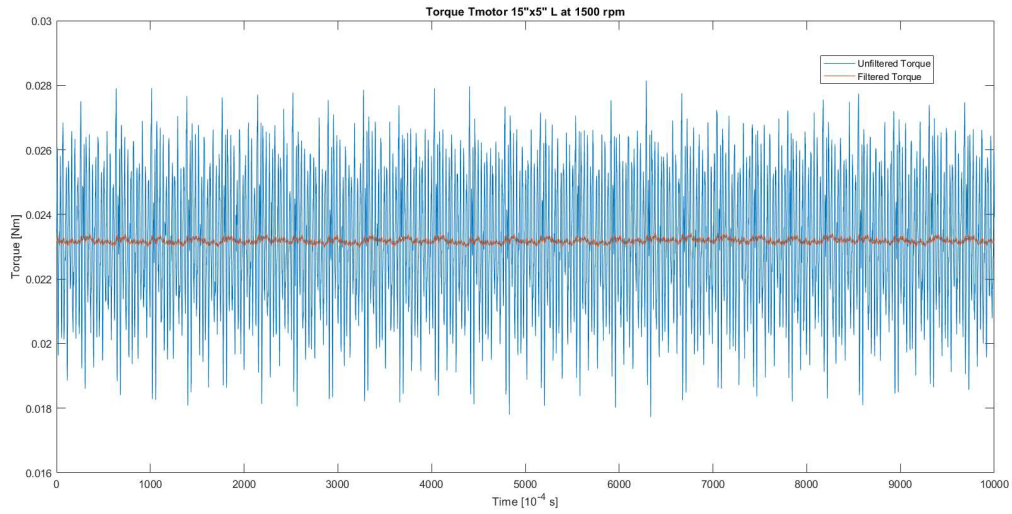


Figure 2.38: Comparison between filtered and unfiltered torque signal acquired at 10 kHz

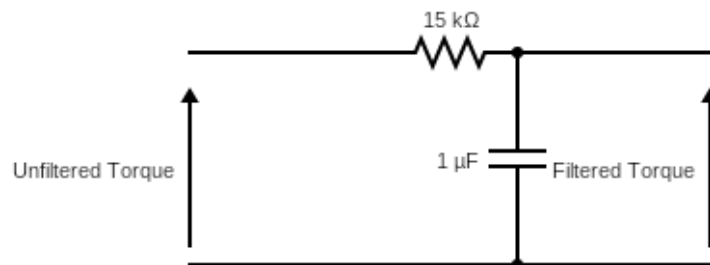


Figure 2.39: Passive low pass filter with cutting frequency  $f_c=15$  kHz

Signal Type	Default Terminal Number	Use of signal
PFI 0/P0.0 (In)	1	-
PFI 1/P0.1 (In)	2	Speed Encoder
PFI 2/P0.2 (In)	3	-
PFI 3/P0.3 (In)	4	-
D GND	5	Digital Reference Signal
PFI 4/P1.0 (Out)	6	Digital Output Trigger
PFI 5/P1.1 (Out)	7	PWM Rate Generator
PFI 6/P1.2 (Out)	8	-
PFI 7/P1.3 (Out)	9	-
+5V	10	-
D GND	11	-
AO 0	12	-
AO 1	13	-
AO GND	14	-
AI 0	15	-
AI 8	16	-
AI 1	17	Bus Voltage Signal
AI 9	18	Differential Reference Signal
AI 2	19	Filtered Torque Voltage Signal
AI 10	20	Differential Reference Signal
AI 3	21	Non-Filtered Torque Voltage Signal
AI 11	22	Differential Reference Signal
AI SENSE	23	-
AI 4	24	-
AI 12	25	-
AI 5	26	-
AI 13	27	-
AI GND	28	-
AI 6	29	-
AI 14	30	-
AI 7	31	-
AI 15	32	-

Table 2.9: USB 6211 pin out table

### 2.6.3 Firsts Results

The motor characterization, performed in section 2.4.2, displayed that the motor would run with the parameters shown in the datasheet only when the speed control loop is disabled and the control signal  $U_{nsoll}$  is saturated. Therefore, keeping  $U_{nsoll}$  signal fixed and varying the motor supply seemed the better way to achieve accurate measurements. Anyhow, it was decided to perform also a test with varying  $U_{nsoll}$  and fixed  $U_{mot}$  to show the practical differences between the two experiences.

Torque results, acquired in air with the 15"x5"L propeller, were plotted with respect to the speed and compared with data defined by the study [18] for the same propeller. It was also sketched the torque trend for higher velocities, computing an experimental  $c_Q$ , considering the air density adjusted in normal air. The correction was done by rectifying the air density with respect to the temperature and pressure acquired with the perfect gas law define by the Equation 2.1.

The coefficient  $c_Q$  for the new test campaign was slightly lower than the one previously found, as it can be seen in Figure 2.40, but this small error could be due to the different instruments used.

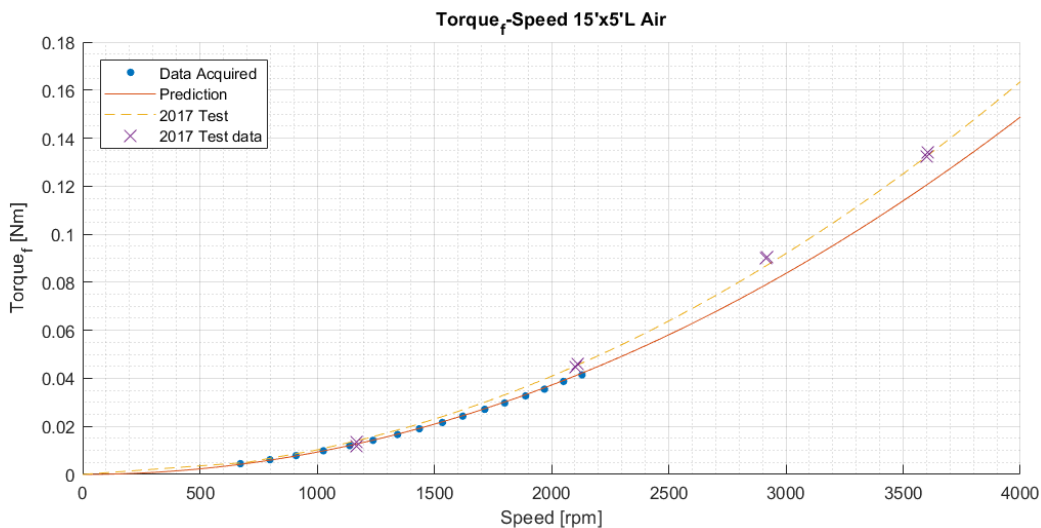


Figure 2.40: Torque-speed characteristic of 15"x5" L acquired compared with state of the art

The major difference found between the two diverse control types for the motor was, as suspected, linked to the torque calculated through the motor constant  $k_T$ . The torque, as defined by Equation 2.4, considering the current acquired by the multimeter, was plotted in a speed-torque chart. It can be seen, from Figure 2.41, that when the PWM control signal was saturated, the torque acquired by the torque meter and the one calculated with motor parameter are parallel with a constant negligible error. The same cannot be said when the fixed signal is the motor supply: in this case, the torque calculated is largely lower than the one acquired, reaching the same value only when the PWM attains the 100% of duty-cycle.

The torque could be, therefore, approximated by the Equation 2.4 whenever the variable signal is set to be the motor supply. It is important to underline that if this approach will be chosen in future tests, it is of major importance to check that the motor control

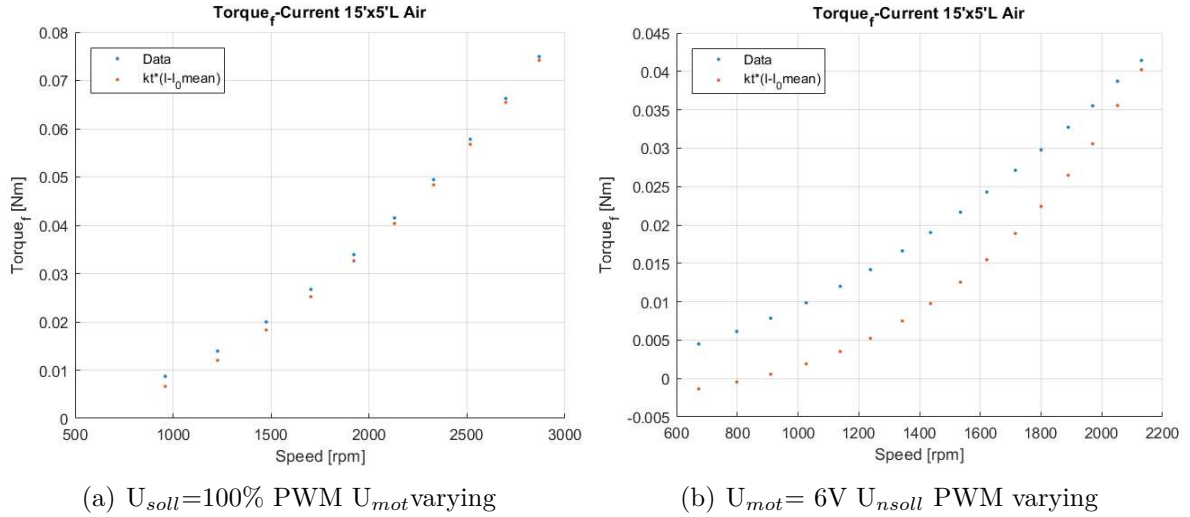


Figure 2.41: Variation of motor torque with different control methods

is saturated and that no speed loops are enabled in the driver. If a new motor will be used, it would be advisable to re-perform the  $k_T$  characterization tests to ensure that the experimental coefficient is similar to the one written in the motor datasheet.

For these tests, the efficiency of the propeller was calculated as:

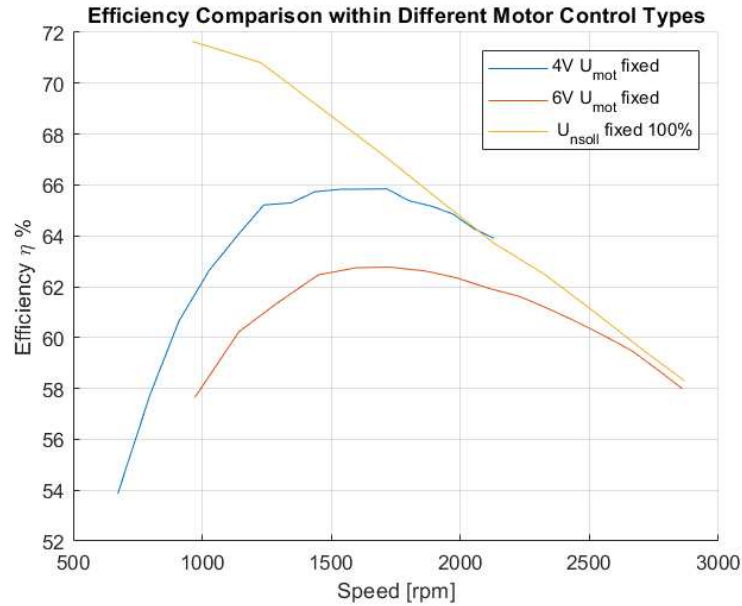
$$\eta = \frac{P_{out}}{P_{in}} \cdot 100 = \frac{Q \cdot \omega}{V \cdot I} \cdot 100 \quad (2.19)$$

where:

- $\eta$  [%] is the rotor efficiency;
- $P_{out}$  [W] is the mechanical power produced by the motor;
- $P_{in}$  [W] is the electrical power given to the motor;
- $Q$  [Nm] is the mechanical torque generated by the propeller;
- $\omega$  [rad/s] is the spinning speed of the propeller;
- $V$  [V] is the voltage supplied to the motor;
- $I$  [A] is the current absorbed by the motor.

Since the current absorbed by the motor changed with respect to the control used, the overall system efficiency changed as well. In the test, with  $U_{soll}$  fixed at 100% of duty-cycle,  $U_{mot}$  was increased up to 6 V, while when  $U_{soll}$  was varied between 0% and 100 % of duty-cycle, the motor supply was fixed at either 5 or 6 V. It can be noticed that the efficiency of the propeller is higher when the motor is controlled by changing the supply tension  $U_{mot}$ . This difference is more evident for lower speeds, while for higher velocities the efficiency trend is reaching an oblique asymptote.

Summing the contributes from the ESC characterization and these tests, it was chosen to use the the  $U_{mot}$  as a control voltage and keep  $U_{soll}$  at its 100% duty-cycle for all future



experimental campaigns.

Tests with the  $U_{mot}$  used as a control parameter were performed several times in different days to test the repeatability of the measurement. The results were coherent each time. The mean  $c_q$  values found for different run were the following:

Test Run	Mean $c_Q$	Stand Deviation Error
$U_{mot}$ fixed at 4V	0.0035	$7.999 \cdot 10^{-5}$
$U_{mot}$ fixed at 5V	0.0034	$2.503 \cdot 10^{-5}$
$U_{nsoll}$ fixed at 100% and $U_{mot}$ up to 6 V	0.0034	$3.963 \cdot 10^{-5}$
$U_{nsoll}$ fixed at 100% and $U_{mot}$ up to 6 V	0.0034	$2.809 \cdot 10^{-5}$
$U_{nsoll}$ fixed at 100% and $U_{mot}$ up to 6 V	0.0034	$4.068 \cdot 10^{-5}$
$U_{nsoll}$ fixed at 100% and $U_{mot}$ up to 6 V	0.0034	$4.068 \cdot 10^{-5}$
$U_{nsoll}$ fixed at 100% and $U_{mot}$ up to 5 V	0.0034	$5.906 \cdot 10^{-5}$
$U_{nsoll}$ fixed at 100% and $U_{mot}$ up to 5 V	0.0034	$5.718 \cdot 10^{-5}$

Table 2.10:  $c_Q$  value distribution in different test runs

For all tests, error distribution plots were sketched helping to visually see the different standard deviations between the acquired filtered torqued and the unfiltered one, as it can be noticed in Figure 2.42. Moreover it was checked the correlation between the speed  $\omega$  and the torque value  $Q$  defined in aerodynamic literature for a propeller as:

$$Q \propto \omega^2 \quad (2.20)$$

To do so a polynomial regression was adapted to the found torque values, as seen in Figure 2.43 and the closer the  $x$  exponent is to 2, the better the behaviour of the propeller.

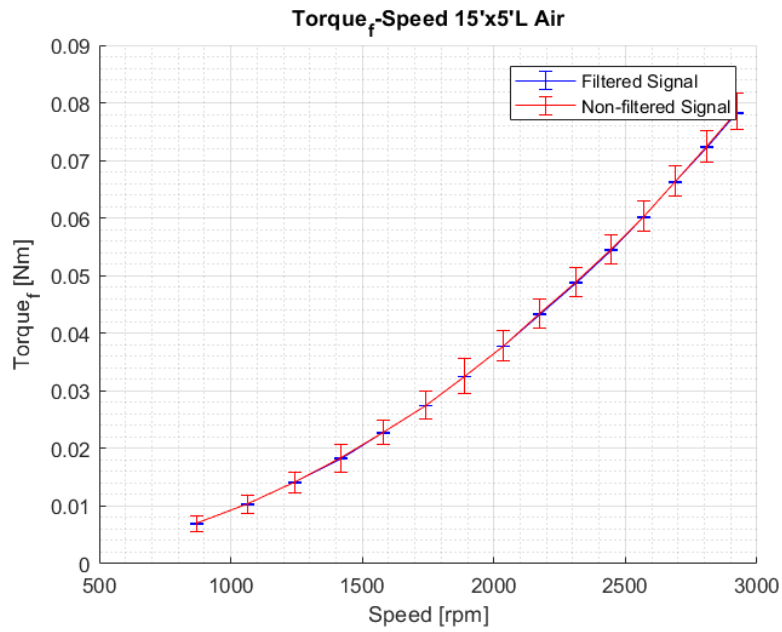


Figure 2.42: Errorbar plot comparing acquired filtered torque and unfiltered.

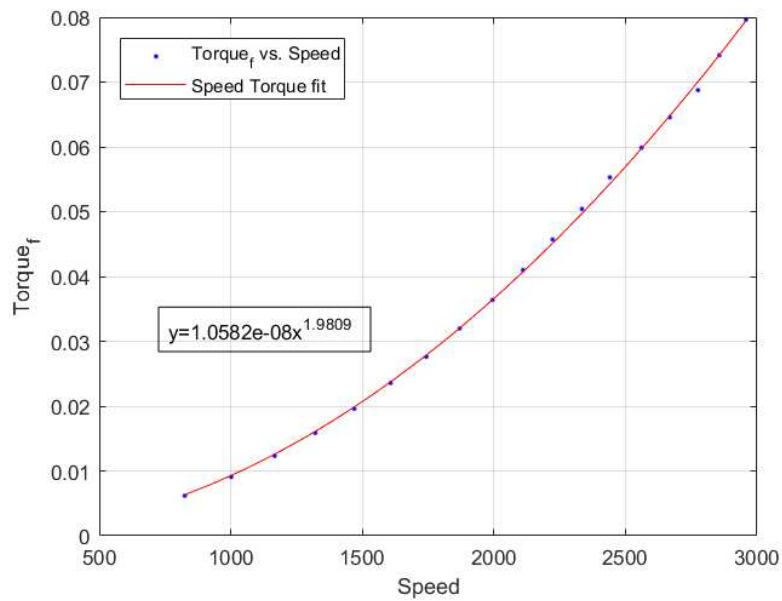


Figure 2.43: Torque polynomial regression

### 2.6.4 Vibration Tests

Vibration analyses for the torque measurements were performed using the same procedure followed in section 2.3.1. In this case, it was evident that the torque measurements were suffering from high order harmonics when not filtered. Waterfall plots were analysed for both filtered torque, as well as non-filtered torque. From this comparison, it can be seen that the filter applied to the torque is well functioning, since the amplitude of higher order vibrations is dampened. The harmonics showing higher amplitudes in Figure 2.44 are the orders x4, x8, and x12, it can be spotted also a possible critical speed around 450 Hz. In both filtered and unfiltered torque plots, it is highly present a x12 harmonic: this harmonic is most certainly due to the commutation torque ripple of the BLDC motor. The commutation torque ripple is a problem that affects many electrical motors, it is defined as a non-linear torque production cause by the stator windings excitation. A trapezoidal BLDC motor as the one used for this project has 3 phases, whose position is controlled by 3 Hall sensors; this configuration makes the torque ripple appears 12 times in a full mechanical rotation. This phenomenon has been studied as a control problem in electrical motors, in particular in a study from the University of Tianjin [20] has developed a mathematical model which defines the generated torque as:

$$Q = Q_0 + \sum Q_i \cdot \sin(i\omega t) + \sum Q_i \cdot \cos(i\omega t) \quad (2.21)$$

where:

- $Q$  [Nm] is the total generated torque;
- $Q_0$  [Nm] is the expected torque with the DC voltage supplied to the motor;
- $Q_i$  [Nm] are the amplitudes of the different harmonics introduced by the torque ripple, and  $i=6, 12, 18$ .

Sophisticated control algorithms have been improved to reduce the commutation ripple torque, but as seen from the waterfall plot for filtered torque, the passive filter seemed to work fine enough for this characterization of the architecture. Usually, the torque ripple of a motor could be neglected because it is limited in amplitude with the respect of torque measurements. In the case of this project, this could not be done since the torque meter is designed to read extremely low torques. The torque meter has a sensitivity of  $3 \cdot 10^{-3}$  Nm and therefore the torque ripple is fully acquired by the sensor, disturbing the propeller torque measurements.

### SCADAS

All vibration analysis, up to this moment, were computed with MATLAB; to ensure that the waterfall plots collected in this way were reliable, a counter vibrational analysis was performed with the help of SCADAS technology. Speed and torque, filtered and not, were acquired by the system at 2000 Hz while the system was set spinning by the MATLAB code already discussed.

The results of the different tests have been plotted in colour maps. The orders of the harmonics found were the same achieved with MATLAB code, meaning that the algorithm was reliable. In particular, it can be noted that in Figure 2.46 the x12 harmonic shows red peaks, meaning that its amplitude is larger than the other orders. Changing the  $x$  axis from frequency to order, harmonics are not represented anymore as diagonal lines,

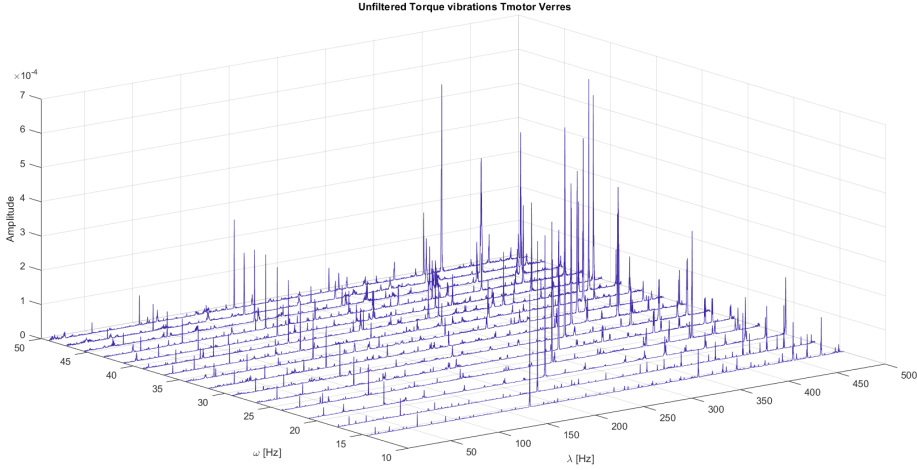


Figure 2.44: Unfiltered Torque Vibration

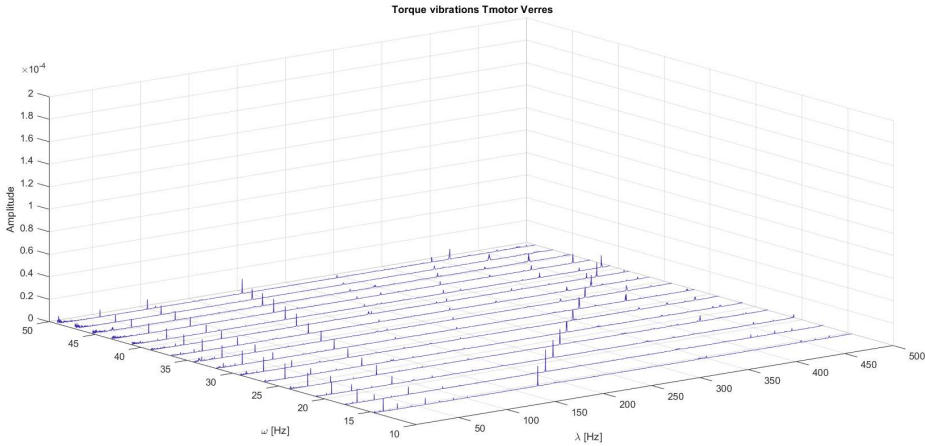


Figure 2.45: Filtered Torque Vibrations

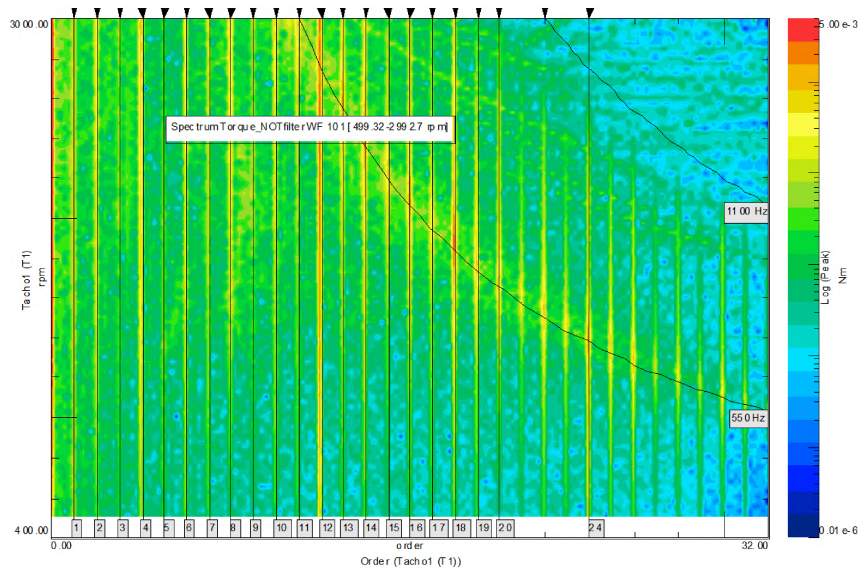


Figure 2.46: Colour map for unfiltered torque vibrations by harmonics

but as straight verticals. In the same way, critical speeds become hyperbolic shaped when they are plotted with reference to order: in this particular case, the critical speed at 550 Hz it is highly remarkable. The speed vibrations were also plotted in a colour map, with frequency along the  $x$  axis and confirmed that the most important harmonic for this signal is the first one. The filtered torque showed none or little peaks, therefore, it was chosen to plot in a waterfall chart.

In particular another test was done with the SCADAS system on the measuring chain: a hammering test, also known as an impact test. Hammering is a test performed by gently hitting with an impact hammer the system in static conditions and acquiring its vibrations. Vibrations were acquired by two high accuracy accelerometers positioned as shown in Figure 2.49. The accelerometers were perpendicular one to the other, to acquired the system vibrations in different axes. This procedure is done to define whether there are some resonance frequencies for the architecture. Several hammering tests were done, hitting in different directions. The plot 2.50 represents the frequency response function (FRF) of the system, whose amplitude is defined as the force of reaction to the hammering normalized over the gravity constant. Frequency amplitude peaks defines the presence of natural frequencies or resonances. In the plot here represented it is evident a peak around 90 Hz as well as a smaller one circa at 500 Hz. How large the base of peaks is, defines how much the system is able to dampen vibrations, the narrower the more dampened it is. It has to be said the positioning of the setup during this experimental campaign was not the final one and therefore it was not optimized to reduce vibrations, that is why the hammering test results are not smoother.

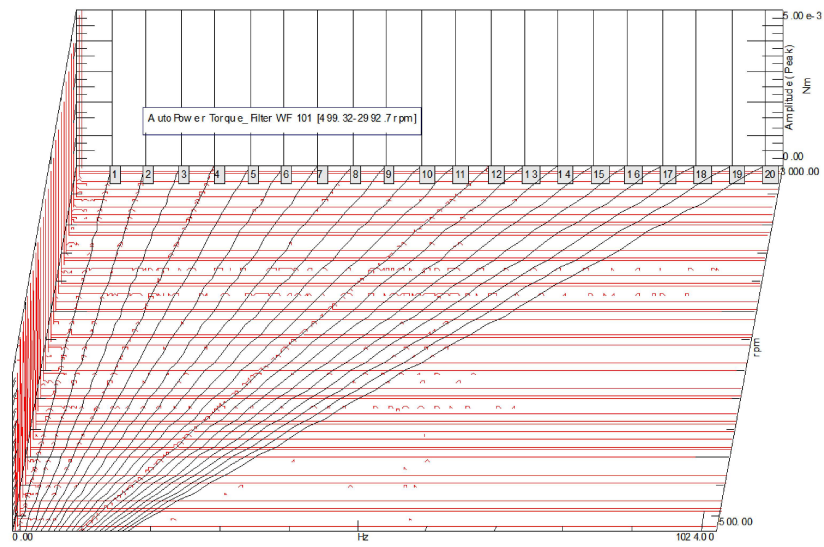


Figure 2.47: Filtered torque waterfall plot

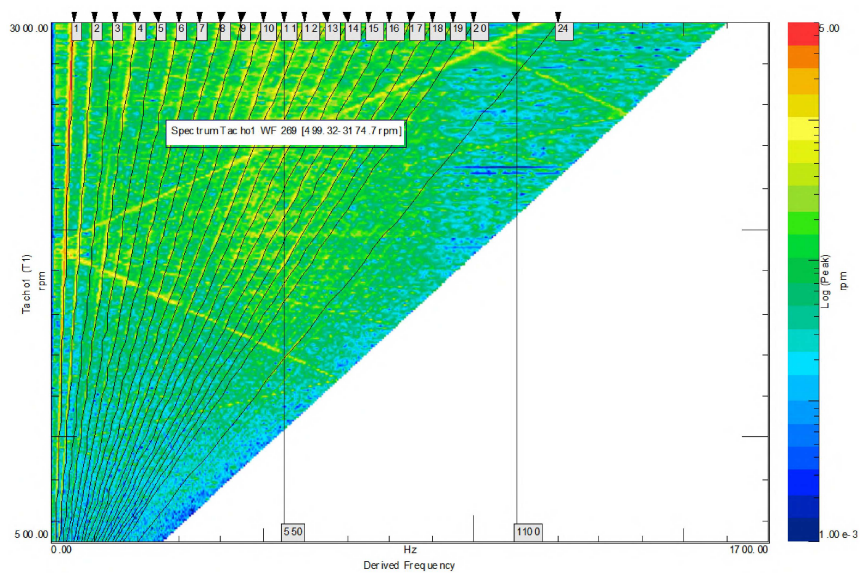


Figure 2.48: Colour map for speed vibrations

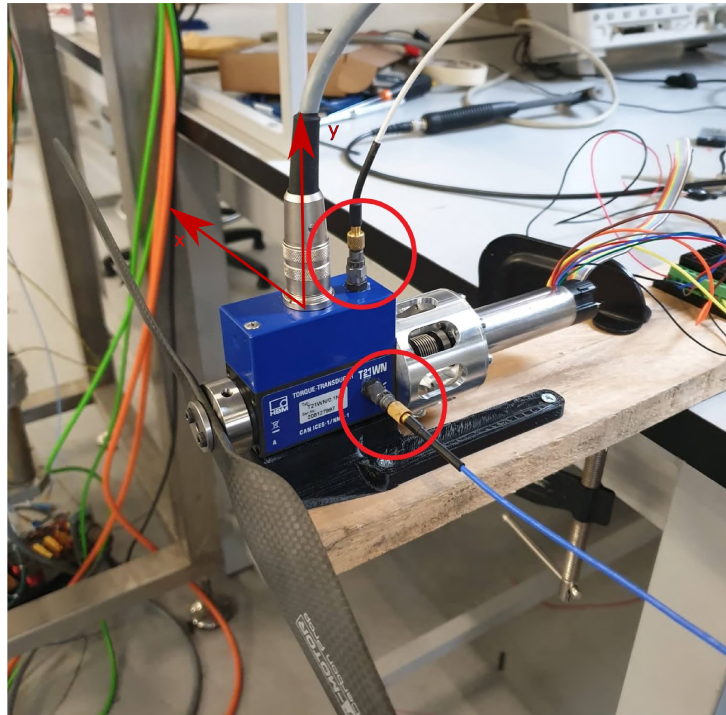


Figure 2.49: Accelerometers positioning for hammering test

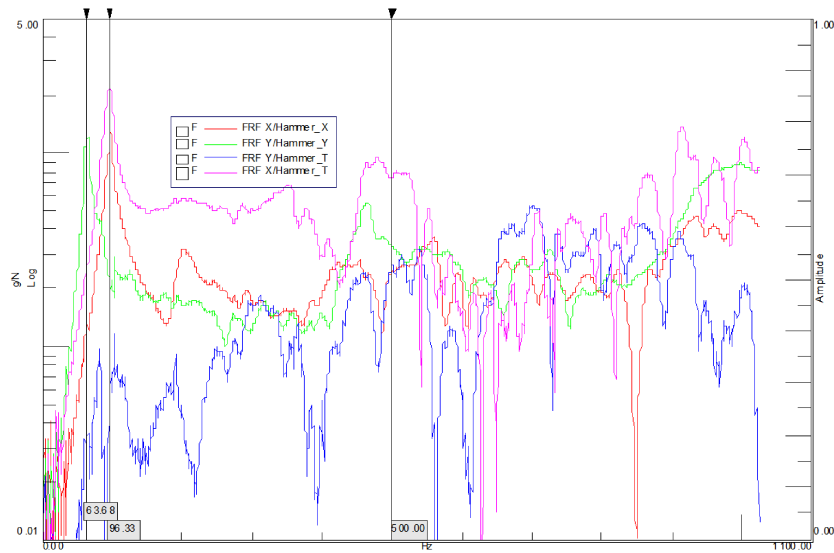


Figure 2.50: Hammering test results

### 2.6.5 Simulation of Vacuum Chamber Electrical Connections

Standard air tests defined that the torque meter, with the appropriate filtering, was working as it should do in conventional atmosphere. It was, then, envisioned to try and re-perform a vacuum performance test for this architecture to understand if the electrical and mechanical changes, applied to the configuration, influenced the behaviour of the setup in Martian-like conditions.

Before placing all components in vacuum, a last test was performed in air. This test was done to check if the electronics connections would suffer when attached to the vacuum chamber. It has to be underlined that cables connecting the instruments inside the chamber to the outside world, with serial ports, have to be quite long. This normally could lead to voltage losses, but it is even more important when the cables are connecting the ESC driver to its motor. It is advisable, when working with an electric motor, to position the ESC as close as possible to the motor, in order to prevent power losses. Moreover, the voltage supply should be also near to the ESC because, over time, long cables may degrade the ESC functionalities. This procedure could not be applied when working with a vacuum closed chamber because the power voltage supply has to be outside to set it and control it, and in this particular case the ESC could not be positioned in low pressure since it was not vacuum rated.

To test if the length of the cables influences the behaviour of the motor or the torque sensor, a set of long cables was created. Cables were split in two parts and connected with a male-male rs232 port to simulate the flange connections of the vacuum chamber. All the electronics used to control inputs and outputs was arranged on a strip-board. The strip-board, described by the scheme in Figure 2.52, helped to collect signal and voltage supplies in a more organized way. On the board two normally open switches were inserted: one defining the spinning direction of the motor and the other one allowing the torque meter reference signal and the motor ground to be in common. The PWM output was in series with two MOSFETs powered by the same voltage as the one supplying the motor electronics. This circuit represented the same used in first air tests to help produce a PWM signal compatible with the ESC TTL logic. Two RC filters were implemented: one to filter the torque, while the second one was to filter the value of  $U_{mot}$  measured experimentally. The filter applied on the  $U_{mot}$  signal has a cutting frequency  $f_c$  of 150 Hz, implemented as the filter applied on torque signal. In previous tests, the  $U_{mot}$  signal did not require an external filter since it was already filtered by the ECU electronics, that would not be available in TAS-I facility and therefore was bypassed in this test.

The strip-board circuit was first tested with the same connections used for all other air tests to check that it was working correctly. Once this test was passed, the test simulating the connections used in the vacuum chamber was performed. Data acquired from this test were not as satisfactory as the ones found in all other air tests. It was noticeable a high increase of the noise in the torque measurement when the current absorbed by the motor reached the 6 A limit, defined by the datasheet for thermal issues in long operating times. This problem caused a small deflection in the torque measurement as it can be seen from the plot represented in Figure 2.53. This variation of standard distribution could also be due to interference between cables. Cables were not shielded and therefore if close enough voltage signals could interfere with one another.

With this test it was possible to understand, that once the setup was placed in the

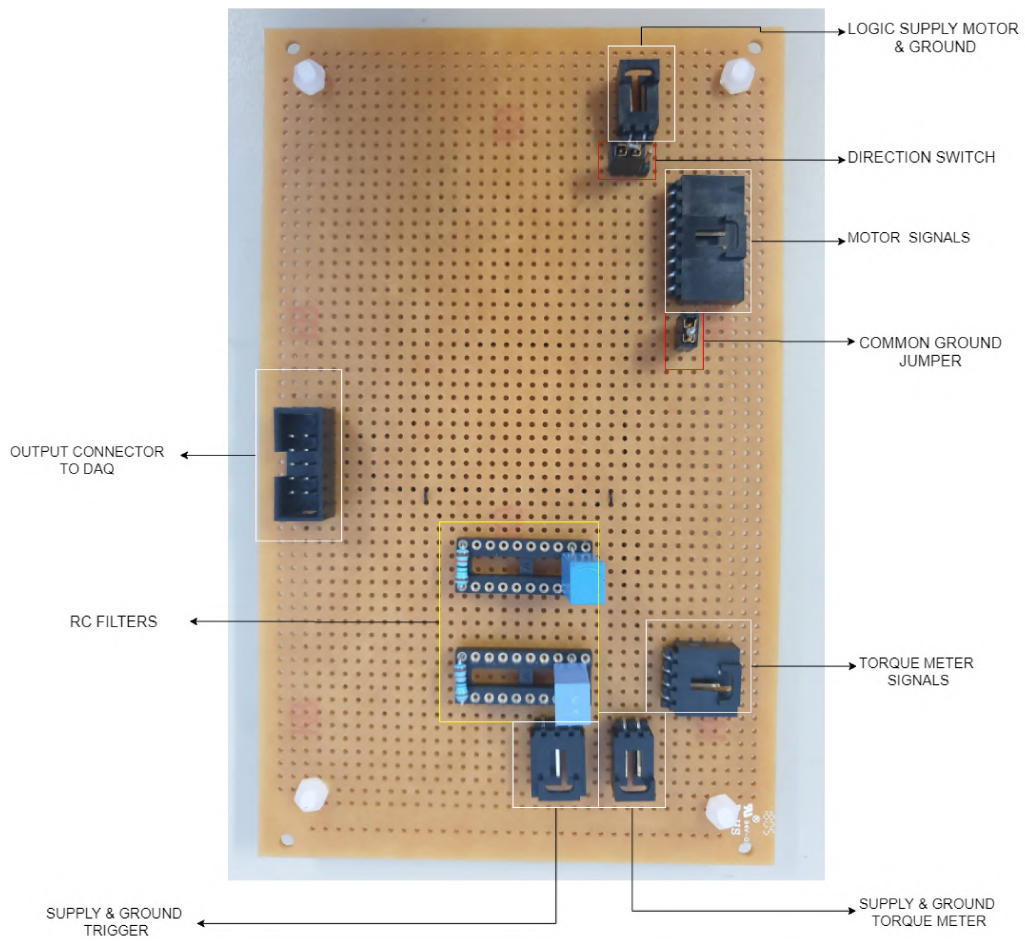


Figure 2.51: PCB inputs and outputs for propeller performance testing



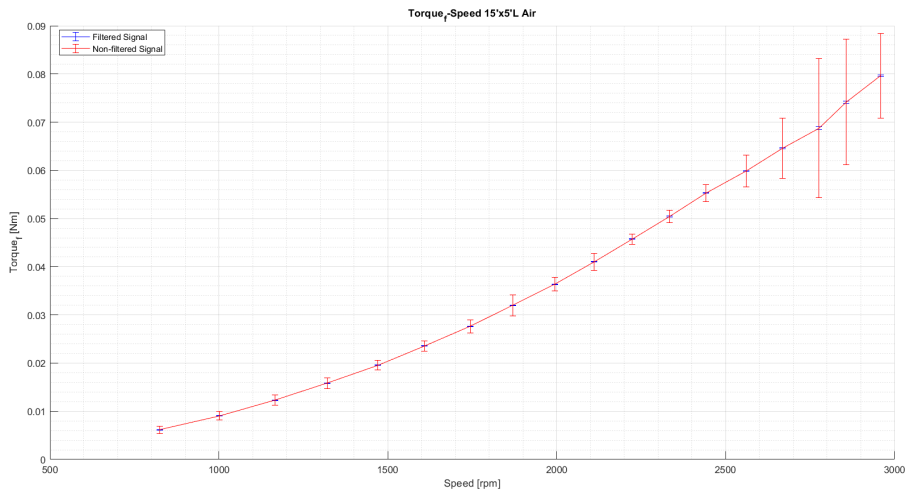


Figure 2.53: Errobar plot for acquired torque with long cables set

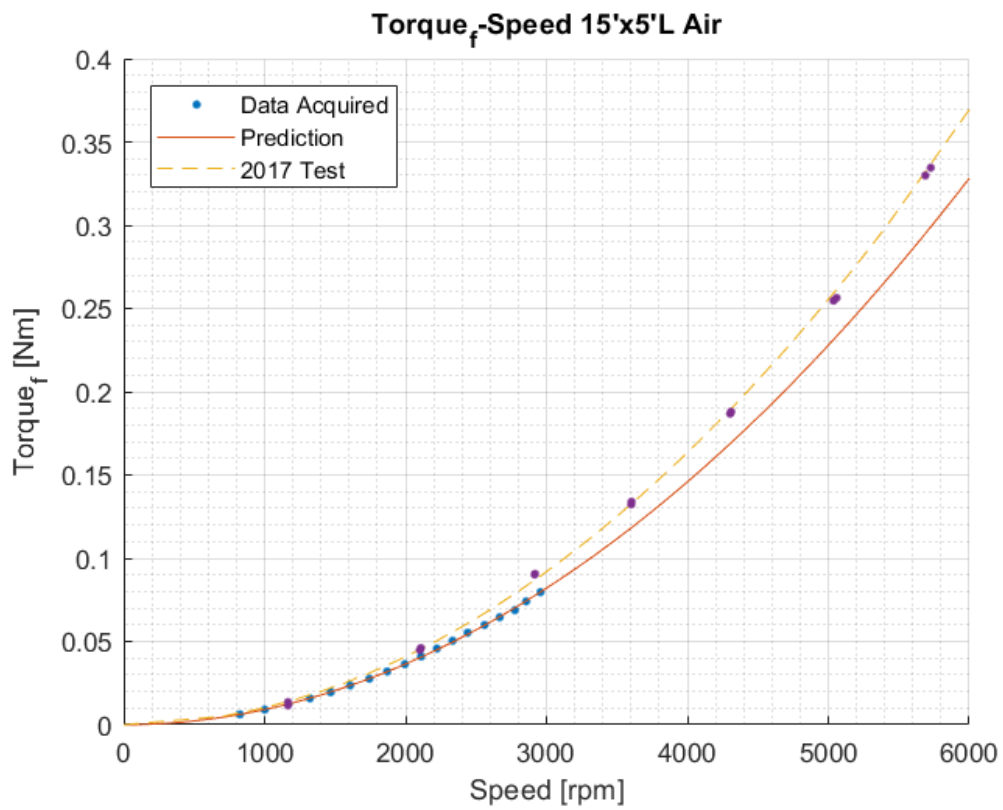


Figure 2.54: Torque speed characteristic for long cable set

vacuum chamber, the cables should be reduced as much as possible to reduce electrical noise effects on the acquired outputs. In particular it should be looked out for anything similar happening, because the vacuum chamber could act as a Faraday cage and increase noise. It was also considered important to continue to acquire the unfiltered torque too because, seen the filtered torque plot in Figure 2.54, it was not evident that something was misbehaving.

## 2.7 New Vacuum Chamber Torque Test Campaign

Once finished the characterization in air of the test architecture for propeller torque testing, it was considered optimal to execute a new testing campaign in vacuum. The air tests defined that all components did not suffer from working previously in low pressure environment and therefore the setup could be rebuilt to use it in Martian-like condition. In particular, in standard air it was confirmed that both the motor as well as the torque meter were working as they should.

Tests in vacuum chamber were performed by placing the test architecture fixed on the internal chamber plate as it was done in the first vacuum fixed setup, described in Figure 2.19. The mechanical changes done for the air campaign were kept and the electronics was similar to the one used for the test performed with long cables. The voltage supply to the motor and the torque meter was provided by two AGILENT E3648A, one of which was piloted by GPIB interface to output the controlled  $U_{mot}$  signal. The voltage passing through the motor supply cables, used to derive the absorbed current, was acquired via GPIB with an HP 34401A multimeter, with  $6\frac{1}{2}$  digits precision. The multimeter was connected to a  $1m\Omega$  shunt in the same configuration shown in Figure 2.35. Due to internal differences in the multimeter electronics, compared to the one used for air tests, this measurement was not acquired when the instrument was excited by an external trigger. The trigger was set, by SCPI commands sent via GPIB, to "Immediate", meaning that the voltage reading would happen as soon as the instrument had enough data, and the voltage data was then acquired by MATLAB only when the data acquisition part of the code was reached. All other inputs and outputs were collected with the previously described MATLAB code, through the USB6211 DAQ, at 1000 Hz frequency for 1 second at each ramp cycle. Signals directed to the USB6211 pin, as described in Table 2.9, were collected in the PCB by a 10 pins connector.

Three tests were scheduled to be performed in TAS-I facility for testing the propeller setup:

1. A standard air test with 15"x5" L propeller;
2. A Martian atmosphere test with 15"x5" L propeller;
3. A Martian atmosphere test with Thales Alenia Space propeller.

These tests were designed to acquire all parameters that could give information about faults happening in the data acquisition process.

### 2.7.1 Standard air test with 15"x5" L propeller

The first test performed in the vacuum chamber was a standard air test with the same propeller used in air characterization. This test was done to check that all electrical connections were working and to check the reproducibility of the performance test in a different environment. The vacuum chamber had to be closed for this test for safety reasons even if it was not evacuated. The test could be performed only up to 1500 rpm: this limitation was due to the current limit imposed on the vacuum chamber connections flanges. The RS232 connector, used to link the instruments inside the chamber to the outside system, could only bear currents up to 2 A per pins, therefore the speed of the propeller could not be increased as it was done in open air test.

This test gave better results than expected: the torque-speed trend was similar to the one acquired in open air and the distribution of the filtered and unfiltered torque was similar, if not better than the one acquired in open air as it is shown in Figure 2.55. The torque aerodynamic coefficient, experimentally found, was  $c_q=0.0034\pm 8.643 \cdot 10^{-5}$  and so in line with the coefficients calculated for air characterization tests. The motor current distribution was also checked by analysing the torque computed with motor constant  $k_T$ . As it can be seen in Figure 2.56, the parallelism between the torque acquired with the torque meter and the computed one is preserved. Torque data were plotted with respect to the speed propeller and superimposed to the ones of open air test to show the correctness of the test, remarkable in Figure 2.57. To complete the analysis waterfall plot for the torque vibrations were made, but the harmonics did not seem to be changed by the closed chamber environment.

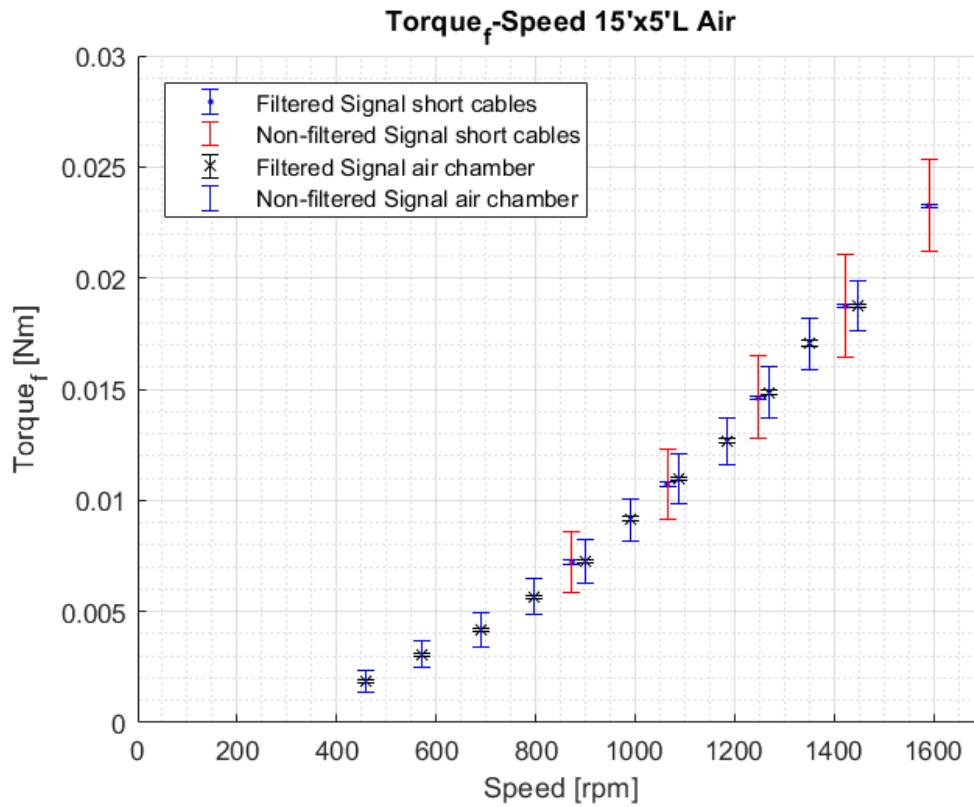


Figure 2.55: Comparison for errorbar data within open air propeller test and vacuum chamber filled with standard air test.

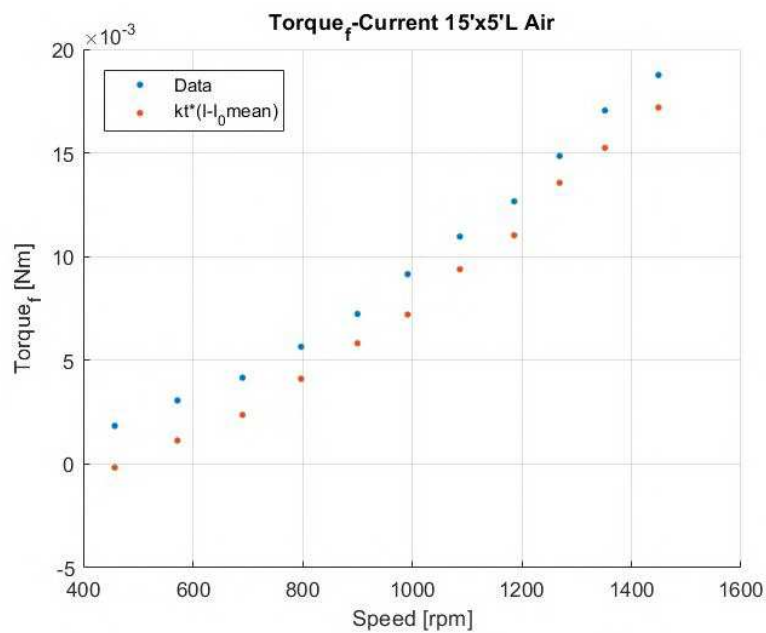


Figure 2.56: Torque comparison between acquired data and computed data for 15"x5"L testing in vacuum chamber filled with standard air

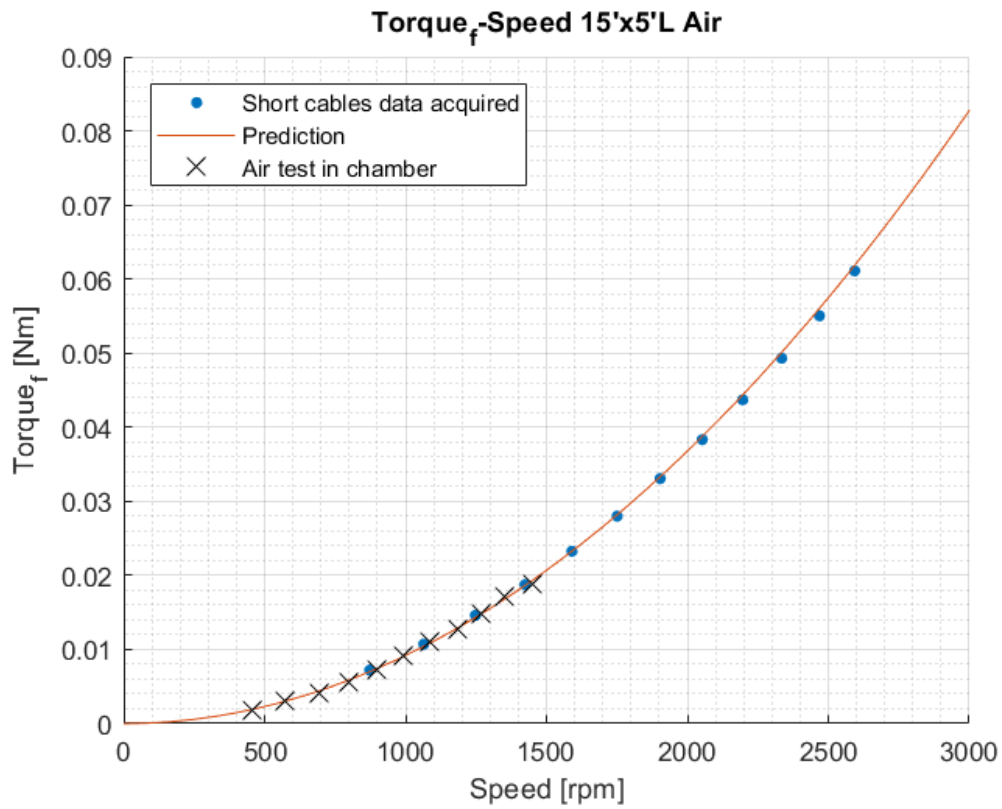


Figure 2.57: Comparison torque-speed data acquired in open air test and in vacuum chamber filled with standard air

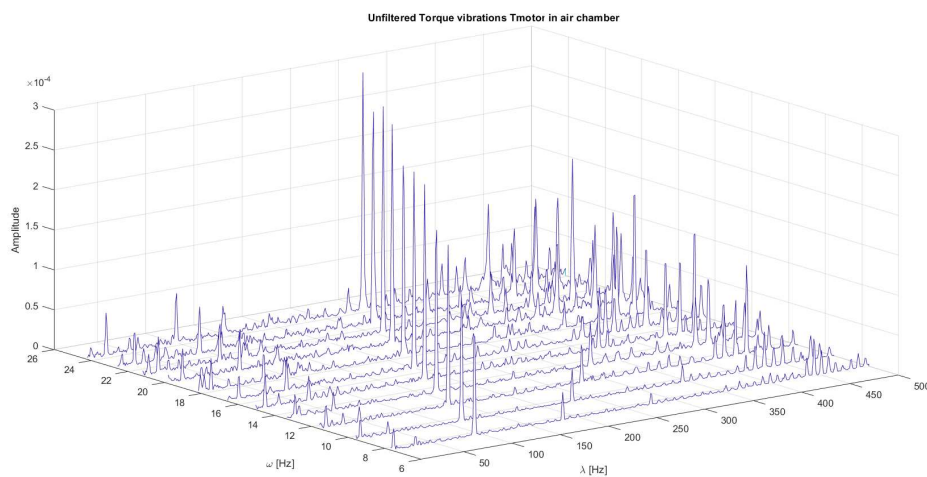


Figure 2.58: Unfiltered torque waterfall for propeller 15"x5" L in standard air in the chamber

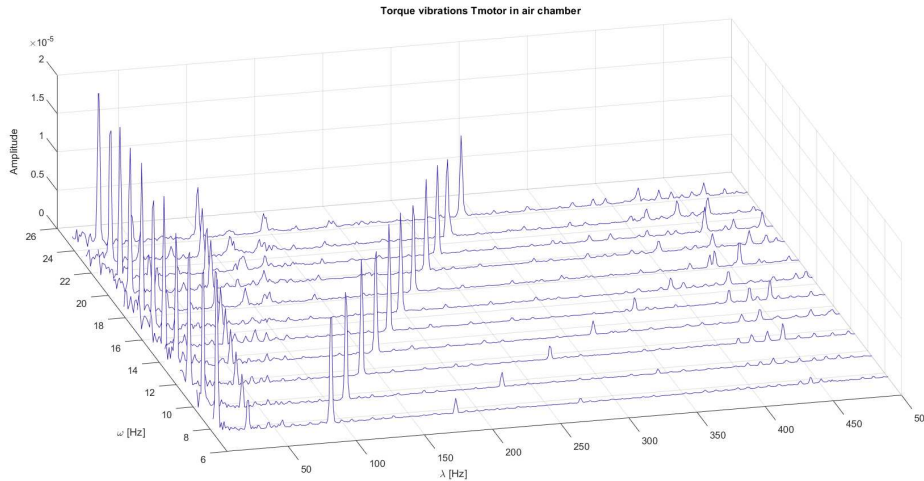


Figure 2.59: Filtered torque waterfall for propeller 15"x5" L in standard air in chamber

## 2.7.2 Martian atmosphere test with 15"x5" L propeller

The second test performed in TAS-I PHASE vacuum chamber was done changing two parameters: the maximum voltage  $U_{mot}$  used to control the propeller speed and the air density. The propeller tested was again the 15"x5" L; this propeller is not made for low density atmospheres and thus the torque generated will be extremely low with comparison to the one seen in air. The correlation that exists between the torque generated by a propeller and the current absorbed by the motor helped to increase the possible spinning velocity for the rotor, since the current in these conditions would not pass the 2 A limit. The test was performed in the vacuum chamber with an inside pressure  $p=13.4$  mbar and an air density  $\rho=1.66 \cdot 10^{-2}$  kg/m<sup>3</sup>.

The results obtained by these testing conditions were curious and hence the test was performed a second time to assure that the results were not due to a temporary problem, but the second test reported the same results as the first one, that are depicted in Figure 2.60.

The torque of the propeller, acquired through the torque meter sensor, was seen increasing up to 0.001 Nm where it would plateau for a couple of seconds, before dropping under zero, when the speed was circa 2700 rpm, and then re-stabilize itself and increase around on the normal-torque trend speed. For this unexpected phenomenon, three hypotheses were formulated:

- The system may have encountered a resonance speed around 2700 rpm;
- The torque read was too low, compared with the torque meter sensitivity to read accurate values;
- The torque meter may not be able to perform accurate measurements in vacuum.

The second hypothesis was immediately discarded because, even if it is true that the torque signal acquired was lower than the torque sensitivity, this would only mean that the measurements acquired would have been inaccurate from the start and not only in

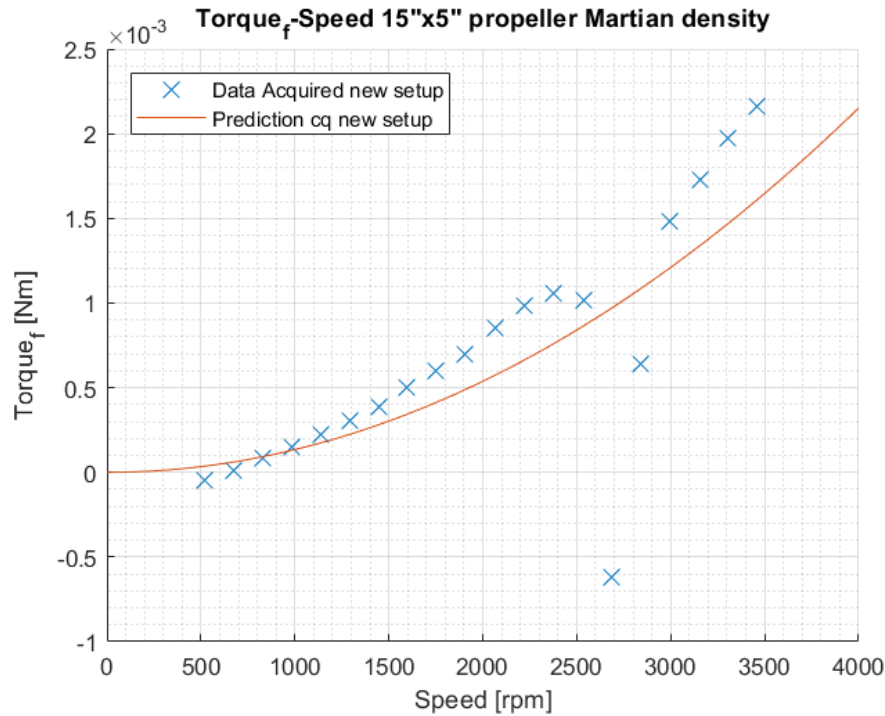


Figure 2.60: Torque-speed data acquired with 15"x5" L propeller in Martian-like atmosphere.

one precise point. It is although possible that the torque trend plotted in Figure 2.60 is not accurate both because it takes into account faulty data in the 2700 rpm area and the torque sensor is not accurate when working around 0 Nm point.

The other two hypotheses were more difficult to check. At first, it was controlled that was the current absorbed by the motor at the torque drop moment and, as it is reported in Figure 2.61, the current did not suffer the same problems that the torque meter identified. This result alone gave important evidence that the motor had been working fine in vacuum environment all along testing campaigns.

The speed reported in all above testing charts is the one acquired with the torque meter encoder, but since in this case some major problems were found, the speed was also computed with respect to the motor characteristics. The motor output velocity was calculated as described in equation 2.5 with the motor data acquired in this test and superimposed in a plot, represented in Figure 2.62, to the speed obtained from the used encoder. It can be seen that the encoder speed is equal to the one calculated with the supply electrical data. It can be concluded that at least the torque meter encoder is working, leaving open the suggestion that the whole sensor is working correctly.

To enforce the idea that the torque problem was only due to the encounter of a critical speed the unfiltered torque and the vibrational response of the acquired signals was checked. The standard deviation distribution of the unfiltered torque is subjected to a large increase in the same spot where the torque value dropped as it can be seen in Figure 2.63.

Waterfall plots for both filtered torque and unfiltered torque gave curious results as it can be seen in Figure 2.64 and Figure 2.65.

It is noticeable in the order analysis, that the harmonics excited are the same excited in air. In particular it can be seen that, around 450 Hz there is a resonance peak, when

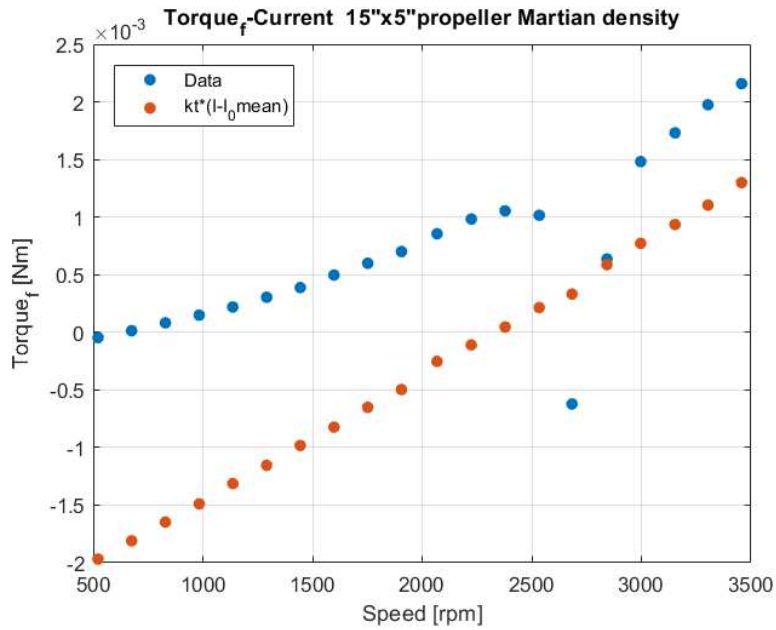


Figure 2.61: Torque comparison between acquired data and computed for 15"x5" L in low density environment

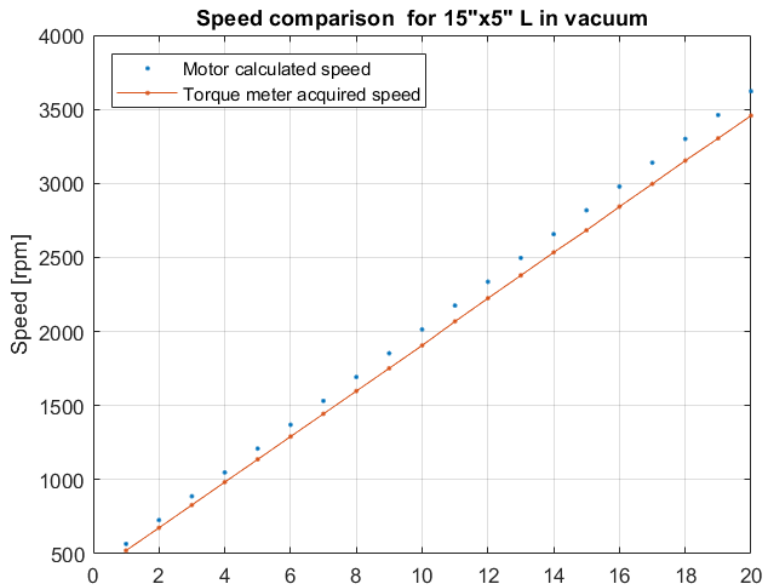


Figure 2.62: Comparison speed as read by the torque meter encoder and as computed from the motor characteristic for 15"x5" L propeller in low density atmosphere

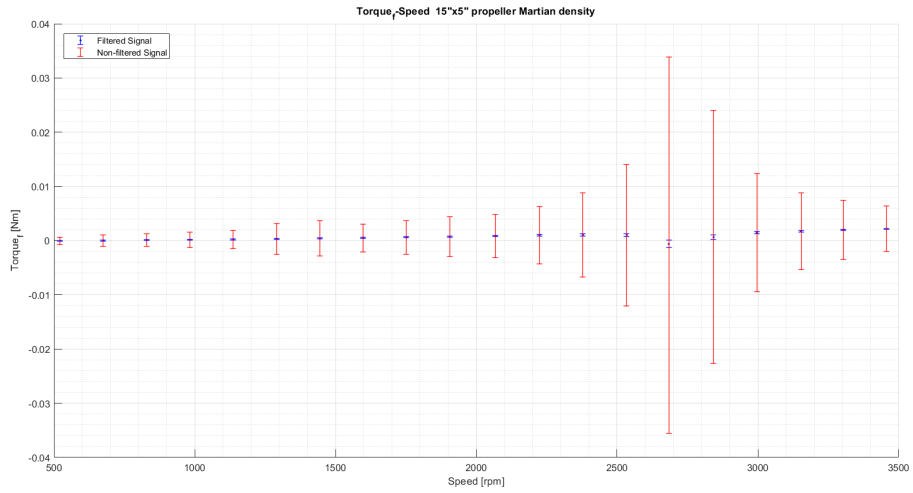


Figure 2.63: Errorbar torque distribution for 15"X5" L propeller in Martian-like atmosphere

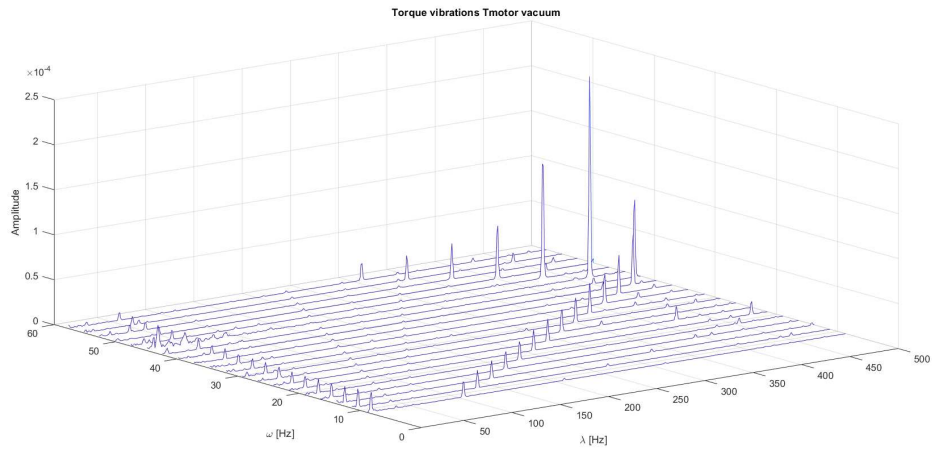


Figure 2.64: Filtered torque waterfall for propeller 15"X5" L in Martian like density

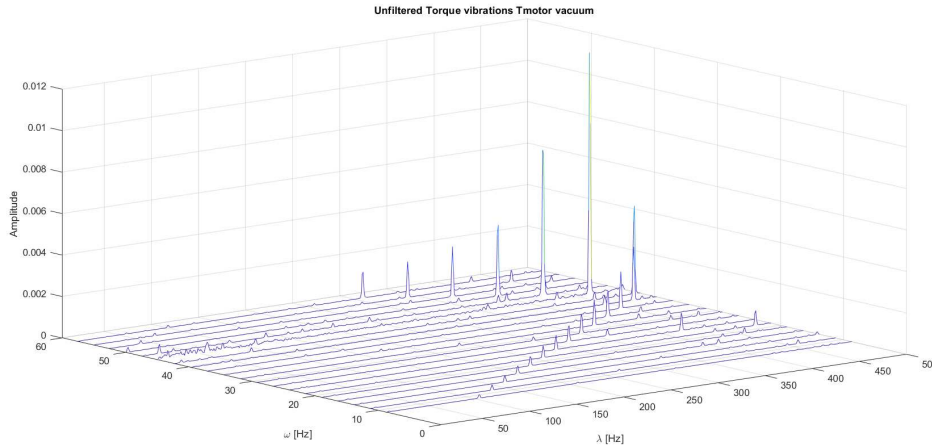


Figure 2.65: Unfiltered torque waterfall for propeller 15"x5" L in Martian-like density

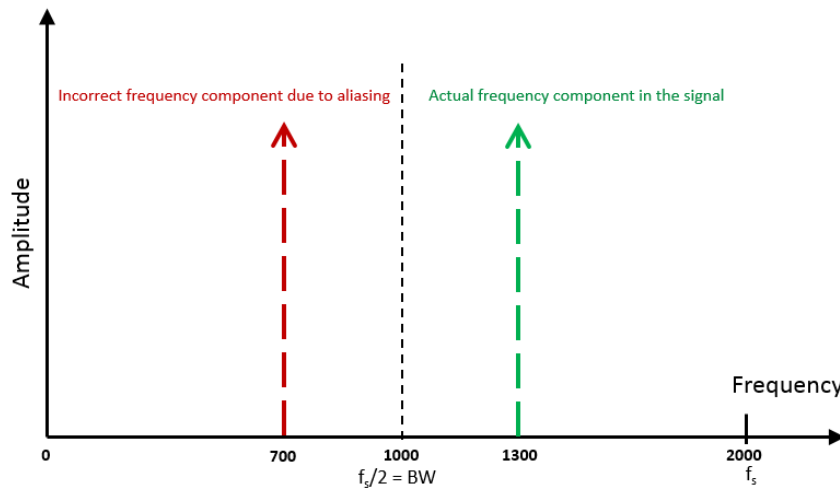


Figure 2.66: Aliasing causes mirroring the frequency that happens to be higher than  $f_{max} = f_s/2$ , where  $f_s$  is the sampling frequency. ©SIEMENS

the critical speed encounters a series of inverse diagonally peaks. These peaks do not have any physical meaning in the position where they are in the waterfall plot. It was found that they correspond to the aliasing of the signal as it is described in Figure 2.66. Aliasing happens when the maximum frequency content  $f_{max}$  of a signal is higher than half the sampling rate used. This process causes the vibrations order to be mirrored with a wrong frequency in the waterfall plot. Therefore the resonance peak here seen 450 Hz, would be most likely placed at 550 Hz, and therefore corresponds to the one found with SCADAS acquisition in open air and the inversely diagonal peak would be the continue of the x12 harmonic after 500 Hz. For future tests, the frequency sampling rate should be increased over 1000 Hz to read the resonance in the most appropriated way without aliasing phenomena.

This aliasing problem was never acknowledge for the fft algorithm before this test, even if the reverse peaks are also shown in Figure 2.64. This happened because since they were quite small no importance was given to them. It is important to highlight that the amplitude of the peaks was increased by changing the density of the air in the vacuum

chamber, meaning that low pressure densities have an influence on the torque measure acquired by the sensor.

### 2.7.3 Martian atmosphere test with Thales Alenia Space propeller

The last test performed with this architecture was a torque test for the Martian blade used last year to check if a Martian drone design was possible. The rotor was mounted as described in section 2.2.7 on the torque meter shaft. The test was performed in the vacuum chamber with an inside pressure  $p=14$  mbar and an air density  $\rho=1.66 \cdot 10^{-2}$  kg/m<sup>3</sup>.

The test results were compared with the one found in vacuum with the previous fixed setup and acquisition system, here illustrated in section 2.3.2. The  $c_q$  computed, with the Equation 2.15, for this propeller, with respect to the torque data acquired, is:

$$c_q = 0.0361 \pm 0.0023$$

That is similar to the value found by first vacuum tests performed with the swing test bench architecture:

$$c_{qSwing} = 0.0384$$

but it is still quite far away for the one computed by the University of Maryland's study that was used for performance reference:

$$c_{qMaryland} = 0.0174$$

A positive point is that, as shown in Figure 2.67, the filtered torque reduced enormously the standard deviation of the data acquired even in vacuum. In particular, it was important to see that even the unfiltered torque was less spread than the one of previous vacuum tests, thanks to the changes in the supply system and the mechanical design. It can be also spotted that data acquired with the new setup follow a more stable trend than the ones acquired with the swinging setup. This phenomenon could be due to the new acquisition code that waits for the transient dynamics to reduce themselves before acquiring data. In Figure 2.67 the last acquired data may seem contradictory, since the unfiltered torque has a high increase in the standard deviation, it is important to say that this phenomenon was linked to the absorbed motor current reaching the 2 A limit. In order to do not cause problem to the vacuum chamber structure, the current limit was also set in the ESC controller and therefore once reached the 2 A maximum value the motor would stop working as it does in standard conditions.

For this test, it was important to check the relationship of the computed torque with the acquired one as it was done for all previous experiments. Even in this case the torque read by the torque meter was parallel to the one computed with the motor constants, only showing a different behaviour when the motor reached the current limit, but as already said these points may be neglected since they represent the motor behaviour in a very specific condition. The relationship between the acquired torque and the one deduced by the current absorbed is shown in Figure 2.72.

Waterfall plots for torque vibrations were plotted for both the filtered measure and the unfiltered one, reported in Figure 2.70 and 2.71. If compared with the same analysis done for the first fixed vacuum setup built, shown in Figure 2.17, it can be seen that

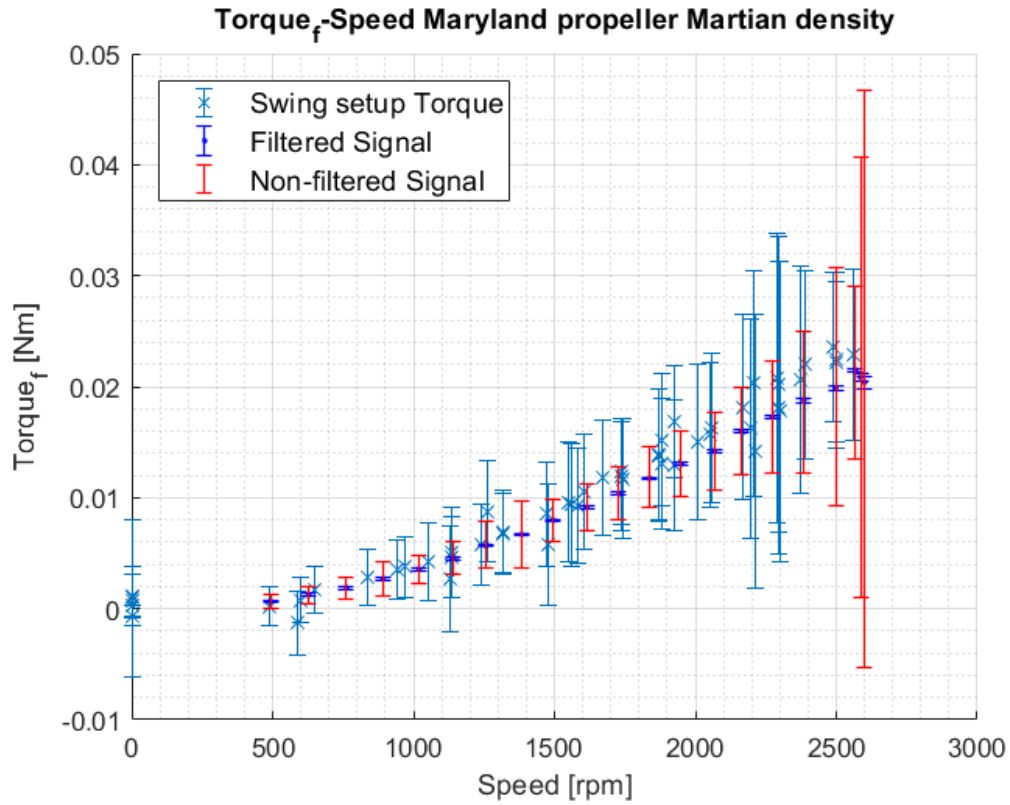


Figure 2.67: Torque distribution for previous Martian propeller tests in TAS-I PHASE chamber and for data acquired with the new system

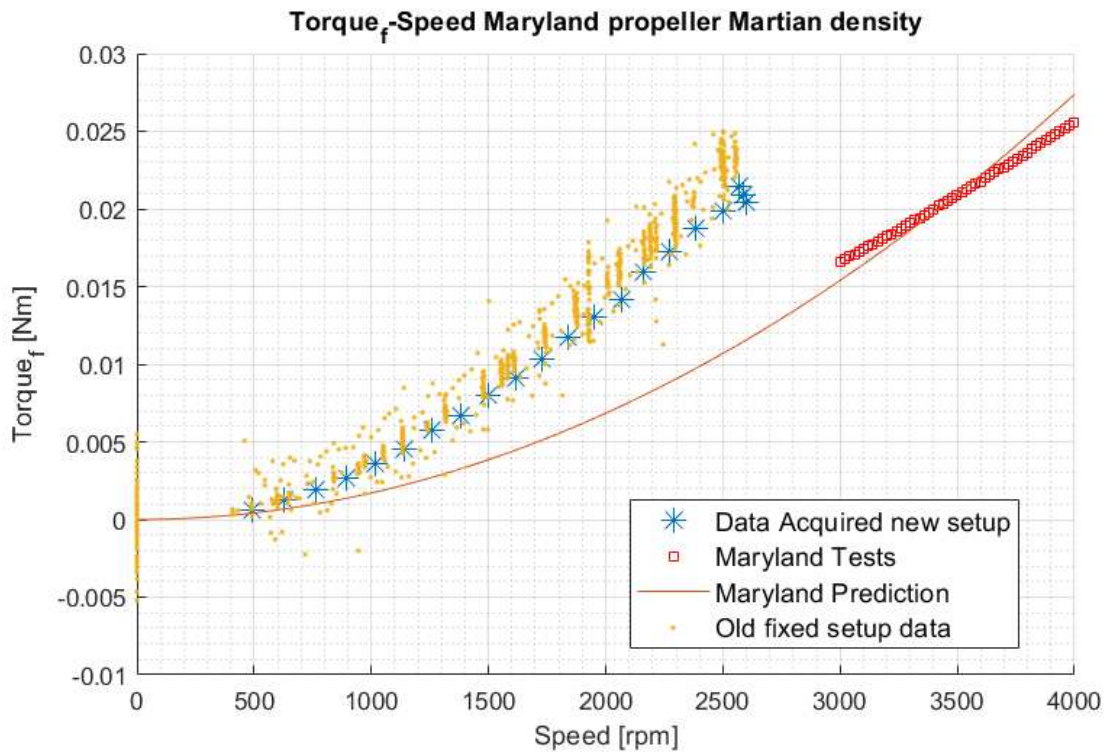


Figure 2.68: New architecture torque result for Martian propeller compared to University of Maryland's one.

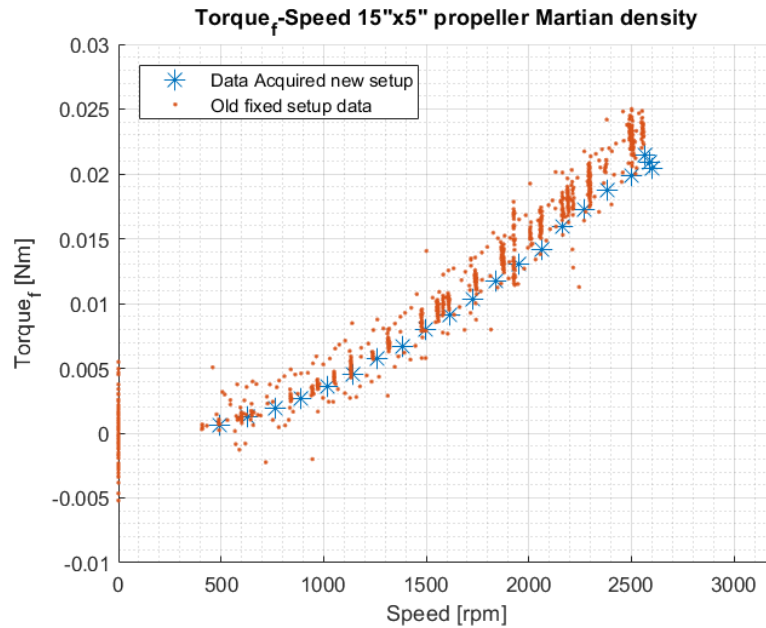


Figure 2.69: Comparison between torque data found for fixed setup in PHASE vacuum chamber before and after the architecture changes

vibrations have overall been reduced by two orders of magnitude when filtered, while for the unfiltered all orders, except for the x12 harmonic, were reduced in amplitude.

This test seems to hint that the torque meter is reading the torque as it should and therefore the distance between the University of Maryland propeller trends and its twin built by Thales Alenia Space does not dwell nor in the torque meter neither in the motor electronics, but most likely in the manufacturing of the rotor itself.

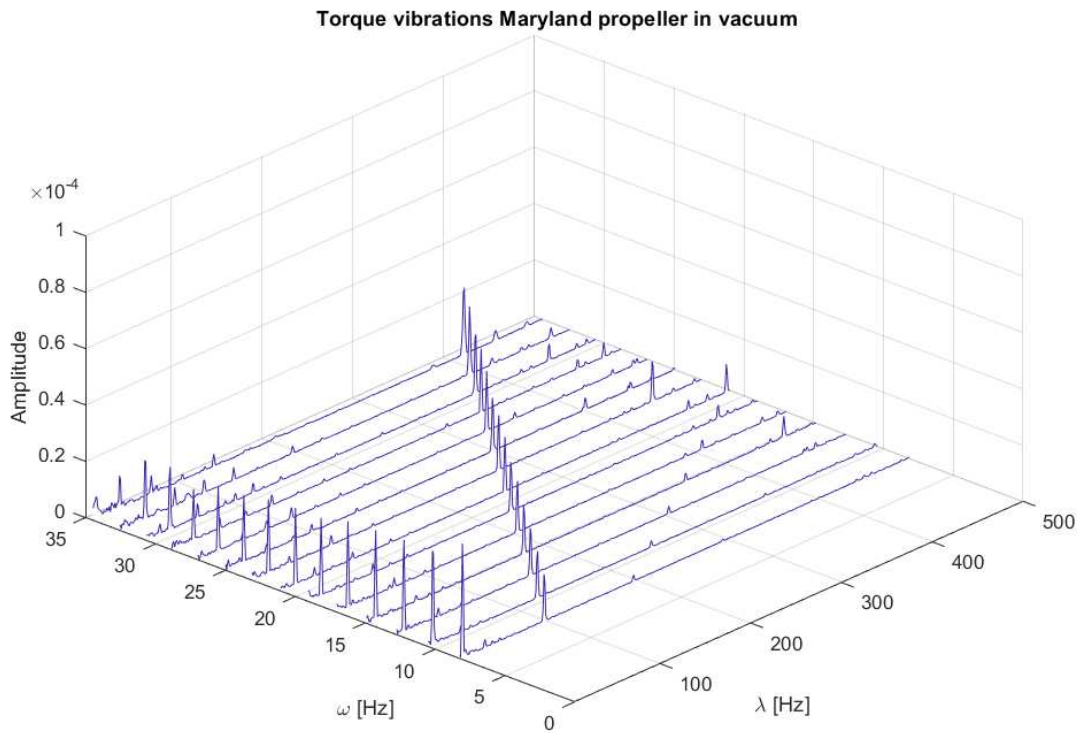


Figure 2.70: Filtered torque waterfall for Martian blade in vacuum

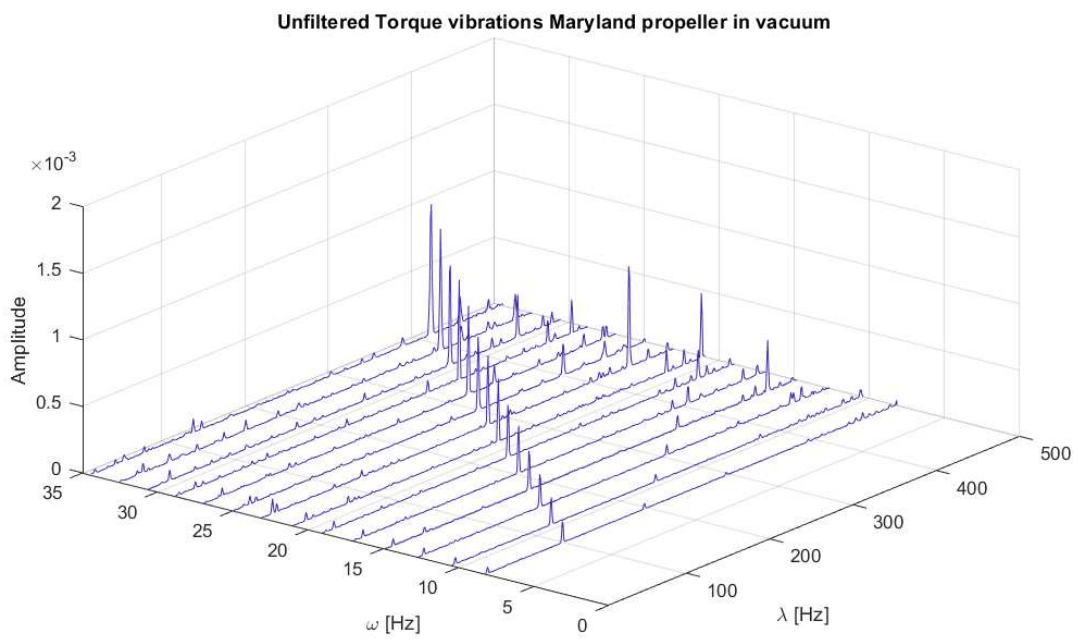


Figure 2.71: Unfiltered torque waterfall for Martian blade in vacuum

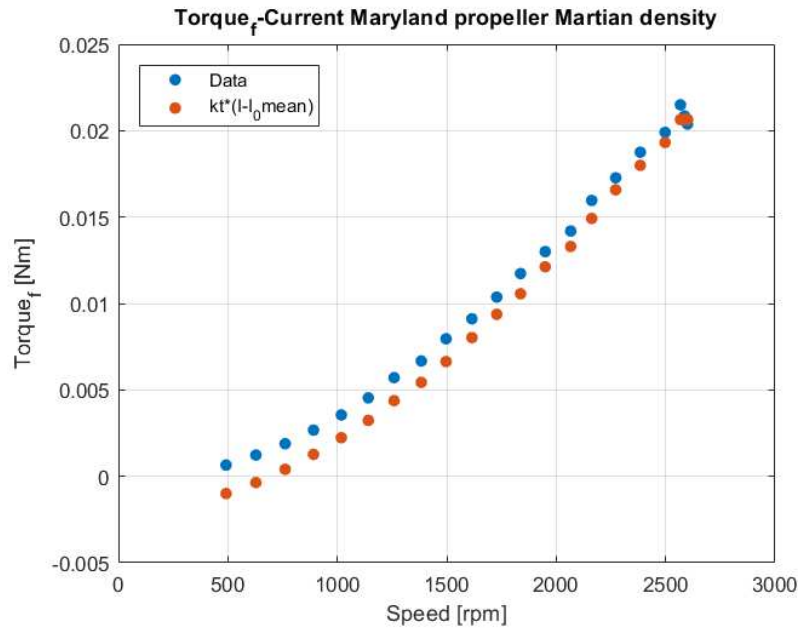


Figure 2.72: Computed and acquired torque comparison for Martian blade in Martian-like conditions

## 2.8 Investigation on new Thrust Test-bench

When the performance for the Martian propeller, obtained with the swinging setup, were analysed, the most important problem to solve was the deviation of the torque measurement from what was the trend expected. The thrust data, on the contrary, were in line with the ones from the study used as a comparison, anyhow thrust, in different test runs, was not as accurate as it was supposed to be, therefore it was thought to study a possible design for a new test bench that help to increase the accuracy of thrust force acquisition. As already discussed when analysing torque data, the synchronous acquisition of torque and thrust is extremely difficult to perform and usually it results in obtaining inaccurate measurements. Hence, it was thought that, for the future experimental campaigns of the Martian drone, it would be better to build two different setups, each one measuring only one physical quantity.

In order to provide a more accurate and precise test stand for the measurement of the thrust, a new, more compact design, that minimizes the unknown degrees of freedom, was hypothesized. The basic design architecture would not include a load cell, but acquired the force indirectly by a torque meter. The scheme of the possible setup is described in Figure 2.73.

In this scheme,  $b$  represents the distance between the axis of symmetry of the propeller and the fulcrum of the torque meter, and  $r$  is the radius of the blade used. The forces and moments generated are represented as:

- $T$  is the torque generated by the propeller when spinning;
- $P$  is the weight of the motor on the end of the arm;
- $M$  is the induced moment on the torque meter arm, by the propeller.

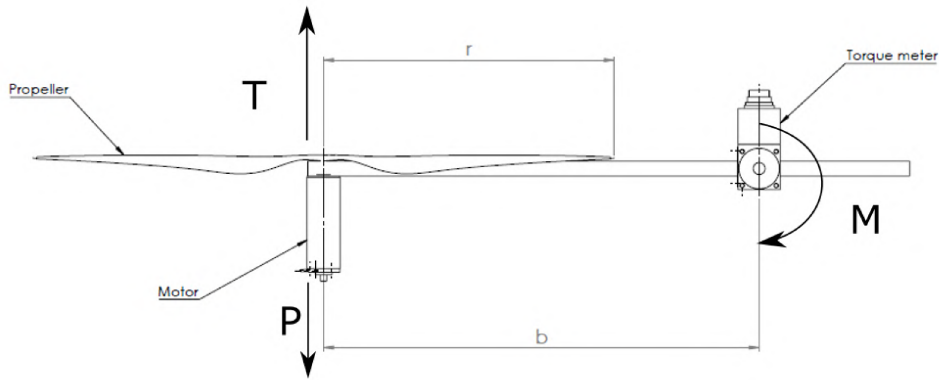


Figure 2.73: New thrust setup design

This new test stand is designed to connect the motor and the propeller on one end of a metal beam and attach the beam, near to the free end, to the measuring shaft of the torque meter. The drive side of the torque meter would be kept fixed through a clamping system. This particular architecture is useful since the torque read through the sensor is directly proportional to the thrust generated by the propeller. It is important to underline that in this study the weight of the motor, the propeller, and the beam will not be taken into account for measuring the torsional moment on the torque meter axis since they could be balanced with a pre-charge on the free end of the beam.

The moment read by the torque meter sensor, when the propeller is spinning, will be:

$$M = T \cdot b \quad (2.22)$$

where:

- $M$  [Nm] is the moment read;
- $T$  [N] is the thrust force of the propeller;
- $b$  [m] is moment arm with respect to the torque meter axis.

Moreover it has to be remembered that thrust forces of a propeller is defined by the the propeller  $c_t$  coefficient as:

$$T = c_T \rho \omega^2 D^4 \quad (2.23)$$

where:

- $c_T$  is the thrust coefficient of the propeller;
- $\rho$  [kg/m<sup>3</sup>] is the density of the air;
- $\omega$  [rpm] is the rotational speed;
- $D$  [m] is the diameter of the blade.

The moment arm and the speed of the propeller are the two main parameters for this test bench. In order to define the torque meter needed for this kind of test, it was performed a first mathematical study where it was supposed that the first experiment would be conducted in normal air in the 15"x5" L propeller used for torque characterization. For the first part of the study, it was supposed that the torque meter used would be the HBM

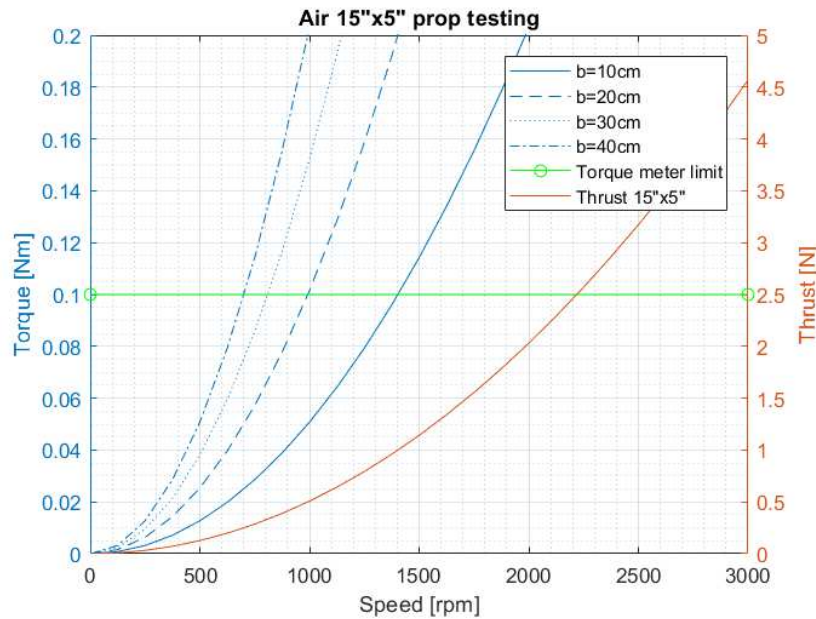


Figure 2.74: Moment arm for air test analysis

T21WN, adopted until now as torque sensor, this hypothesis was formulated supposing that the torque meter would work in vacuum environments. Choosing this torque meter as sensor, it was investigated if a torque sensor with nominal torque 0.1 Nm would be suitable for this setup.

In this case, the maximum arm length possible was 40 cm and its minimum matched the propeller radius length since the rotor would be laying in the same plane as the torque meter. Varying the moment arm between these two values and increasing the rotational speed to a maximum of 3000 rpm the graph shown in Figure 2.74 was obtained.

It can be seen that for lower arms, the propeller speed possible would increase, but alas, in standard air, this configuration would only allow reaching 1500 rpm circa.

Since this test bench is being designed for testing the Martian propeller thrust in low vacuum atmosphere, the same calculations done for air, were reported for Martian atmosphere. In particular, it was computed the torque corresponding to the maximum thrust achieved at 4000 rpm by the University of Maryland's propeller as a function of the varying beam arm. The value of the thrust at this specific speed was calculated with the Equation 2.23, using the  $c_t$  experimentally found and the Martian density defined in literature, reported in Table 1.1.

As it can be seen from Figure 2.75, the maximum moment arm length, feasible for measuring thrust up to 4000 rpm in vacuum, supposing a nominal torque for the sensor equal to 0.1 Nm, is 22 cm. Torque data with different lengths for the beam arm were plotted as function of spinning rotor speed in Figure 2.74. It can be seen from the above mentioned chart that even a 30 cm arm would give the possibility to acquire performance data up to 3500 rpm, which is the limit used for experimental testing in TAS-I PHASE chamber. This plot highlights that this test bench, with a torque meter of 0.1 Nm rated torque, would be suitable for reading the thrust force generated by the Martian propeller in vacuum.

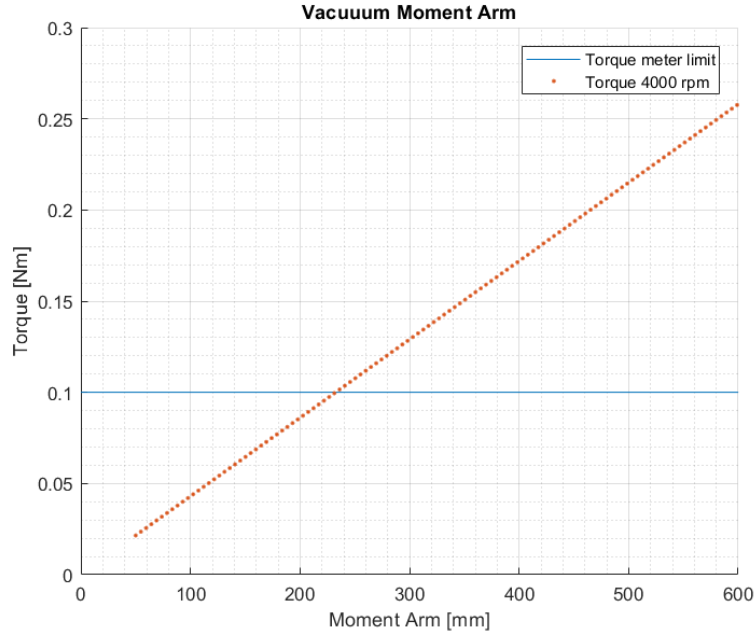


Figure 2.75: Maximum thrust defined as a moment in function of the beam arm length

Even though the system is feasible two main possible issues have to be checked before proceeding in the implementation of the test bench:

- If the reduced dimension of TAS-I PHASE vacuum chamber allows this kind of setup;
- If the stress limits on the measuring shaft are not overcome.

The first problem is articulated in two parts: the actual dimensions of the chamber and the aerodynamic effect of the propeller within the chamber. TAS-I PHASE, as described in Figure 2.1, has an internal serviceable diameter of 70 cm and therefore would easily accommodate the structure presented in Figure 2.73. The length of the beam would be between 30 and 20 cm. Although, it has to be said, that the direction of the propeller inside the chamber is not negligible: in fact, aerodynamic resonances and recirculation effects may interfere with the thrust of the propeller. Until this moment the setup was envisioned to have the propeller perpendicular to the longitudinal axis of the TAS-I PHASE chamber, but it had to be changed to reduce unexpected aerodynamics effects. Setting the direction of the propeller parallel to the chamber axis was challenging, because forces would not be distributed as before, as it can be seen in Figure 2.77. In particular, it can be seen that the weight of motor and rotor combination, that before was reducing the thrust force, in this case, is acting on a different plane. The weight directed in the  $z$  direction causes a flexural moment on the torque meter shaft. If the torque meter used is supposed to be the same used for torque measurements, then the limits for forces acting on the shaft, described in section 2.2.6 should be taken into consideration. In the case of the new setup shown in Figure 2.77 the forces acting on the shaft will be the following:

- Axial Force:  $F_a = P = 1.96N < 2 \text{ kN}$ ;
- Radial Force:  $F_r = T \leq 0.4N < 3.6 \text{ N}$ ;

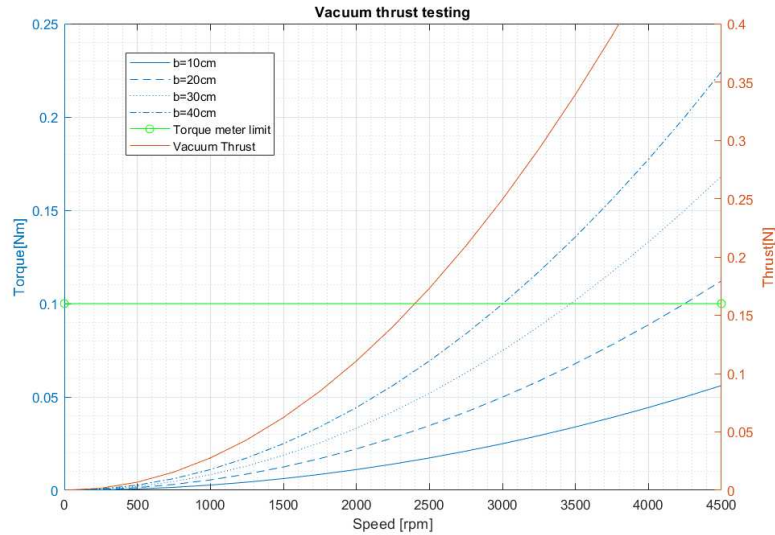


Figure 2.76: Thrust moment as a function of the arm length with respect to the speed in vacuum condition

- Bending Moment:  $M_f = P \cdot b = 0.45 Nm \geq 0.12 Nm$ .

It can be noted that the bending moment acting on the torque meter shaft overcomes the limit imposed. This issue may be resolved by either inserting a counterweight able to produce an inverse moment and so reducing the total bending moment, but the axial force limit should be then checked, or by searching a torque meter whose limits on shaft reaction forces are higher.

As previously stated, all the study of this new test bench hypothesized that the torque sensor used was the same used for torque measurements and that it would work correctly in vacuum. It is anyway advisable, if this setup would be built in future, to chose a different torque meter, because either-wise all performance data will depend on the same sensor and therefore if this is defective then all data acquired will be inaccurate.

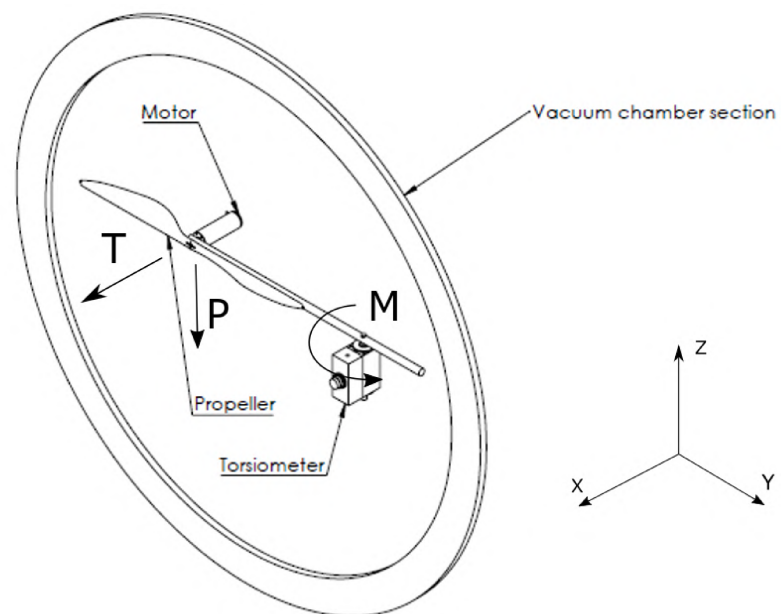


Figure 2.77: Thrust test bench with propeller parallel to the vacuum chamber axis.

# Conclusion

The initial aim of this thesis was to design a new test bench for the acquisition of both torque and thrust. To acquire accurate measurements it was though optimal to decouple the test bench in two different setup configurations: one fixed, like the one used for open air testing, for the torque and a setup with a rotational degree of freedom for the acquisition of the thrust, as defined in the last section. The torque test bench was redesigned by fixing the previously swinging setup, and modifying the connection between the motor and torque meter shafts.

The characterization of the brushless motor highlighted that the parameters  $k_T$ ,  $k_I$  and  $k_V$ , reported by the motor datasheet, were accurate. Therefore, they could be used to compute, thanks to the monophasic equivalent model, the torque and the speed of the motor, by acquiring the electrical supply voltage and the current absorbed by the motor. It is important to remember that this statement is only correct when the motor control signal is saturated over its maximum limit value and the internal speed control loop of the driver is disabled. If the motor is controlled otherwise, the datasheet parameters do not match experimental ones. It was also defined that the new way of acquiring data, with a ramp, followed by a stable speed acquisition is more suitable for obtaining accurate outputs and therefore, it should be envisioned to use the same layout for future tests, irrespective of if the torque or the thrust is acquired.

The torque meter characterization, on the other hand, presented mixed results: it was discovered that the sensor had not being damaged by the previous vacuum tests since it worked perfectly in standard air, but in vacuum the data acquired encountered vibrational issues. It has to be noticed that the torque meter in air needed filtering of the torque signal in order to remove the noise generated by the commutation ripple torque of the motor. It is important to define that the fixed setup, designed for improving the torque accuracy, has corrected the distribution of the torque filtered and unfiltered, by reducing their vibrations with respect to torque data acquired with the former fixed and swing setups. This means that the stiffening of the connection between the motor and the torque meter shafts, as well as the modifications applied to the acquisition and electrical systems were necessary to improve the data acquisition accuracy of the testing architecture. Moreover, it was confirmed that the long electrical connections, used to link the setup inside the vacuum chamber and the instruments outside of it, have little or no influence on the acquired data. In vacuum, the vibrations of the torque meter signal were increased, implying that the torque sensor measurements could be influenced by the different pressure in the chamber atmosphere. It is although to underline that, in vacuum, the torque meter encoder was proved to work correctly, by comparing the acquired rotor velocity with the one computed by the motor model. Furthermore, the torque acquired in vacuum, when no resonance was encountered, followed the one computed with the motor

equations, leaving open the possibility that the mean torque acquired by the sensor is correct even at low pressures.

The trend of the torque found, with the new setup, for the Martian propeller, even if more accurate and less dispersed than in previous tests, was not able to match the curve found by the study of the University of Maryland. This result led to the conclusion that the difference in the parameter  $c_q$  found between the American study and the one of Thales Alenia Space, may be induced by the wrong design of the propeller itself. This is also possible since the propeller was reconstructed by the dimensions described in the scientific paper published, but no evidence that the data published by Maryland's University had been collected with that blade was reported in the paper itself.

For future analysis, it would be valuable to test the torque meter with another propeller for low pressure atmosphere whose torque characteristics have been defined by software simulation. In this way, it would be totally certain if the torque meter is only inaccurate in the torque distribution or if the mean value acquired is wrong. Since performance measurements for a propeller need a high accuracy it would be advised to rebuild the torque setup using a vacuum rated torque meter or discard the torque sensor and identify the torque only by the absorbed current of the motor. Parallel to the new torque setup, it would be advisable to rebuild the thrust setup, as describe in this thesis, in order to decouple the measurement and acquire new, more accurate thrust data for the propeller.

# Nomenclature

ABBREVIATIONS	FULL NAME
ABS	Acrylonitrile Butadiene Styrene
BLDC	Brushless Direct Current
BNC	Bayonet Neill-Concelman connector
CAD	Computer Aided Design
CNES	Centre National d'Etude Spatial
DAQ	Data Acquisition
DC	Direct Current
ESA	European Space Agency
ESC	Electronic Speed Controller
EHV	Extreme Ultra-high Vacuum
EMF	Electro-Magnetic Force
FFT	Fast Fourier Transform
FRF	Frequency Response Function
FVC	Frequency to Voltage Converter
Fund.	Fundamental
GND	System Ground
GPIO	General Purpose Interface Bus
I/O	Input/Output
ISAS	Institute of Space and Astronautical Science
JPL	Jet Propulsion Laboratory
MOSFET	Metal-Oxide-Semiconductor Field-Effect Transistor
MRTS	Martian Rotor Test Stand
MSH	Mars Helicopter Scout
N	Magnetic North
NASA	National Aeronautics and Space Administration
NI	National Instruments
PCB	Printed Circuit Board
PI	Proportional-Integrative
PFI	Programmable Function Input
PWM	Pulse-Width Modulation
rev	revolution
RC	Radio Controlled
RO	Rated Output
RPM	Revolutions per Minute
S	Magnetic South
SCADAS	Supervisory Control And Data Acquisition System

SCPI	Standard Commands for Programmable Instruments
SLAM	Simultaneous Localization and Mapping
STD	Standard Deviation
TAS-I	Thales Alenia Space Italia
TTL	Transistor-Transistor Logic
UAV	Unmanned Aerial Vehicle
UHV	Ultra-high Vacuum
VFC	Voltage to Frequency Converter

---

# Acknowledgement

Since my final high school project on Hubble telescope, it has been my dream to be able to work in the Spatial industry. Therefore, I would like to thank Prof. Chiaberge and Thales Alenia Space, in particular my supervisor Carlo Maria Paccagnini, who gave me the opportunity to get closer to this reality. A big thank you goes also to Mario Silvagni who supported me in the development of the thesis as well as in the experimental campaigns in standard air, along with Pippo Castorina who followed and helped the vacuum chamber experiments. I am particularly grateful for all the support given by the LIM team: Gianluca, Federico, Dario and Luis. A special thank you goes to Andrea, Fabio and Davide who have been part of this Martian project. My special appreciation goes to my family who has been able to support me, no matter what during this project and in all my academic career, and who thought to appreciate what it is given to you and to fight and endure in your projects until the end. Last, but certainly not least a huge thank you to my Lucas, the next big aerospace engineer, who supported me with his great knowledge in astrophysics and with his kind words everyday for the past year.

# Bibliography

- [1] B. Balaram, T. Canham, C. Duncan, H. F. Grip, W. Johnson, J. Maki, A. Quon, R. Stern, and D. Zhu, “Mars helicopter technology demonstrator,” in *2018 AIAA Atmospheric Flight Mechanics Conference*, American Institute of Aeronautics and Astronautics, Jan 2018.
- [2] R. Schicker and G. Wegener, “Measuring torque correctly,” p. 261.
- [3] A. Datta, B. Roget, D. Griffiths, G. Pugliese, J. Sitaraman, J. Bao, L. Liu, and O. Gamard, “Design of a martian autonomous rotary-wing vehicle,” *Journal of Aircraft*, vol. 40, p. 461–472, May 2003.
- [4] A. MiMi, “Mars helicopter scout,” Apr 2015.
- [5] U.S. Government Printing Office, “U.S. Standard Atmosphere,” 1976.
- [6] I. Kroo and P. M. Kunz, “Development of the mesicopter: A miniature autonomous rotorcraft,” 1999.
- [7] D. Greer, P. Hamory, C. Edwards, K. Krake, and M. Drela, “Design and predictions for high-altitude (low reynolds number) aerodynamic flight experiment,” *Journal of Aircraft*, vol. 37, no. 4, p. 684–689, 2000.
- [8] R. Shrestha, M. Benedict, V. Hrishikeshavan, and I. Chopra, “Hover performance of a small-scale helicopter rotor for flying on mars,” *Journal of Aircraft*, vol. 53, p. 1160–1167, Jul 2016.
- [9] L. A. Young, E. W. Aiken, M. R. Derby, L. Gatos, R. Demblewski, and J. Navarrete, “Experimental investigation and demonstration of rotary-wing technologies for flight in the atmosphere of mars,”
- [10] G. A. Ament and W. J. F. Koning, “Isolated rotor forward flight testing from one atmosphere down to martian atmospheric densities,” 2018.
- [11] M. McCoy, A. J. Wadcock, L. A. Young, and M. Field, “Documentation of the recirculation in a closed-chamber rotor hover test,” 2016.
- [12] *The Cambridge Aerospace Dictionary (2nd edition)*. 2010.
- [13] F. H. Grip, L. Young, B. Allan, B. Mettler, and M. S. Martin, “Flight dynamics of a mars helicopter,” 2017.
- [14] J. Garcia, T. Mathy, and H. Diez, “Mosquito, mars original system for qualitative imaging and tactical operations. system and architecture analysis.,” *66th International Astronautical Congress*, p. 10.

- 
- [15] H. Bezard and J.-M. Moschetta, “Aerodynamic study of a micro-uav for mars exploration,” p. 8.
- [16] P. Lv, J. M. Fu, Z. F. Xia, F. Mohd-Zawawi, E. Benard, and J. M. Moschetta, “Numerical investigation of a proof-of-concept rotor in martian atmosphere,” p. 7.
- [17] N. Tsuzuki, S. Sato, and T. Abe, “Conceptual design and feasibility for a miniature mars exploration rotorcraft,” 2004.
- [18] M. Chiaberge, M. Silvagni, and F. Tessari, “Uav powertrain efficient design through a model-based approach,” *International Journal of Mechanics and Control*, vol. 19, p. 18, Jun 2018.
- [19] R. K. Mobley, *An introduction to predictive maintenance*. Butterworth-Heinemann, 2. ed ed., 2002.
- [20] Y. Ji, B. Li, and J. Sun, “Harmonic analysis on torque ripple of brushless dc motor based on advanced commutation control,” *Journal of Control Science and Engineering*, vol. 2018, p. 1–9, 2018.
- [21] E. W. Aiken, R. A. Ormiston, and L. A. Young, “Future directions in rotorcraft technology at ames research center,” 2000.
- [22] F. Tessari, “Power optimization methods and technologies for unmanned robotic systems,” *Politecnico di Torino, Master of Science Thesis*, Oct 2016.
- [23] A. Botta, “Mars drone rotors and engines testing in mars-like atmosphere,” *Politecnico di Torino, Master of Science Thesis*, Dec 2017.